**Title**
Molecular mechanisms of C-type inactivation and lipid regulation in K2P channels



**Author**
Natale, Andrew Martin

**Publication Date**
2022

Peer reviewed|Thesis/dissertation

# Molecular mechanisms of C-type inactivation and lipid regulation in K2P channels

by
Andrew M. Natale

DISSERTATION
Submitted in partial satisfaction of the requirements for degree of
DOCTOR OF PHILOSOPHY

in

Biophysics

in the

GRADUATE DIVISION
of the
UNIVERSITY OF CALIFORNIA, SAN FRANCISCO

Approved:

DocuSigned by:
Michael Grabe
5B8B990D587B414...

Michael Grabe
Chair

DocuSigned by:
Daniel Minor

Daniel Minor

DocuSigned by:
Lily Jan
394456D87457494...

Lily Jan

Committee Members

# DEDICATION & ACKNOWLEDGEMENTS

This work is dedicated to my parents. They sparked my curiosity and love of science, and their unwavering support made this journey possible.

I also wish to acknowledge the many people who supported me and with whom I worked throughout my time at UCSF. First, my advisors and committee members Dr. Michael Grabe, Dr. Daniel Minor, and Dr. Lily Jan, who all taught me how to think like a scientist and then gave me the freedom to explore my ideas. I also had the great fortune to collaborate directly with many other dedicated scientists who taught me so much: Fayal Abderemane-Ali, Ambre Bertholet, Paola Bisignano, Sara Capponi, Parker Deal, Yessica Gomez, Yuriy Kirichok, Haerim Lee, Jamie Lincoff, Marco Lolicato, Lianne Pope, and John Rosenberg. And of course, I must acknowledge the friends I made along the way and thank them for their support, both scientific and personal: Christina, Gabe, Greyson, Jason, Keely, Matvei, Sophia, and Yessica (again). And finally, I wish to acknowledge my undergraduate advisor Dr. Joseph Falke, who supported me in my first real scientific endeavors and whose encouragement put me on the path to graduate school.

# CONTRIBUTIONS

Chapter 1 has been adapted from a previously published journal article:

> Marco Lolicato*, Andrew M Natale*, Fayal Abderemane-Ali, David Crottès, Sara Capponi, Ramona Duman, Armin Wagner, John M Rosenberg, Michael Grabe[§], Daniel L Minor Jr[§]. $K_{2P}$ channel C-type gating involves asymmetric selectivity filter order-disorder transitions. *Science Advances* 6:eabc9174 (2020).
>
> *Equal contribution [§]Corresponding authors

The original paper was modified for this dissertation to remove sections and datasets without significant contributions from Andrew M. Natale. Authors Michael Grabe and Daniel L. Minor Jr. supervised the research.

Molecular mechanisms of C-type inactivation and lipid regulation in $K_{2P}$ channels

Andrew M. Natale

## ABSTRACT

$K_{2P}$ potassium channels regulate cellular excitability using their selectivity filter (C-type) gate. C-type gating mechanisms, best characterized in homotetrameric potassium channels, remain controversial and are attributed to selectivity filter pinching, dilation, or subtle structural changes. The extent to which such mechanisms control C-type gating of innately heterodimeric $K_{2P}$s had been unknown. Here, using molecular dynamics and electrophysiology of TREK-1 ($K_{2P}$2.1) I uncover unprecedented, asymmetric, potassium-dependent conformational changes that underlie $K_{2P}$ C-type gating. These asymmetric order-disorder transitions, enabled by the $K_{2P}$ heterodimeric architecture, encompass pinching and dilation, disrupt the S1 and S2 ion binding sites, require the uniquely long $K_{2P}$ SF2-M4 loop and conserved "M3 glutamate network," and are suppressed by the $K_{2P}$ C-type gate activator ML335. These findings demonstrate that two distinct C-type gating mechanisms can operate in one channel and underscore the SF2-M4 loop as a target for $K_{2P}$ channel modulator development.

In addition, it has long been established that TREK family $K_{2P}$ channels are regulated by plasma membrane phospholipids like $PIP_2$. However, the exact lipid binding sites are unknown and even the directionality of regulation by $PIP_2$ remains controversial, and thus the molecular details have been left unclear. Here, using coarse-grained molecular dynamics simulations, I identify 3 distinct lipid binding sites on the surface of TREK-1 and establish their relative binding affinities for $PIP_2$. Two of these sites directly contact the well-known regulatory 'proximal C-terminus' domain of TREK-1. Subsequently, using all-atom computational electrophysiology

simulations, I establish that $PIP_2$ binding to these two sites, as well as basic residue neutralizing mutations, all increase the TREK-1 conduction rate via an electrostatic ion recruitment mechanism. These conditions also alter the distribution of $K^+$ ion in the selectivity filter in ways that likely stabilize the C-type gate active state and lead to higher channel open probability. Finally, my results suggest that $PIP_2$ binding at one of these sites may induce conformational changes that allosterically inactivate the C-type gate, opening the door to resolving previous controversies about the direction of TREK channel regulation by $PIP_2$.

# Table of contents

# List of figures

# List of tables

## List of abbreviations

| | |
|---|---|
| Å | angstrom |
| atm | atmosphere |
| amu | atomic mass unit |
| C | Celsius |
| $C_\alpha$ | alpha carbon |
| CG | coarse-grained |
| CV | collective variable |
| fs | femtosecond |
| K | kelvin |
| $K_{2P}$ | Two-pore-domain potassium (channel) |
| kcal | kilocalorie |
| kJ | kilojoule |
| LINCS | LINear Constraint Solver |
| M4-5A | transmembrane helix 4, 5-alanine mutation |
| MD | molecular dynamics |
| mM | millimolar |
| MSM | Markov state model |
| mV | millivolt |
| ns | nanosecond |
| pA | picoampere |
| PA | phosphatidic acid |

| | |
|---|---|
| PC | phosphatidylcholine |
| PC1 | principal component 1 |
| PC2 | principal component 2 |
| PCA | principal component analysis |
| PCCA+ | Robust Perron Cluster Cluster Analysis |
| pCt | proximal C-terminus |
| PD | pore domain |
| PDBID | protein data bank identifier |
| PE | phosphatidylethanolamine |
| PI | phosphatidylinositol |
| $PIP_2$ | phosphoinositol-4,5-bisphosphate |
| PMF | potential of mean force |
| $P_o$ | open probability |
| PO | palmitoyl-, oleoyl- |
| pS | picosiemen |
| PS | phosphatidylserine |
| RMSD | root-mean-squared deviation |
| RMSF | root-mean-squared fluctuation |
| SF | selectivity filter |
| SM | sphingomyelin |
| tICA | time-lagged independent component analysis |
| TM | transmembrane |

| | |
|---|---|
| TEVC | two-electrode voltage clamp |
| μA | microampere |
| μM | micromolar |
| μs | microsecond |
| VGIC | voltage-gated ion channel |
| WHAM | Weighted Histogram Analysis Method |
| WT | wild-type |

# BACKGROUND

## *Ion channels and potassium leak currents*

The finely tuned bioelectric circuits that run our muscles, brains, and sensory systems are the product of the ion channel proteins residing in our cell membranes. Ion channels comprise a vast and diverse group of proteins found in all classes of organisms but with a common core function: allowing the highly specific permeation of biologically relevant ionic species such as $K^+$, $Na^+$, $Ca^{++}$, and $Cl^-$ across lipid membranes, typically in a tightly regulated fashion in response to voltage and/or environmental and metabolic stimuli. The most famous of these may be the voltage gated $Na^+$ and $K^+$ channels, which though they spend most of their time sealed tightly closed, open in response to a change in membrane potential to orchestrate the brief voltage spike signal known as the action potential – an event key to the function of nerves and muscles (Hodgkin & Huxley 1952, Hille 2001). However, even from the early days of the science of electrophysiology it was apparent that there must be many other components playing a role. Notably, it has long been apparent that many electrically excitable membranes have a baseline permeability to $K^+$ ions, producing a background, or "leak", current that is largely time and voltage independent (Hodgkin & Huxley 1947, Hodgkin & Katz 1949, Hodgkin & Huxley 1952). These "leak" currents play an important role in regulating cellular excitability by modulating the resting membrane potential; allowing $K^+$ to flow down its concentration gradient from the cytosol to the extracellular solution tends to push the membrane potential towards the $K^+$ reversal potential, hyperpolarizing the membrane. This reduces the excitability of the cell by making it more difficult for a stimulus to reach the threshold voltage to fire an

action potential. Thus, this “leak” current represents an important mechanism for regulating electrical activity in excitable cells.

The main ion channels associated with leak current were identified more than 25 years ago and are now known as part of the $K_{2P}$ (KCNK) family of dimeric potassium channels (Lesage et al. 1996, Fink et al. 1996, Duprat et al. 1997, Fink et al. 1998), which in turn belongs to the larger voltage-gated ion channel (VGIC) superfamily (Yu et al. 2005). Mammalian $K_{2P}$ channels can be divided into six subfamilies (TREK, TWIK, TRESK, THIK, TASK, and TALK), and there are a total of 15 different $K_{2P}$ subunits found in humans (Enyedi & Czirják 2010, Feliciangeli et al. 2015). In the years since their discovery studies have shown that they are much more than simply passive “leak” channels but are instead highly regulated by a large set of factors, allowing cells to finely tune the excitability of their membranes (Renigunta et al. 2015). This central regulatory role for $K_{2P}$ channels means that they are involved in many physiological processes (Kanda et al. 2019, Brohawn et al. 2019, Yoshida et al. 2018, Lazarenko et al. 2010, Madry et al. 2018) and thus they present promising targets for the development of therapeutics aimed at pain (Alloui et al. 2006, Devilliers et al. 2013, Vivier et al. 2017), migraine (Royal et al. 2019), ischemia (Heurteaux et al. 2004, Laigle et al. 2012, Wu et al. 2013), depression (Heurteaux et al. 2006), glaucoma (Yarishkin et al. 2018), pulmonary hypertension (Lambert et al. 2018), lung injury (Zyrianova et al. 2020). An understanding of the structure and molecular mechanisms of regulation in $K_{2P}$ channels is key to this effort.

*Structural features of $K_{2P}$ channels*

Among the broader group of $K^+$ selective channels in the VGIC superfamily, $K_{2P}$ channels stand out for several unique topological features. Each $K_{2P}$ subunit consists of a pair of pore

domains (PD1 and PD2) each containing 2 transmembrane helices (2 TM) in tandem for a total of 4 TM – these are termed M1 through M4 – and no additional voltage sensing domains (**figure B.1A**). Functional channels thus assemble as either homodimers or heterodimers incorporating different $K_{2P}$ subunits (Blin et al. 2016, Blin et al. 2014, Berg et al. 2004, Lengyel et al. 2016, Levitz et al. 2016), giving the typical VGIC arrangement of 4 pore domains, each contributing one pore loop to the selectivity filter. The conserved $K^+$ selectivity filter signature sequence (TxTTxGYGD) is found in all $K_{2P}$ pore domains, albeit with several notable patterns of modification in mammalian $K_{2P}$s: the replacement of the first Thr in PD1 with a hydrophobic residue, the loss of the final Asp in PD1, and the replacement of the PD2 Tyr with Phe (or Leu in TWIK channels).

The first $K_{2P}$ structures, of the TRAAK ($K_{2P}4.1$) and TWIK-1 ($K_{2P}1.1$) channels, were solved in 2012, revealing for the first time the 3D architecture of these channels (Brohawn et al. 2012, Miller & Long 2012) (**figure B.1B**). They both showed an apparently open conformation with no obstruction of the conduction pathway by the inner helices M2 and M4. Overall, the channels had a 2-fold symmetric arrangement, while the pore helices and selectivity filter at the core of the channel exhibited quasi-4-fold symmetry, similar to tetrameric $K^+$ channel structures. Despite the noted idiosyncrasies in the selectivity filter sequences, the filters in these structures were found in the typical $K^+$ channel configuration with the backbone carbonyl and sidechain hydroxyl oxygen atoms of the TxGxG segment pointing into the channel axis to form the four canonical ion coordination sites, S1 through S4.

Despite the quasi-4-fold symmetry of the channel core, there are several clear differences between the $K_{2P}$ PD1 and PD2. Most obviously, in PD1 the first extracellular loop

linking M1 to PH1 (equivalent to the turret loops of fourfold symmetric channels) forms an extended alpha helical structure that projects away from the membrane and has been termed the 'cap' domain (**figure B.1B**). This cap comprises four total alpha helices, two from each channel subunit, and extends by more than 30 angstroms from the extracellular face of the channel, directly above the selectivity filter. Consequently, the mouth of the selectivity filter is partially shielded from the extracellular solution and access to the filter is restricted to a bifurcated aqueous tunnel that extends laterally underneath the cap. The cap domain also allows for another notable feature of the $K_{2P}$ architecture - the dimer is domain-swapped, with M1 of one subunit packed against M2 and PH1 of the other subunit (**figure B.1C**). In addition, another key difference between pore domains is that in PD2 the second extracellular loop linking SF2 to the M4 helix is typically 12-14 residues long – the one exception being TRESK ($K_{2P}$18.1) – compared to 6 in the $K_{2P}$ PD1 and most tetrameric $K^+$ channels. Studies have pointed to this SF2-M4 loop as a key functional element (Sandoz et al. 2009), and its additional length over the standard loop in most other $K^+$ channel pore domains has important consequences for the role of the selectivity filter in $K_{2P}$ gating (Lolicato et al. 2020).

As additional $K_{2P}$ structures became available it became apparent that portions of the TM helices showed substantial conformational plasticity. This was first apparent in higher resolution structures of a TRAAK-fab complex in which the C-terminal portion of the M4 helix was found in different conformations in each of the two channel subunits (Brohawn et al. 2013, Brohawn et al. 2014). In the first conformation M4 remains approximately linear as it crosses the membrane at a roughly 45 degree angle and makes no contacts with the M2 helix of the opposite subunit, instead leaving a 5-10 angstrom fenestration that exposes the aqueous

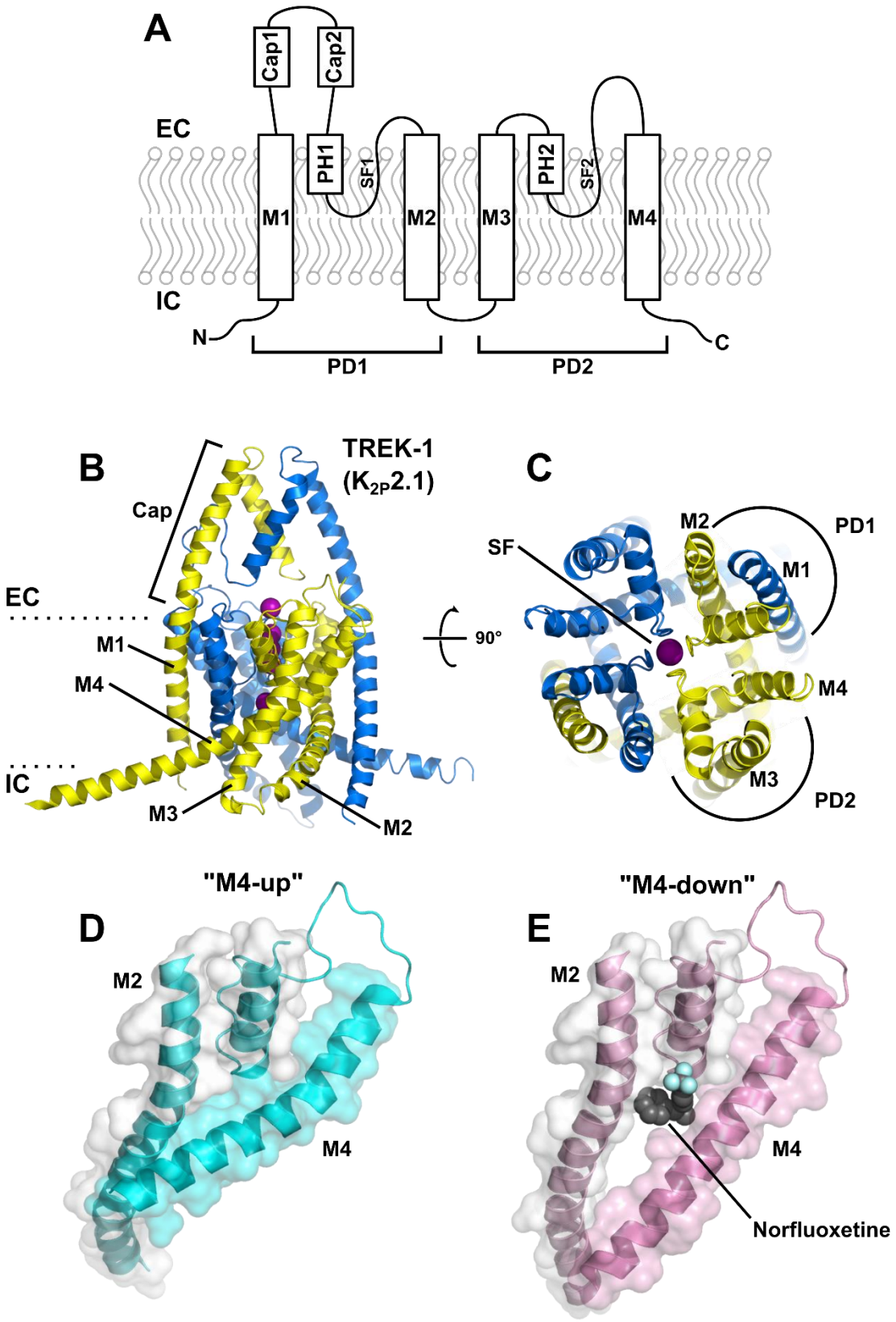


**Figure B.1: Structural features of $K_{2P}$ channels**

**Figure B.1 Legend. (A)** Membrane spanning topology of $K_{2P}$ channels, with helices and the locations of the selectivity filter (SF1 & SF2) labeled. **(B)** Side view in the membrane plane of the structure of TREK-1 ($K_{2P}$2.1) from PDBID 6CQ6 (Lolicato et al. 2017). Subunits A and B are colored yellow and blue, respectively, while $K^+$ ions are purple. Transmembrane helices and cap domain are labeled. **(C)** Top view without cap from the extracellular side of the membrane of the same structure as in **(B)**. Pore domains and selectivity filter are labeled. **(D)** Select elements of the structure of TREK-2 ($K_{2P}$10.1) from PDBID 4BW5 (Dong et al. 2015) showing the "M4-up" state. **(E)** Select elements of the structure of TREK-2 from PDBID 4XDK (Dong et al. 2015) showing the "M4-down" state bound to the inhibitor norfluoxetine (spheres).

intracellular cavity to the membrane core. In the second conformation M4 bends at its midpoint near a conserved Gly (G260 in human TRAAK) by approximately 25 degrees, which causes the C-terminal half of M4 to pack against M2 and close the fenestration – but importantly does not obstruct the ion pathway. These two conformations have been termed 'M4-down' and 'M4-up' respectively.

Subsequent structural studies reinforced this finding with TREK-2 ($K_{2P}$10.1) being crystalized in two different conformations – one with both M4 helices 'up' and the other with both 'down' (Dong et al. 2015) (**figure B.1 D & E**). The same study also found that the binding site for the TREK inhibitor fluoxetine and its derivatives was in the fenestration between M4 and M2 that is only open in the down state. Several other studies have also shown that lipid or detergent acyl chains can occupy this fenestration site in TWIK-1 and TRAAK (Miller & Long 2012, Brohawn et al. 2014), leading to the hypothesis that lipids gate the channel shut by entering the fenestration and occluding the selectivity filter in the 'M4-down' configuration, but are excluded in 'M4-up', leading to higher activity. Subsequent experiments have however shown that the selectivity filter remains accessible and can still be opened in the 'M4-down' state, suggesting that regulation by M4 motions is more complicated than simply allowing for a

lipid block (Piechotta et al. 2011, Rapedius et al. 2012, McClenaghan et al. 2016, Aryal et al. 2017).

Indeed, there does not appear to be a strict correspondence between 'M4-down' = inactive and 'M4-up' = active. Two different TRAAK variants carrying activating mutations were crystalized with both M4s in the 'down' conformation – in both cases the activating mutations were located at the interface of M4 with PH1 (Lolicato et al. 2014). More recently, structures of TREK-1 ($K_{2P}$2.1) have revealed a cryptic small molecule binding site at the interface between M4 and PH1, directly adjacent to the selectivity filter; activators which bind at this site greatly increase the $P_o$ of TREK-1 without any apparent changes in the conformation of the C-terminal portion of M4, which has been found in the 'up' conformation in all TREK-1 structures to date (Lolicato et al. 2017, Pope et al. 2020, Lolicato et al. 2020). Altogether, this structural information and a number of functional studies (Piechotta et al. 2011, Bagriantsev et al. 2011, Bagriantsev et al. 2012, Rapedius et al. 2012) suggest a paradigm for TREK family channels in which all regulatory inputs converge on a gate at the selectivity filter, with the conformation of the M4 helix – which senses intracellular pH, temperature, membrane tension, and lipid binding (Maingret et al. 1999, Maingret et al. 2000a, Maingret et el. 2000b, Honoré et al. 2002, Chemin et al. 2005) – allosterically coupled to this gate.

# CHAPTER 1: $K_{2P}$ channel C-type gating involves asymmetric selectivity filter order-disorder transitions

## INTRODUCTION

$K_{2P}$ channels regulate nervous, cardiovascular, and immune system functions (Enyedi et al. 2010, Feliciangeli et al. 2015) through the action of their selectivity filter (C-type) gate (Bagriantsev et al. 2011, Piechotta et al. 2011, Bagriantsev et al. 2012, Schewe et al. 2016). C-type gating occurs in many potassium channel classes and displays a hallmark sensitivity to external potassium due to its dependency on interactions between the permeant ions and selectivity filter (López-Barneo et al. 1993, Baukrowitz & Yellen 1995, Pardo et al. 1992, Cohen et al. 2008, Cordero-Morales et al. 2006, Hoshi & Armstrong 2013). Although structural studies of exemplar homotetrameric potassium channels have uncovered various types of selectivity filter rearrangements attributed to C-type gating (Cordero-Morales et al. 2006, Zhou & MacKinnon 2003, Zhou et al. 2001, Cuello et al. 2017, Cuello et al. 2010, Wang & MacKinnon 2017, Pau et al. 2017, Matthies et al. 2018), there remains a debate about whether the essence of C-type gating involves pinching, dilation, or more subtle selectivity filter changes. Furthermore, although structural studies of different $K_{2P}$ family members have revealed changes in the transmembrane helix conformations that affect activity (Lolicato et al. 2017, Dong et al. 2015, Brohawn et al. 2012, Brohawn et al. 2013, Lolicato et al. 2014, Miller & Long 2012), no selectivity filter conformational changes that could explain how $K_{2P}$ C-type gating occurs have been observed (**figure 1.1 and table 1.1**). This lack of a structural framework has left open questions regarding the extent to which $K_{2P}$ C-type gating mechanisms resemble

homotetrameric channels and whether the innately heterodimeric $K_{2P}$ selectivity filter architecture confers unique properties to their C-type gates. Here we show molecular dynamics and functional studies, which in combination with x-ray crystallography of TREK-1 ($K_{2P}$2.1) in different potassium concentrations and potassium anomalous scattering (the latter two datasets can be found in the full length published version of this work, Lolicato et al. 2020), uncover extraordinary, asymmetric, potassium-dependent structural changes that trigger $K_{2P}$ C-type gating. We show that low potassium concentrations evoke conformational changes in selectivity filter strand 1 (SF1), selectivity filter strand 2 (SF2), and the SF2-transmembrane helix 4 loop (SF2-M4 loop) that destroy the S1 and S2 ion binding sites through a mixture of pinching of SF1 and dilation of SF2, leveraging the fundamentally heterodimeric nature of the $K_{2P}$ selectivity filter to exploit two classes of C-type gating mechanisms. Both C-type gate rearrangements are suppressed by binding of the activator ML335 (Lolicato et al. 2017) to the $K_{2P}$ modulator pocket in the P1-M4 interface, providing an explanation for how such compounds stabilize the activated state. Shortening the uniquely long SF2-M4 loop to match the canonical length found in the first $K_{2P}$ pore domain (PD1) and in other potassium channels or disrupting the conserved hydrogen bond network centered on Glu234 from the M3 helix that supports the SF2-M4 loop, the "M3 glutamate network" blunts C-type gate responses to various physical and chemical stimuli. Destabilization of the M3 glutamate network compromises ion selectivity but can be reversed by channel activation, indicating that loss of S1 and S2 ions and associated selectivity filter changes reduce ion selectivity, similar to other channels (Derebe et al. 2011). Together, our data establish that C-type gating occurs through potassium-dependent order-disorder transitions in the selectivity filter and adjacent loops that

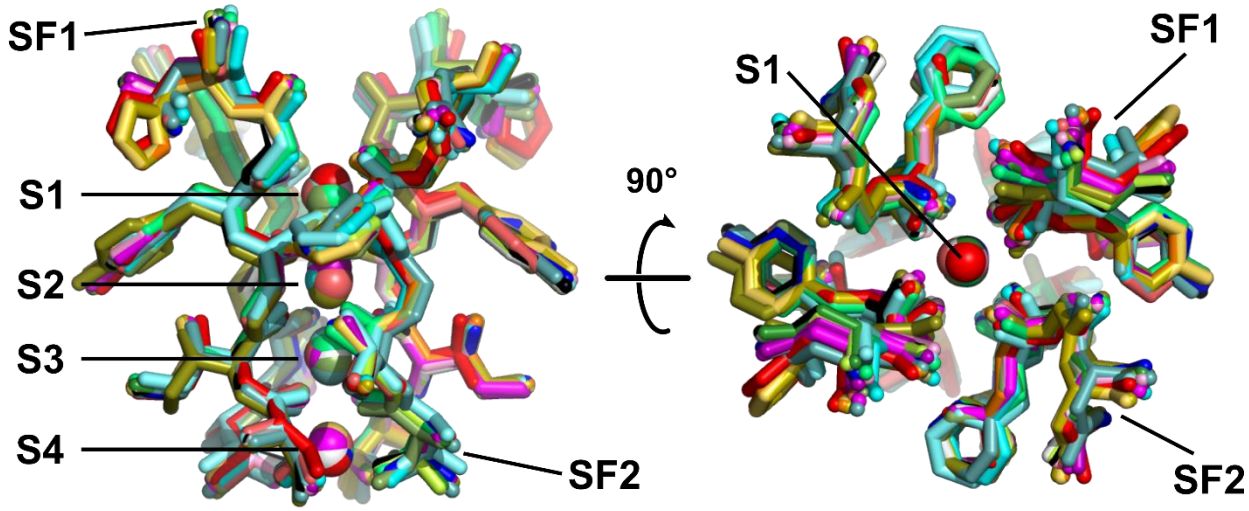


**Figure 1.1: $K_{2P}$ channel selectivity filters structure comparison**

**Figure 1.1 Legend**. Superposition of the selectivity filters and permeant ions from $K_{2P}$ structures extant as of 2020: TREK-1 ($K_{2P}$2.1) 6CQ6 (Lolicato et al. 2017) (smudge), TREK-1:ML335 6CQ8 (Lolicato et al. 2017) (deep salmon), TREK-1:ML402 (cyan) 6CQ9 (Lolicato et al. 2017); TREK-2 ($K_{2P}$10.1) 4BW5, (Dong et al. 2015) (pink), 4XDJ (Dong et al. 2015) (magenta), 4XDK (Dong et al. 2015) (purple); TRAAK ($K_{2P}$4.1) 3UM7 (Brohawn et al. 2012) (aquamarine), 4I9W (Brohawn et al. 2013) (limon), 4WFE (forest green) (Brohawn et al. 2014), 4WFF (white) (Brohawn et al. 2014), 4WFG (grey) (Brohawn et al. 2014), 4WFH (black) (Brohawn et al. 2014); TRAAK G124I 4RUE (blue) (Lolicato et al. 2014); TRAAK W262S 4RUF (lime green) (Lolicato et al. 2014); TWIK-1 ($K_{2P}$1.1) 3UKM (Miller & Long 2012) (red); TASK-1 ($K_{2P}$3.1) 6RV2 (orange) (Rödström et al. 2020), TASK-1:BAY1000493 6RV3 (yellow orange) (Rödström et al. 2020), TASK-1:BAY2341237 6RV4 (olive) (Rödström et al. 2020). SF1, SF2 and ion binding positions, S1-S4, are indicated. Ions are shown as spheres and colored according to the parent structure. **Table 1.1** lists permeant ion concentration in crystallization conditions for each structure and RMSD for all selectivity filter backbone atoms relative to TREK-1 6CQ6. Structures with two RMSD values have two dimeric channels per asymmetric unit.

respond to gating cues relayed through the SF2-M4 loop. These findings underscore the importance of the SF2-M4 loop as a conduit for signals sensed by the cytoplasmic tail and transmitted through the M4 transmembrane helix (Bagriantsev et al. 2011, Bagriantsev et al. 2012) and highlight the potential for targeting the SF2-M4 loop for the development of new, selective $K_{2P}$ channel modulators.

## RESULTS

*C-type gate and connecting loops are dynamic*

Structure determination of TREK-1 over a range of [$K^+$] concentrations, from 0 mM to 200 mM, showed marked potassium dependent changes in the selectivity filter structure (Lolicato et al. 2020). At [$K^+$] lower than 50 mM there was evidence of a partial loss of electron density in the loop linking SF2 to the M4 transmembrane helix (SF2-M4 loop) along with a dilation of the selectivity filter strand 2 (SF2), as well as smaller changes in selectivity filter strand 1 (SF1). Notably, potassium anomalous scattering data showed that upper portion of the selectivity filter became depleted in ions under these low [$K^+$] conditions, while ions were retained at sites S3 & S4. On the other hand, the same experiments in the presence of the TREK-1 small molecule activator ML335 (Lolicato et al. 2017) yielded structures with a canonical, fully $K^+$ occupied selectivity filters which were essentially identical to one another across all [$K^+$].

To gain additional molecular insight into how potassium occupancy and ML335 affect the C-type gate, particularly in the context of a lipid bilayer, we turned to molecular dynamics (MD) simulations of TREK-1. Initially, we simulated two conditions: (i) 180 mM [$K^+$] and a +40 mV applied membrane potential (denoted "High [$K^+$]/+40 mV"; 36.5 μs aggregate) and (ii) the same [$K^+$] and potential with bound ML335 (denoted "High [$K^+$]/+40 mV/ML335"; 31.6 μs aggregate). We observed many permeation events in both conditions (144 and 253 for High [K+]/+40 mV and High [K+]/+40 mV/ML335, respectively), confirming that the initial structures represent conduction competent states. Nevertheless, the pattern of permeation events over time showed notable differences depending on ML335 (**figure 1.2 A**). Over the course of the

simulations, most of the High [K+]/+40 mV/ML335 trajectories (8 of 10) remained in a stable, ion-conducting state. By contrast, most (7 of 12) of the High [K+]/+40 mV trajectories entered long-lived (>1 μs) nonconducting states from which they did not recover and that were characterized by obvious disruptions of the initial selectivity filter conformation. Concordantly, the two conditions had a substantial difference in average conductance (~8 pS versus ~32 pS for High [K+]/+40 mV and High [K+]/+40 mV/ML335, respectively) (**figure 1.2 B**). There were no major changes during the simulations in the M4 helix position or in other parts of the channel outside of the selectivity filter when compared with their starting positions as defined by the crystal structures.

To determine whether there were differences in C-type gate dynamics across simulation conditions, we examined a number of factors. Because structural waters behind the selectivity filter stabilize both the active and C-type inactivated states of the model homotetrameric channel KcsA (Ostmeyer et al. 2013), we first characterized the role that water molecules have on the TREK-1 filter conformation. We found that in conductive states, regardless of the presence of ML335, a characteristic water network behind the filter stabilized SF1 and SF2 through hydrogen bonds to the backbone amides of Phe145/Gly146 and Phe254/Gly255, respectively (**figure 1.3 A & B**). As the TREK-1 filter moves away from the canonical, conductive conformation, these well-organized networks dissolve (**figure 1.3 C & D**). Nevertheless, before dissolution, there were no obvious differences in the water configurations with or without ML335 that would explain the differences in conduction and filter stability. We also note that unlike in KcsA, where water molecules stabilize a discrete non-conducting pinched filter state (Cordero-Morales et al. 2006, Zhou et al. 2001, Ostmeyer et al. 2013), these TREK-1

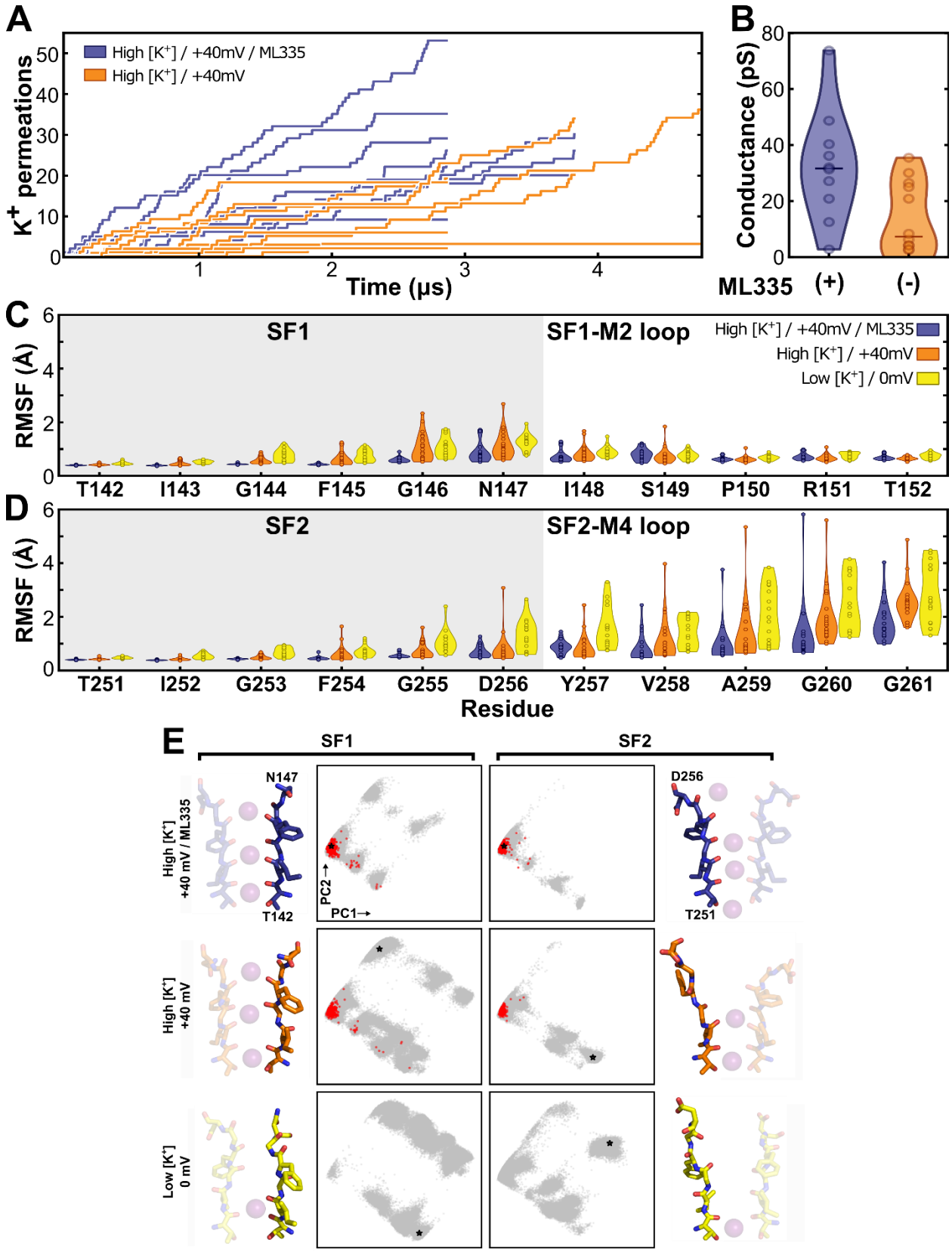


**Figure 1.2: TREK-1 conductance properties and SF conformational dynamics from MD simulations**

**Figure 1.2 Legend. (A)** Cumulative $K^+$ ion permeation events over simulation time for all individual trajectories in High [$K^+$]/+40 mV (orange) and High [$K^+$]/+40 mV/ML335 (purple) conditions. **(B)** Conductance calculated from the trajectories in **(A)**. Each point shows the average conductance from one independent trajectory; horizontal bars indicate median. **(C) & (D)** $C_\alpha$ RMSF values of the filter and loop regions for **(C)** pore domain 1 and **(D)** pore domain 2, for all simulated conditions. Each point represents RMSF calculated from one TREK-1 subunit of one trajectory. Conserved selectivity filter signature sequences are shaded gray. **(E)** PCA analysis of SF1 and SF2 dihedral angles and exemplar filter conformations. Each dot represents the instantaneous conformation of the TIGFG backbone dihedral angles from single selectivity filter. Black stars indicate the location in PC1 vs. PC2 space of the adjacent exemplar. Red dots indicate conformations immediately preceding $K^+$ permeation events.

nonconductive states were heterogeneous, having many different conformations of the filter and surrounding waters (**figure 1.3 C-D**).

We next asked whether dynamics in protein elements near the filter could explain differences in filter stability. To do so, we calculated root-mean-square fluctuation (RMSF) values for the selectivity filter and the postfilter loops. Because crystal structures showed that low potassium occupancy in the filter resulted in increased mobility in these regions (Lolicato et al. 2020), we included a third set of simulations in which TREK-1 had only a single ion in the filter and no membrane potential was applied (denoted "Low [$K^+$]/0 mV," 20.6 μs aggregate). This analysis revealed that residues Phe145-Ser149 of SF1, Phe254-Gly261 of SF2, and the SF2-M4 loop comprise the three most dynamic areas near the filter and showed that their mobility was greatly restricted by ML335 (**figures 1.2 C & D**). Furthermore, under Low [$K^+$]/0 mV conditions, the mobility of these regions exceeded either of the High [$K^+$]/+40 mV conditions. Together, the simulations indicate that the absence of $K^+$ in the filter versus the presence of ML335 have strong, opposite effects on the dynamics of the selectivity filter and SF2-M4 loop (**figures 1.2 C & D and 1.4**).

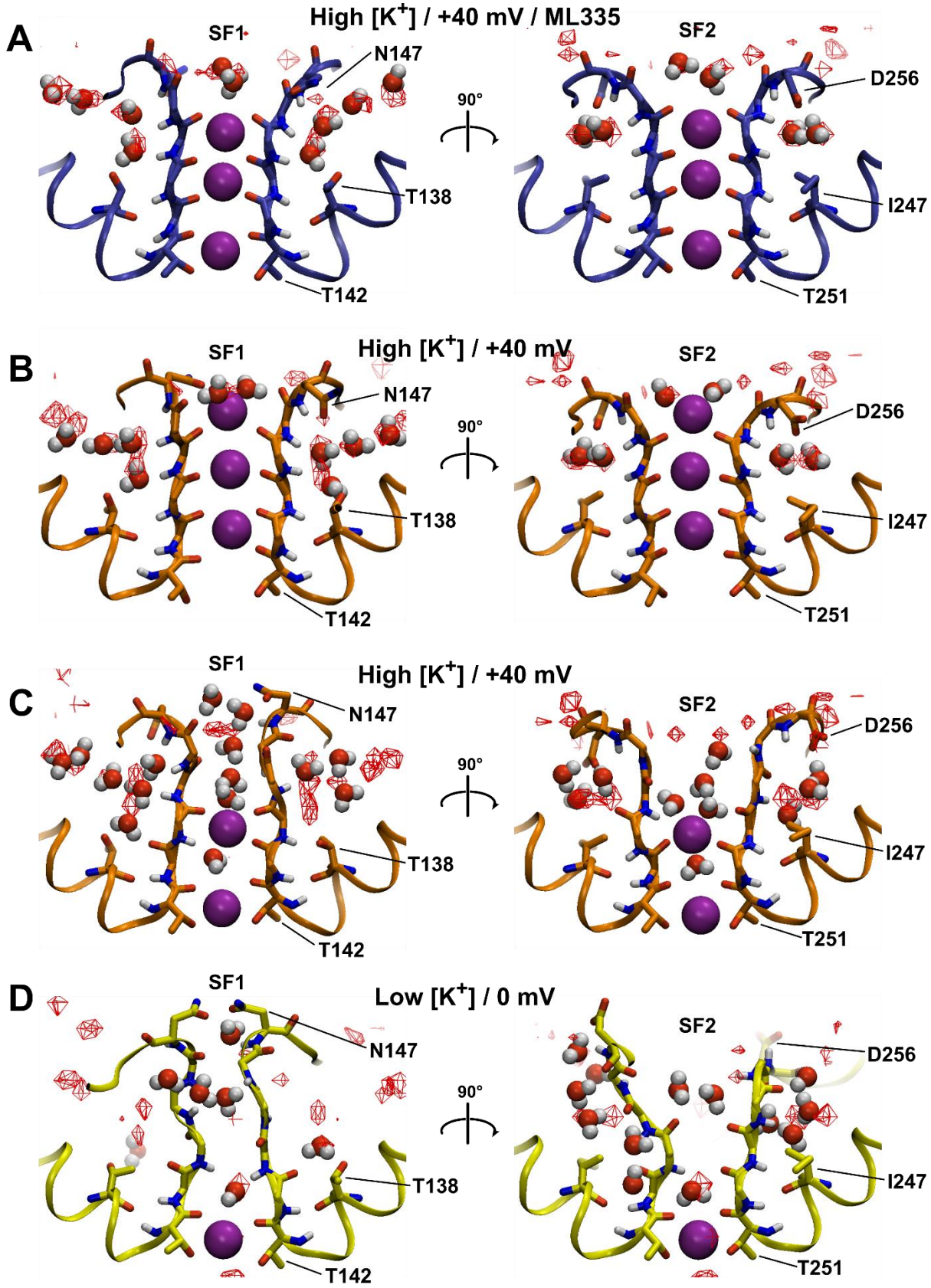


**Figure 1.3: Water interactions with the selectivity filter**

**Figure 1.3 Legend. (A)** Final frame of High [$K^+$]/+40 mV/ML335 simulation 4, showing SF1 (left) and SF2 (right). **(B)** Final frame of High [$K^+$]/+40 mV simulation 12. **(C)** Final frame of High [$K^+$]/+40 mV simulation 21. **(D)** Final frame of Low [$K^+$]/0 mV simulation 29. In all panels, water molecules interacting with the extracellular face of the selectivity filter are shown as spheres. Water oxygen atom occupancy maps calculated from the simulation data are shown as red mesh and are contoured at the same level (density contains voxels with occupancy >7%) in all panels. Maps in **(A)** and **(D)** were calculated from all High [$K^+$]/+40 mV/ML335 and Low [$K^+$]/0 mV simulation trajectories, respectively. Map in **(B)** and **(C)** was calculated from all High [$K^+$]/+40 mV simulation trajectories. **(C)** and **(D)** show examples where filters have become disordered.

To determine specific structural features associated with loss of conduction and how these features relate to the broader C-type gating context, we analyzed the backbone dihedral angles of the SF1 and SF2 ion-coordinating "TIGFG" amino acid motifs. We used a simple statistical procedure known as principal component analysis (PCA) to transform the 10 backbone dihedral angles from each TIGFG conformation into a new coordinate system wherein the greatest variance in conformations lies along the first axis (principal component), the second greatest along the second axis, and so on (Altis et al. 2007). Focus on the first few high-variance components provides a natural way of reducing the dimensionality of the data and reveals collective changes that cannot be gleaned from examining changes in individual dihedral angles. Projecting all simulation snapshots onto the first two principal components (PC1 and PC2) (**figure 1.2 E**) uncovered a distinct grouping of SF1 and SF2 conformations that lack major deviations from the initial structure. All prior $K_{2P}$ selectivity filter structures (**figure 1.5 A&B**) (denoted as the "native state") and selectivity filters from other potassium channels thought to capture either conducting states (Zhou et al. 2001, Long et al. 2007) or, unexpectedly, C-type inactivated states (Zhou et al. 2001, Pau et al. 2017), map to the center of this group (**figure 1.5 C**). Additional clustering analysis of all High [$K^+$] selectivity filters in the PC1 to PC3 space separated out many distinct clusters of non-native conformations in which

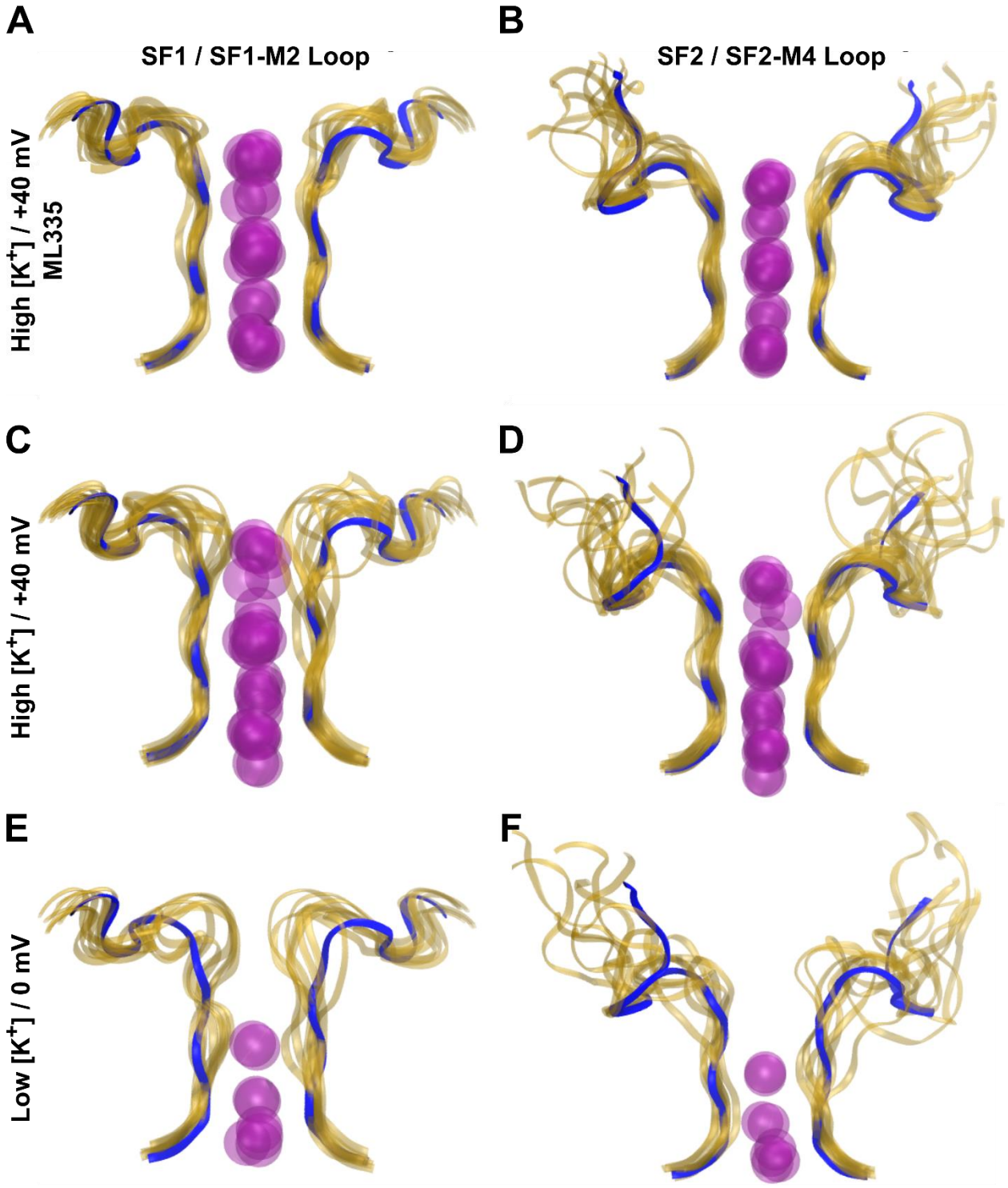


**Figure 1.4: Final filter states from all simulations**

**Figure 1.4 Legend.** Final SF1 **(A,C,E)** and SF2 and loop **(B,D,F)** ion and backbone conformations from all simulation trajectories; **(A) & (B)** are from High K+ / +40 mV / ML335, **(C) & (D)** are from High K+ / +40 mV, and **(E) & (F)** are from Low K+ / +0 mV. Transparent gold ribbons represent the protein state in the final frame of each trajectory; transparent purple spheres are potassium ions. Solid blue ribbons represent the initial crystal structure conformation.

the backbone dihedral angles deviate substantially from the native state (**figure 1.5 D**). Some of these conformations are reached from the canonical SF1 structure via a single discrete backbone "crankshaft" motion between either the S2 and S3 sites (Ile143/Gly144) (**figure 1.5 D, cluster 2**) or at the top of the S0 site (Gly146/Asn147) (**figure 1.5 D, cluster 3**) that result in a flip of the amide group plane that reorients the backbone carbonyl away from the pore and correspond to conformations suggested to be involved in C-type gating in previous $K_{2P}$ channel simulations (Brennecke & de Groot 2018, Harrigan et al. 2017). The remaining SF1 and SF2 clusters represent larger deviations from the initial state and cannot be described by single amide crankshaft motions. Some of these configurations are reminiscent of the unusual selectivity filter structure of the nonselective channel NaK (**figure 1.5 C&D**) (Shi et al. 2006), while others represent novel conformations that have not been observed experimentally (**figure 1.5 D**). Notably, conformations with multiple crankshaft motions and large dihedral angle changes are more highly populated in the absence of ML335 and are especially abundant under Low [$K^+$] conditions (**figure 1.2 E**).

Of all the TREK-1 selectivity filter conformations observed under high [$K^+$] conditions, only a few are compatible with $K^+$ permeation. Greater than 90% of ion conduction events occurred when all four SF strands occupied the native state conformational cluster. No conduction events were observed when more than two SF strands adopted nonnative states. Under High [$K^+$]/+40 mV/ML335 conditions, SF1 and SF2 were found in the native state cluster

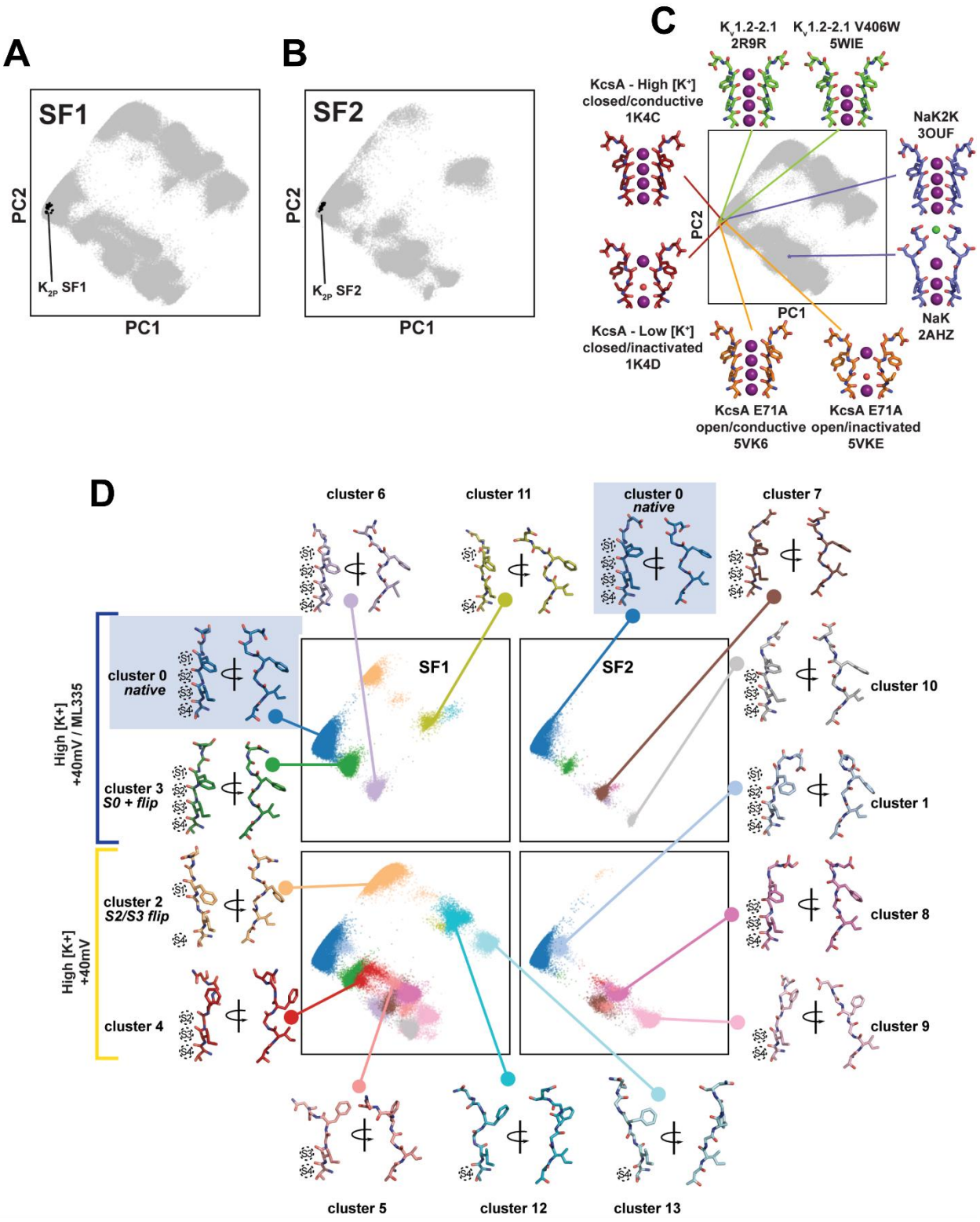


**Figure 1.5: TREK-1 principle component analysis (PCA)**

**Figure 1.5 Legend. (A) & (B)** PCA projection of selectivity filter conformations for SF1 **(A)** and SF2 **(B)**. Grey points indicate TREK-1 conformations from all simulations in this work; black points represent projections of SF1 and SF2 conformations obtained from the structures shown in **figure 1.1**. **(C)** Representative non-$K_{2P}$ selectivity filter conformations and their projections into PCA space. Grey points indicate TREK-1 conformations from all simulations (SF1 and SF2). Lines and colored points show the PCA projected location of SF conformations from the indicated tetrameric potassium channel crystal structures: KcsA closed/conductive (1K4C) and closed/inactivated (1K4D) (Zhou et al. 2001) (firebrick); Kv1.2-2.1 chimera (2R9R) (Long et al. 2007) and V406W mutant (5WIE) (Pau et al. 2017) (chartreuse); NaK (2AHZ) (Shi et al. 2006) and $K^+$ selective mutant NaK2K (3OUF) (Derebe et al. 2011) (slate); and KcsA E71A open/conductive (5VK6) and open/inactivated (5VKE) (Cuello et al. 2017) (orange). (D) Hierarchical clustering of SF conformations from all High [$K^+$] simulations. Clustering was performed on PC1-3, for clarity only PC1 and PC2 are shown. Points representing selectivity filter conformations in PCA space are colored according to their membership in one of 14 identified clusters. A single representative conformation is shown for each cluster, with the exception of the native state (cluster 0) for which representative conformations from both SF1 and SF2 are shown. For each representative conformation potentially intact (whether or not it is actually intact depends on all four strand conformations) ion binding sites are indicated with dotted circles.

90 and 95% of the time, respectively, while under High [$K^+$]/+40 mV conditions, these values dropped to 64 and 86% (**figure 1.2 E**). Thus, the presence of ML335 reduces the accessible conformational space of the filter, restricting SF1 and SF2 largely to their native, conductive conformations. This conformational restriction causes longer periods of sustained conduction and higher current values relative to the High [$K^+$]/+40 mV condition (**figure 1.2 A&B**), in line with the fact that ML335 directly activates the TREK-1 C-type gate (Lolicato et al. 2017).

In all three simulation conditions, most of the nonconductive filter conformations have multiple dihedral angle deviations from the canonical structure and share a loss of ion binding sites at S1, S2, or both due to rearrangement of the ion coordinating carbonyls (**figure 1.2 E, bottom and middle right; and figure 1.5 D**). These changes leave only the S3 and S4 sites competent for potassium binding and are in excellent agreement with crystallographic ion positions observed under low potassium conditions (**figure 1.4 E&F**) (Lolicato et al. 2020).

Furthermore, examination of the ensemble of final SF1 and SF2 backbone conformations from the simulations under different conditions shows that these structural components display increased conformational disorder and pseudo-fourfold symmetry breaking that is in excellent agreement with TREK-1 x-ray structures (**figure 1.4 A-F**) (Lolicato et al. 2020). SF1 adopts nonnative conformations, particularly around Asn147, which pinch the conduction pathway, whereas SF2 preferentially dilates out of the pathway. This asymmetry extends beyond the parts of the filter that directly contact the permeant ions. Although the SF1-M2 loop remains largely native-like, despite the changes in SF1, the longer SF2-M4 loop is highly mobile. This later observation agrees well with the loss of density for SF2-M4 loop in TREK-1 low [$K^+$] crystal structures (Lolicato et al. 2020). These simulations, together with structural data, support the idea that ML335 acts by stabilizing the $K_{2P}$ selectivity filter in a conductive state and indicate that the low [$K^+$] crystal structures represent an inactive C-type gate in which asymmetric disorder in the extracellular portion of the selectivity filter disrupts the S1 and S2 ion binding sites and inhibits ion conduction (Lolicato et al. 2020).

*The SF2-M4 loop integrates responses from diverse gating cues*

In most potassium channels, including the first $K_{2P}$ pore domain (PD1), a six-residue loop connects the extracellular end of the selectivity filter to the outer transmembrane helix of the pore domain (**figures 1.6 A & B and 1.7 A & B**). $K_{2P}$s are unique in that the second pore domain loop (PD2) is longer than this canonical length by six to eight residues in 14 of the 15 $K_{2P}$ subtypes (**figure 1.6 F**). Despite these differences, the N-terminal portions of the PD1 and PD2 loops adopt very similar structures up to Pro150 and Ala259, respectively (**figure 1.6 A**). The simulations revealed that loss of SF2-M4 loop stability was accompanied by the disruption of a

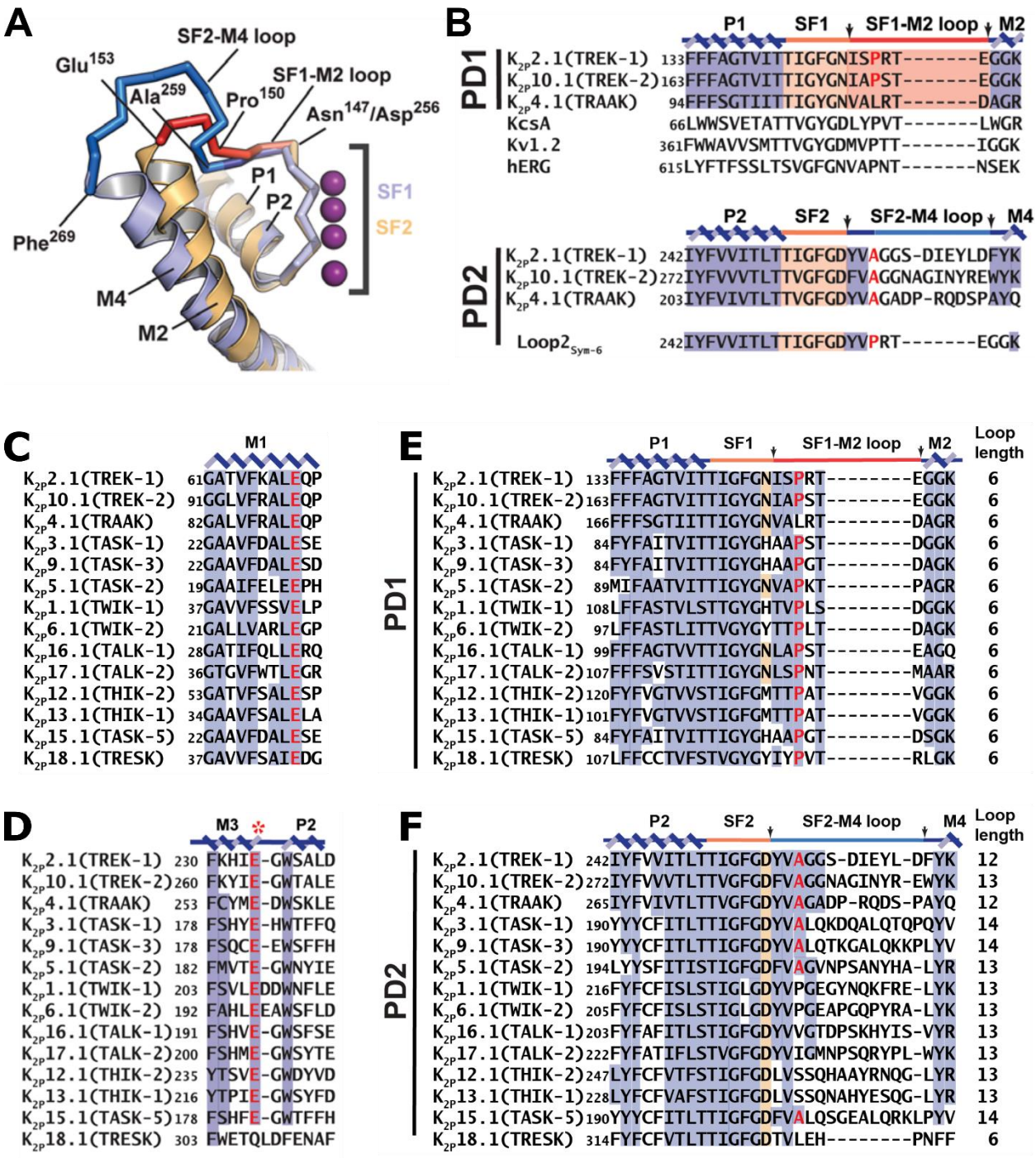


**Figure 1.6: $K_{2P}$ channel pore domain comparisons**

**Figure 1.6 Legend. (A)** TREK-1 P1-SF1-M2 (orange) and P2-SF2-M4 (slate) superposition. SF1-M2 loop (red) and SF2-M4 loop (blue) and portions having a shared conformation (dark blue) are indicated. Residue labels indicate the SF1-M2 and SF2-M4 loop ends and structural divergence point (Pro150/Ala259). **(B)** Sequence alignment of PD1 (top) & PD2 (bottom) for the indicated channels. P1, M2, P2, and M4 helices (blue), SF1 and SF2 (orange), and SF1-M2 loop (red) are indicated. Arrows denote the boundaries of the SF1-M2 loop. **(C) & (D)** Sequence alignment of M1 **(C)** and M3/P2 **(D)** for the indicated $K_{2P}$ channels. TREK-1 Glu69, Glu234, and equivalent positions in other channels are indicated with '*' and red text. Conserved residues are shaded in slate. **(E) & (F)** Sequence alignment of pore helix-selectivity filter-loop regions in PD1 **(E)** and PD2 **(F)** for the indicated $K_{2P}$ channels. Conserved residues are shaded in slate. Conserved selectivity filter Asn/Asp is shaded orange. TREK-1 Pro150, Ala259, and equivalent positions in other channels are shaded red. Sequences are from human $K_{2P}$ channels: $K_{2P}$2.1 (TREK-1) AAD47569.1, $K_{2P}$10.1 (TREK-2) NP_612190.1, $K_{2P}$4.1 (TRAAK) AAI10328.1, $K_{2P}$3.1 (TASK-1) NP_002237.1, $K_{2P}$9.1 (TASK-3) NP_001269463.1, $K_{2P}$5.1 (TASK-2) NP_003731.1, $K_{2P}$1.1(TWIK-1) NP_002236.1, $K_{2P}$6.1 (TWIK-2) NP_004814.1, $K_{2P}$16.1 (TALK-1) NP_115491.1, $K_{2P}$17.1(TALK-2) AAK28551.1, $K_{2P}$12.1 (THIK-2) NP_071338.1, $K_{2P}$13.1 (THIK-1) NP_071337.2, $K_{2P}$15.1 (TASK-5) EAW75900.1, $K_{2P}$18.1 (TRESK) NP_862823.1. SF1 and SF2 sequence and numbers for $K_{2P}$2.1 (TREK-1)$_{cryst}$ (PDBID:6CQ6) (Lolicato et al. 2017) are identical to that of $K_{2P}$2.1 (TREK-1) AAD47569.1.

hydrogen bonding network, the Glu234 network, at the C-terminal end of the PD2 linker involving the M3 Glu234 carboxylate, the SF2-M4 loop Gly260 backbone amide, and the M4 Tyr270 phenolic –OH (**figure 1.7 B & C**). Binding of ML335 to the $K_{2P}$ modulator pocket stabilizes the SF2-M4 loop from the opposite side of the Glu234 network (**figure 1.7 A**), increases the strength of the Glu234 hydrogen bonding network in the simulations (**figure 1.7 B & C**), and strongly attenuates potassium-dependent loop dynamics (**figure 1.2 D**). Conversely, in low [$K^+$] simulations, the Glu234 network is disrupted (**figure 1.7 B & C**), and loop dynamics are enhanced (**figure 1.2 D**). Together, these results suggest that loop dynamics are important for C-type gating, with Glu234 playing a key role by supporting the SF2-M4 loop structure. Notably, the equivalent position in the $K_{2P}$ PD1 outer helix, M1, also has a highly conserved glutamate (**figure 1.6 C**) that affects C-type gating through interactions with the short SF1-M2 loop (Cohen

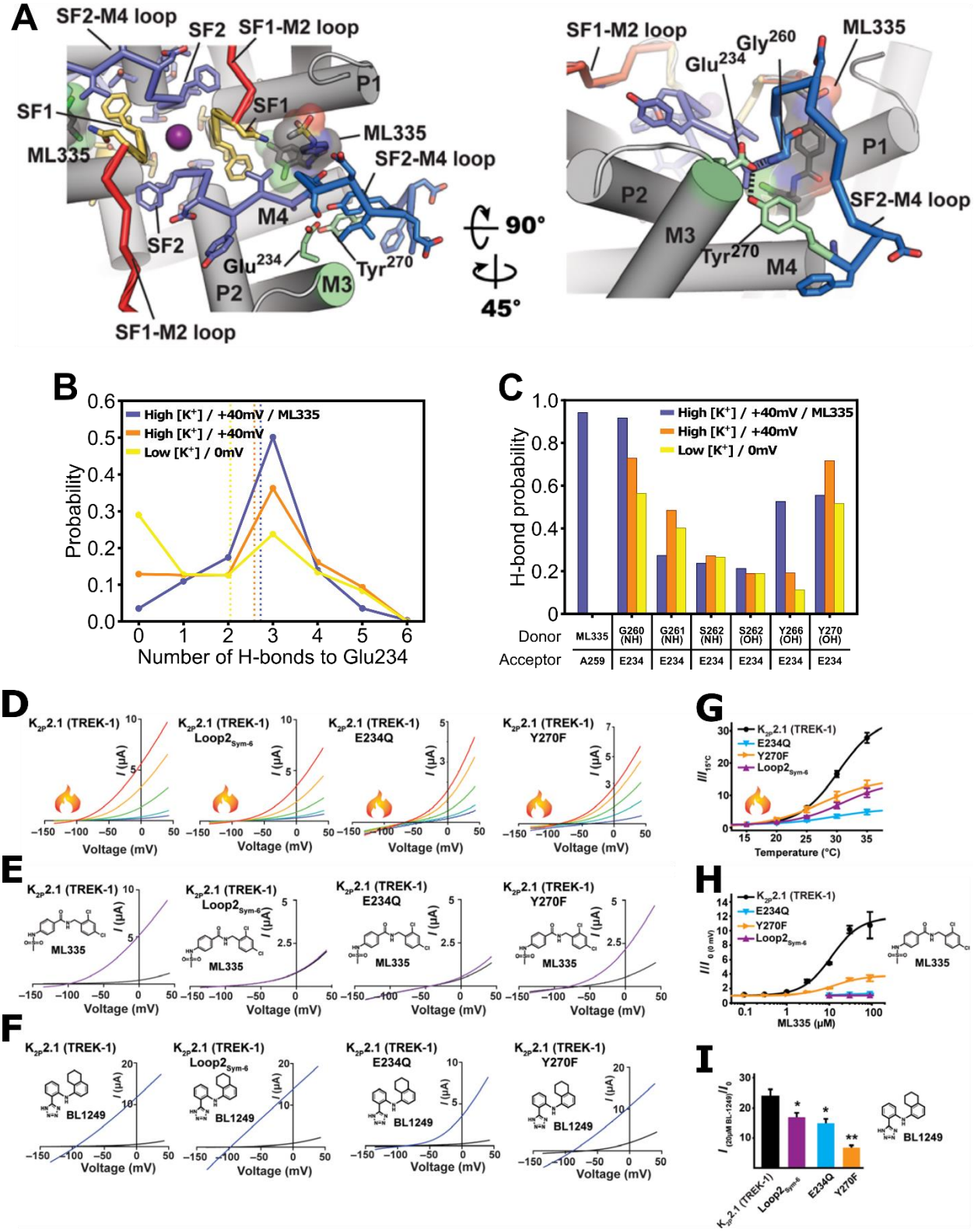


**Figure 1.7: The $K_{2P}$ SF2-M4 loop is central to C-type gate function**

**Figure 1.7 Legend. (A)** TREK-1:ML335 complex (grey) with a view showing the SF1-M2 loop. SF1-M2 loop (red) and SF2-M4 loop (blue), and key residues of the conserved Glu234 hydrogen bond network (Glu234 & Tyr270) are indicted in light green. ML335 is shown in sticks with a transparent surface. **(B)** Per-frame probability of finding a particular number of hydrogen bonds to the Glu234 sidechain carboxylate in all TREK-1 simulations. Dotted lines indicate the overall average number of hydrogen bonds calculated for each simulation condition. **(C)** Per-frame probability of a hydrogen bond between the indicated groups in all TREK-1 simulations. **(D)** Exemplar two electrode voltage clamp (TEVC) recordings at 15°C (blue), 20°C (light green), 25°C (lime green), 30°C (orange), and 35°C (red). **(E)** Exemplar TEVC recordings for 30 μM ML335 (purple) activation. **(F)** Exemplar TEVC recordings for 20 μM BL-1249 (blue) activation. **(G)** Normalized temperature responses (n ≥ 10). **(H)** ML335 dose-response curves (n ≥ 3). EC50 11.3 ± 3.4 and 12.7 ± 4.1 μM, maximum activation 11.9 ± 1.3, and 3.8 ± 0.4 fold for TREK-1 WT and TREK-1 Y270F, respectively. **(I)** Normalized responses to 20 μM BL-1249 (n ≥ 7). **(G), (H), & (I)** show TREK-1 (black), TREK-1 Loop2$_{sym6}$ (purple), TREK-1 E234Q (light blue), and TREK-1 Y270F (orange). "*" and "**" indicate $P < 0.05$ and $P < 0.001$, respectively.

et al. 2008, Zilberberg et al. 2001) in a manner that is conserved with voltage-gated potassium channels (Larsson and Elinder 2000, Ortega-Sáenz et al. 2000). Therefore, given the indications from our simulations and structures (Lolicato et al. 2020) that Glu234 network integrity should be important for gating, we set out to test consequences of restricting the SF2-M4 loop mobility and disrupting the Glu234 network.

To create a channel having symmetric length loops between each selectivity filter and its outer transmembrane helix, we transplanted Pro150-Gly155 from PD1 onto PD2, denoted "Loop2$_{Sym-6}$" (**figure 1.6 B**). Loop2$_{Sym-6}$ showed blunted responses to temperature (**figure 1.7 D&G**) and pressure (Lolicato et al. 2020). Consistent with the deletion of key ML335-binding SF2-M4 loop residues, Loop2$_{Sym-6}$ was unresponsive to ML335 (**figure 1.7 E&H**) but remained partially sensitive to BL-1249 (**figure 1.7 F&I**), an activator that affects the channel from a site under the selectivity filter (Pope et al. 2018, Schewe et al. 2019). Measurement of rectification in inside-out patches, a parameter that is a direct measure of C-type gate activation (Schewe et

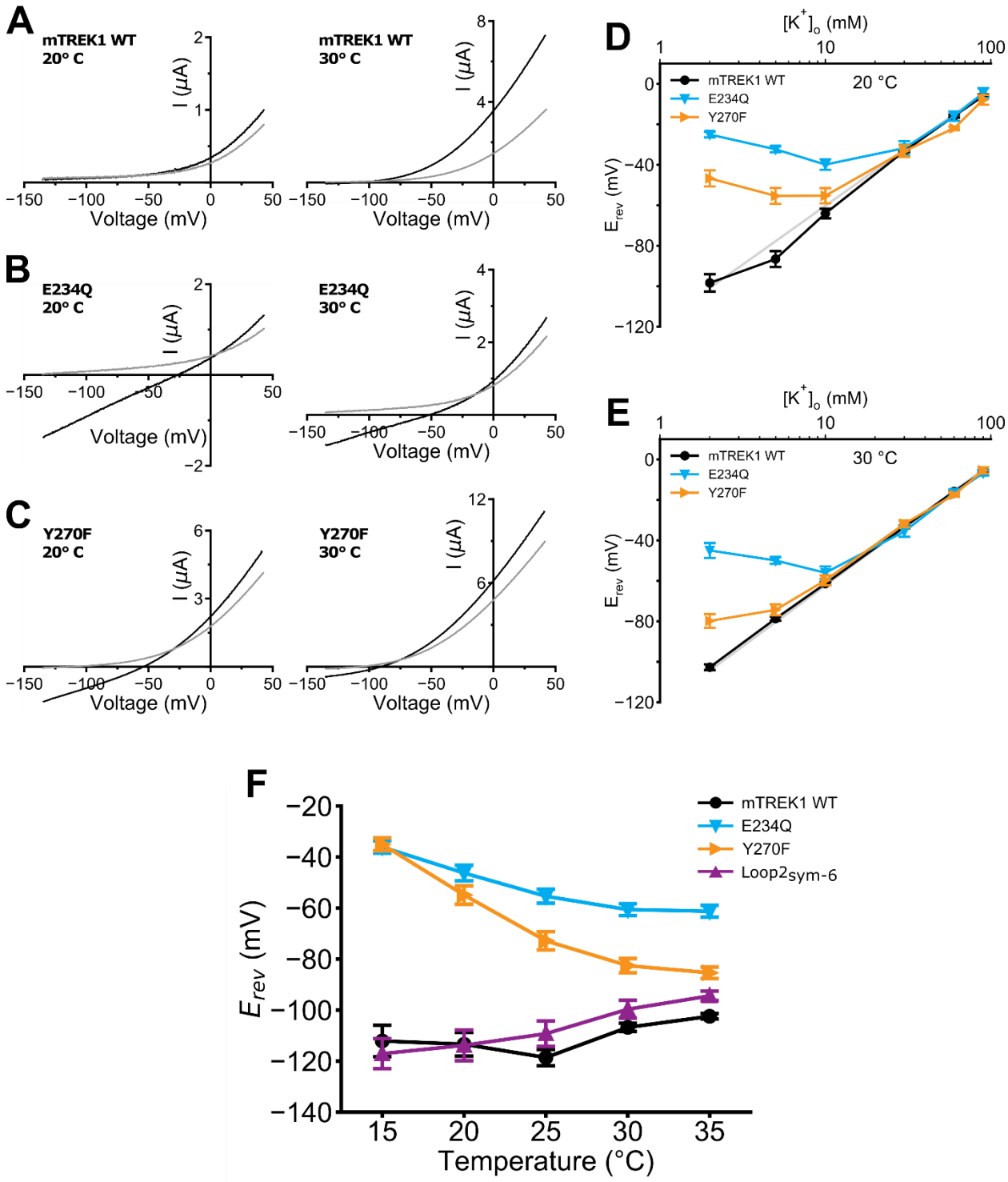


**Figure 1.8: Activation alters TREK-1 mutant ion selectivity**

**Figure 1.8 Legend. (A-C)**, Exemplar two-electrode voltage clamp (TEVC) recordings of TREK-1 **(A)**, TREK-1 E234Q **(B)**, and TREK-1 Y270F **(C)** at 20° C (left) and 30° C (right) in solutions of 96 mM Na+/2 mM $K^+$ (black) or 96 mM N-methyl-D-glucamine/ 2 mM $K^+$ (grey). **(D) & (E)**, Potassium selectivity recorded in Xenopus oocytes in $K^+/Na^+$ solutions (98.0 mM total) at $pH_o$ = 7.4 at d, 20° C and e, 30° C (n=6). Data are background subtracted using uninjected oocytes. Grey line represents Nernst equation $E_{rev} = {RT}/{zF} \times \log([K^+]_o/[K^+]_i)$, where *R* and *F* have their usual thermodynamic meanings, *z* is equal to 1, and *T* = 20° C or 30° C, assuming $[K^+]_i$ = 108.6 mM (Guizouarn et al. 2001). **(F)** $E_{rev}$ as a function of temperature for the indicated channels from TEVC experiments in Xenopus oocytes. For panels **(D)-(F)**, data represent mean ± s.e.m.

al. 2016, Lolicato et al. 2017), demonstrated that unlike gain-of-function mutants, $Loop2_{Sym\text{-}6}$ does not have a constitutively activated C-type gate that would render it insensitive to gating commands (Lolicato et al. 2020). Hence, the blunted responses caused by shortening the SF2-M4 loop to the canonical length indicate that the unusual length of the SF2-M4 loop is central to C-type gate control.

Disruption of the Glu234 hydrogen bond network by E234Q and Y270F mutations resulted in channels having severely blunted responses to temperature (**figure 1.7 D&G**), pressure (Lolicato et al. 2020), ML335 (**figure 1.7 E&H**), and BL-1249 (**figure 1.7 F&I**). Unlike $Loop2_{Sym\text{-}6}$, both mutations compromised ion selectivity as evidenced by an altered reversal potential (**figures 1.7 D-F and 1.8**). This baseline selectivity defect was partially corrected by temperature or pressure activation (**figures 1.7 D and 1.8**; and Lolicato et al. 2020). Together, with prior mutational studies suggesting a role for the SF2-M4 loop in external pH gating (Sandoz et al. 2009), these data strongly support the key role that the SF2-M4 loop has in $K_{2P}$ channel gating and underline the importance of SF2-M4 stabilization by the network centered on Glu234.

*The M3 glutamate network has a conserved role in C-type gate control*

The key elements of the Glu network are highly conserved among $K_{2P}$s (**figure 1.6 D & F**). To test its general importance, we disrupted this network in TASK-1 ($K_{2P}$3.1), a $K_{2P}$ from a subfamily distant from TREK-1 (Feliciangeli et al. 2015). Structural comparison shows that TASK-1 Glu182, Leu208, and Tyr220 form a network similar to the TREK-1 Glu234-Gly260-Tyr270 network (**figure 1.9 A**). Notably, this network is structurally conserved although TASK-1 has one of the longest SF4-M4 loops (14 residues) (**figure 1.6 F**) and has a large sidechain, leucine, at the position that contributes the backbone amide (**figure 1.9 A**). Disruption of this network in TASK-1 had substantial functional consequences. TASK-1 E182Q failed to produce functional channels (**figure 1.9 C**), whereas TASK-1 Y220F yielded channels that were more readily closed by low pH (**figure 1.9 D&E**). This result phenocopies disruption of interactions on the opposite side of the SF2-M4 loop in P1-M4 interface by the TASK-1 I88G mutant (Bagriantsev et al. 2012) and indicates that the Y220F mutation destabilized the SF2-M4 loop and C-type gate. Together, our data demonstrate that the Glu234 network and its stabilization of the SF2-M4 loop is a central element of C-type gate control. Because of its conservation and functional importance in diverse $K_{2P}$s, we term this network as the M3 glutamate network.

## DISCUSSION

*Mechanistic implications for $K_{2P}$ channel function*

Despite the central role of the selectivity filter C-type gate in $K_{2P}$ channel function (Feliciangeli et al. 2015, Bagriantsev et al. 2011, Bagriantsev et al. 2012, Piechotta et al. 2011), observation of conformational changes that would provide a framework for understanding the

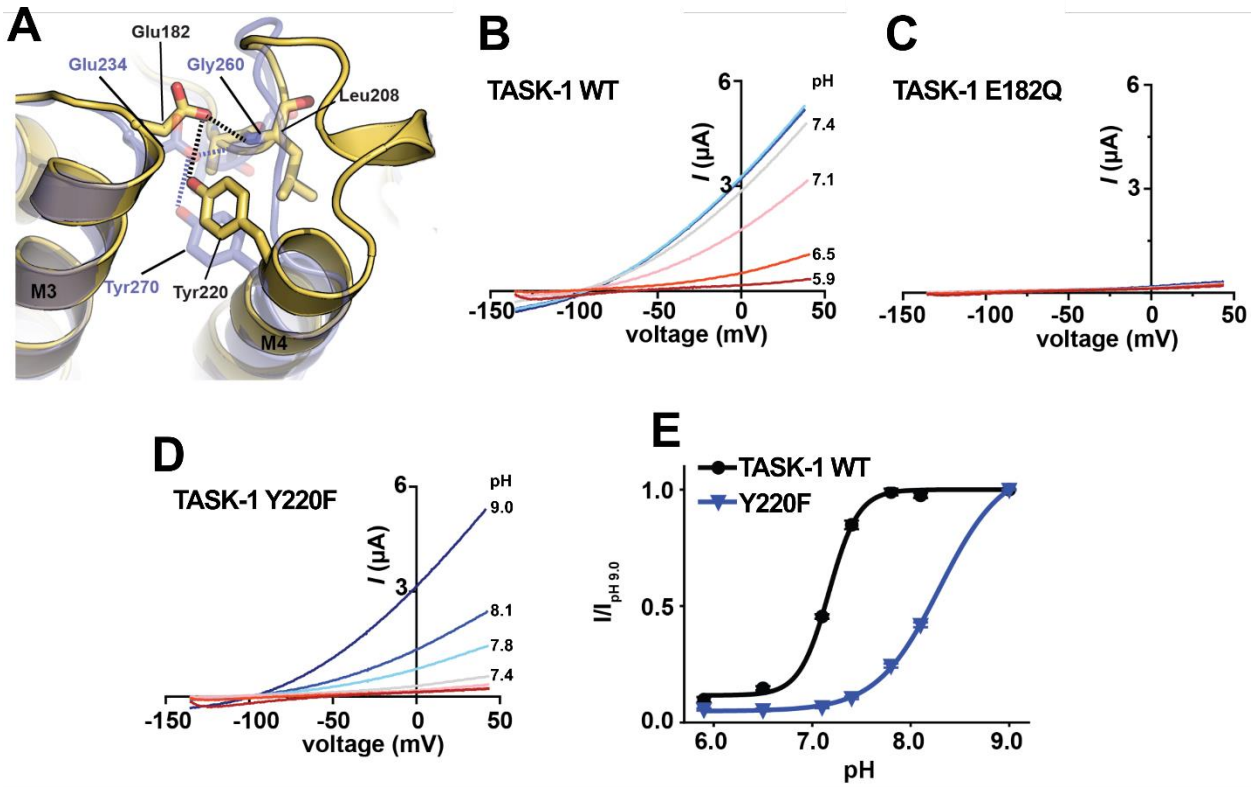


**Figure 1.9: M3 network destabilization facilitates TASK-1 C-type gate closure**

**Figure 1.9 Legend. (A)** Comparison of the SF2-M4 loop and surrounding elements TASK-1 (PDBID: 6RV2) (Rödström et al. 2020) (yellow) and TREK-1 (PBD:6CQ8) (Lolicato et al. 2017) (transparent purple). Key network residues are shown as sticks and are labeled. Dashed lines show hydrogen bonds. **(B)-(D)** Exemplar two-electrode voltage clamp (TEVC) recordings of **(B)**, TASK-1; **(C)**, TASK-1 E182Q; and **(D)**, TASK-1 Y220F at $pH_{ext}$: 9.0 (dark blue), 8.1 (blue), 7.8 (light blue), 7.4 (grey), 7.1 (pink), 6.5 (red), 5.9 (maroon). **(E)**, pH activation curves for TASK-1 and TASK1 Y220F (blue), showing the fraction of the current at 0 mV at each pH relative to the current at pH 9.0 (n≥10). Data in **(E)** represent the mean ± s.e.m. (n≥10).

principles of $K_{2P}$ C-type gating has eluded previous structural studies (Lolicato et al. 2017, Dong et al. 2015, Brohawn et al. 2012, Brohawn et al. 2013, Brohawn et al. 2014, Lolicato et al. 2014, Miller & Long 2012, Rödström et al. 2020). Our data establish that control of the $K_{2P}$ C-type gate involves unprecedented, asymmetric, potassium-dependent, order-disorder transitions in the selectivity filter and surrounding loops (**figures 1.4 and 1.10**). The selectivity filter conformational changes associated with $K_{2P}$ C-type gating comprise two classes of

rearrangements that eliminate the S1 and S2 ion binding sites. One pinches the SF1 extracellular side and exposes the Asn147 sidechains to the extracellular solution (**figure 1.10 A**), a position that modulates C-type inactivation in homotetrameric potassium channels (Pless et al. 2013, Lees-Miller et al. 2000) and that undergoes similar changes in human Ether-à-go-go-Related potassium channel (hERG) simulations (Miranda et al. 2020). Hence, this class of C-type gating mechanism is shared with other potassium channels. The second unwinds SF2 and the SF2-M4 loop, dilates the selectivity filter along the SF2 axis (**figure 1.10 B**), depends on the structure of the uniquely long $K_{2P}$ SF2-M4 loop, and is unlike any of the prior structural changes associated with C-type gating. SF1 pinching and SF2 dilation are not mutually exclusive and are likely to be interdependent given the role of the SF ions in stabilizing the filter. Such asymmetric changes could contribute to the bimodal distribution of closed state dwell times reported for TREK-1 (Bockenhauer et al. 2001) and the closely-related TREK-2 ($K_{2P}$10.1) (Clausen et al. 2017). Further, as $K_{2P}$ heterodimer formation yields channels having two unique SF1-M2 and SF2-M4 loops, this structural diversification together with the two non-mutually exclusive inactivation modes likely provides a mechanism for the emergence of heterodimer properties that differ from either homodimer parent (Lengyel et al. 2016, Levitz et al. 2016, Blin et al. 2016, Royal et al. 2019, Blin et al. 2014, Renigunta et al. 2014, Berg et al. 2004, Mathie et al. 2021). The structural rearrangements in the pore and surrounding regions, loss of S1 and S2 ions, and the demonstration that destabilization of the SF2-M4 loop structure compromises ion selectivity are reminiscent of studies of the nonselective bacterial channel NaK, which has only the S3 and S4 sites and can be converted into a potassium-selective channel by forming the S1 and S2 ion binding sites (Derebe et al. 2011). Further, the loss of ion selectivity associated with $K_{2P}$ C-type

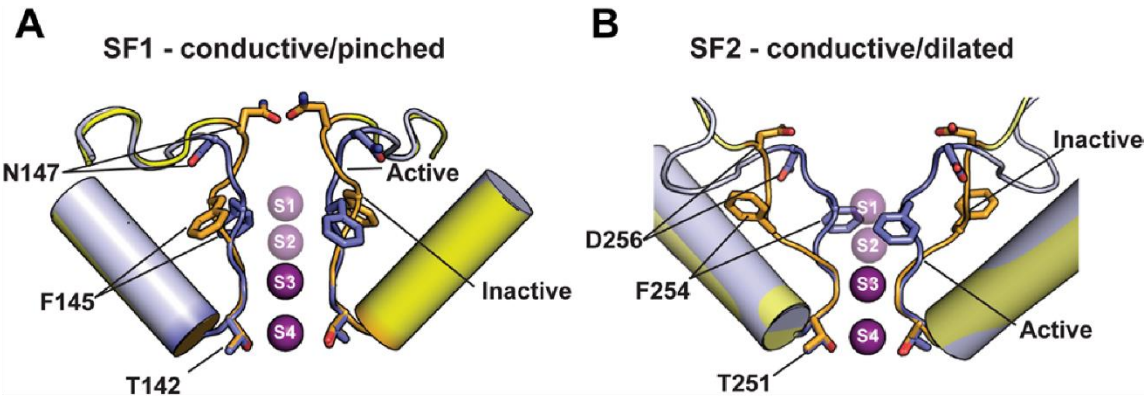


**Figure 1.10: Structural changes associated with C-type gating**

**Figure 1.10 Legend. (A)** SF1 and **(B)** SF2 selectivity filter changes between the active (slate) [**(A)** and **(B)** conductive] and inactive (yellow orange) [**(A)** pinched and **(B)** dilated] conformations based on the 1 mM [$K^+$] and 0 mM [$K^+$]:ML335 structures, respectively. Selectivity filters for 1 mM [$K^+$] and 0 mM [$K^+$]:ML335 show select residues. Potassium ions are magenta spheres.

gating (Bagriantsev et al. 2011, Cohen et al. 2008, Yuill et al. 2007) and the strong link between $K_{2P}$ gating and external potassium concentration (Bagriantsev et al. 2011, Bagriantsev et al. 2012, Piechotta et al. 2001, Cohen et al. 2008) are in good accord with the structural and functional changes we observe. Although C-type gating is an important mode of channel regulation in many potassium channel classes (Schewe et al. 2019), structural insights into its mechanistic basis are limited to studies of a small number of homotetrameric potassium channel types (Cordero-Morales et al. 2006, Zhou & MacKinnon 2003, Zhou et al. 2001, Cuello et al. 2017, Cuello et al. 2010, Wang & MacKinnon 2017, Pau et al. 2017, Matthies et al. 2018) and lack consensus (Hoshi & Armstrong 2013), even for the best studied example, KcsA (Liu et al. 2015, Li et al. 2017, Li et al. 2018, Devaraneni et al. 2013). Nevertheless, our studies identify a unifying feature shared between $K_{2P}$ C-type gating and homotetrameric potassium channel C-type gating—the importance of the conserved glutamate at the extracellular end of the pore module outer helix (**figures 1.7 A and 1.6 C&D**). This site on the $K_{2P}$ PD1 M1 helix affects C-type

gating through interactions with the SF1-M2 loop (Cohen et al. 2008, Zilberberg et al. 2001) similar to other channels which have a canonical six residue loop between the selectivity filter and pore module outer helix (**figure 1.6 B**) (Larsson & Elinder 2000, Ortega-Sáenz et al. 2000, van der Cruijsen et al. 2013). The equivalent PD2 glutamate on M3 of TREK-1, Glu234, forms a conserved network together with a M4 tyrosine, Tyr270, the M3 glutamate network that supports the uniquely long SF2-M4 loop found throughout the $K_{2P}$ family (**figure 1.6 F**). Disruption of the M3 glutamate network blunts responses to diverse stimuli in distantly related $K_{2P}$s (**figures 1.7, 1.8, and 1.9**) and establishes that, together with its role in external pH responses (Sandoz et al. 2009), the SF2-M4 loop is a hub that integrates chemical and physical gating cues sensed in other parts of the channel (**figure 1.7 D-I**) and relayed to the filter via M4 (Bagriantsev et al. 2011, Bagriantsev et al. 2012). The M3 glutamate network is conserved in every functional $K_{2P}$ except TRESK ($K_{2P}$18.1), the only $K_{2P}$ having a short SF2-M4 loop (**figure 1.6 F**). This conservation, together with the report that a pulmonary hypertension mutation at the conserved M3 glutamate in TASK-1 ($K_{2P}$3.1), E182K, disrupts function (Ma et al. 2013) underscores the importance of the M3 glutamate network and SF2-M4 loop in gating throughout the $K_{2P}$ family.

Our studies establish that $K_{2P}$ channel C-type gating entails filter pinching (SF1) and pore dilation (SF2), highlight the dynamic nature of C-type inactivated states (Jekhmane et al. 2019), and indicate that the innate heterodimeric nature of the $K_{2P}$ filter architecture enables two general C-type gating mechanisms, pinching and dilation (Hoshi & Armstrong 2013), which have been viewed as mutually exclusive, to operate in one channel. The substantial differences in the degree of conformational changes between SF1 and SF2 appear to depend on the loop length

connecting these elements to the outer transmembrane helix of their respective pore domains. Binding of small molecules, such as ML335, to the $K_{2P}$ modulator pocket enables conduction by stabilizing the SF2-M4 loop and selectivity filter and increasing channel open probability, whereas disruption of the integrity of the SF2-M4 loop blunts transduction of gating cues that originate from the intracellular C-terminal tail (Bagriantsev et al. 2012, Bagriantsev et al. 2011, Maingret et al. 2000a, Patel et al. 1998, Chemin et al. 2004, Honoré et al. 2002, Kim et al. 2001) and pass through M4 to the C-type gate. These findings corroborate the ideas that the $K_{2P}$ selectivity filter and its supporting architecture are dynamic under basal conditions (Lolicato et al. 2017), that ion permeation requires limiting filter mobility through ligand binding to the $K_{2P}$ modulator pocket or by conformational changes transmitted through the M4 helix (Lolicato et al. 2017), that permeant ions organize and stabilize the $K_{2P}$ conductive state (Schewe et al. 2016, Schewe et al. 2019), and that the inactive state involves an ion-depleted filter (Schewe et al. 2016). Further, our observation that the filter can adopt nonconductive conformations although the M4 transmembrane helix is in the “up” position underscores previous studies indicating that M4 conformation is not the sole determinant of $K_{2P}$ activation (McClenaghan et al. 2016). The key role for the SF2-M4 loop in transducing gating cues sensed by intracellular channel components to the $K_{2P}$ selectivity filter gate such as temperature and pressure, as well as external pH responses (Sandoz et al. 2009), demonstrates its pivotal function in $K_{2P}$ gating. These properties, together with the ability of ML335 to increase open probability by stabilizing this loop, explain why the P1-M4 interface, which is framed on one side by the SF2-M4 loop, is central to $K_{2P}$ gating and why small molecules bound to this interface activate the channel (Lolicato et al. 2017). These findings emphasize the potential for targeting this unique $K_{2P}$ loop

for selective small molecule or biologic modulators directed at $K_{2P}$-dependent processes such as anesthetic responses (Heurteaux et al. 2004, Lazarenko et al. 2010), pain (Alloui et al. 2006, Devilliers et al. 2013, Vivier et al. 2017), arrhythmia (Decher et al. 2017), ischemia (Wu et al. 2013), and migraine (Royal et al. 2019).

## METHODS

*Molecular dynamics system setup*

Initial TREK-1 simulations in the absence of ML335 were initiated from PDBID:5VK5. Later simulations were based on PDBID:6CQ6 (Lolicato et al. 2017), which is indistinguishable from PDBID:5VK5 except for a minor difference in the C-terminal portion of M4. Simulations in complex with ML335 were constructed from PDBID:6W8C (Lolicato et al. 2020). In both cases, models consisted of residues 35 to 321, a disulfide bond was formed between C93 in one subunit with C93 in the other, missing loops were built with RosettaRemodel (Huang et al. 2011), and N and C termini were capped with methylamide and acetyl groups, respectively. All residues were assigned their standard protonation states at pH 7. Structures were embedded in pure 1-palmitoyl-2-oleoyl-glycero-3-phosphocholine (POPC) or POPC + 4% inner leaflet mole fraction 1-stearoyl-2- arachidonoyl-glycero-3-phosphatidylinositol 4,5-bisphosphate (18:0-20:4) $PIP_2$ bilayers using CHARMM-GUI (Jo et al. 2007) and solvated in 180 mM [$K^+$] with neutralizing $Cl^-$ (excepting low [$K^+$] simulations, which contained only 4 mM [$K^+$]). Two structural water molecules were added per subunit in the cavity between SF2 and pore helix 2 on the basis of water molecules identified in TRAAK ($K_{2P}$4.1) PDBID:4I9W (Brohawn et al. 2013). For simulations containing $PIP_2$, an additional $PIP_2$ lipid per channel subunit was placed in the lipid binding site

adjacent to the M4 helix, as observed in the ML335:1 mM [$K^+$] structure (PDBID:6W8C). Extensive preliminary $K_{2P}$ simulations were initiated from a range of filter ion configurations in the S1 to S4 sites including alternating $K^+$ and water with waters at either S1/S3 or S2/S4, all $K^+$, or all $K^+$ with empty sites at S2 or S3. In all cases, the configuration with ions in S1/S2/S4, and an empty S3 was frequently visited during the conduction cycle. Thus, all high [$K^+$] simulations presented here were equilibrated with this configuration. Low [$K^+$] simulations were initiated with a single ion in the selectivity filter placed at the S2, S3, or S4 site. The force fields used for protein, lipids, water, and ML335 were CHARMM36m (Huang et al. 2017), CHARMM36 (Klauda et al. 2010), TIP3P (Jorgensen et al. 1983), and CGenFF 3.0.1 (Vanommeslaeghe et al. 2010, Vanommeslaeghe & MacKerell 2012, Vanommeslaeghe et al. 2012) respectively. Standard CHARMM parameters were used for ions (Beglov & Roux 1994).

*Molecular dynamics simulation details*

Production data were collected on two platforms: Anton2 (Shaw et al. 2014) at the Pittsburgh Supercomputing Center and local graphical processing unit (GPU) resources using GROMACS 2018 (Abraham et al. 2015) (see **table 1.2** for a full list). All systems were energy minimized for 8000 steps with 5 kcal/mol·Å$^2$ harmonic restraints on all protein heavy atoms, followed by a multistep equilibration in which protein restraints were gradually reduced over 10 to 12 ns. Next, for systems simulated under a membrane potential, we performed a 10-mV voltage jump every 5 ns until reaching 40 mV using the constant electric field protocol where $E_{applied} = V/Lz$ (Gumbart et al. 2012). On average $L_z$ = 121 Å in our systems, and the final applied electric field was 0.0076 kcal/mol·Å·e. Note that systems destined for Anton2 were equilibrated with NAMD 2.13 (Phillips et al. 2005). Production run details varied by hardware. Simulations

on Anton2 used a 2.5-fs time step, a Martyna-Tobias-Klein barostat (Martyna et al. 1994) with semi-isotropic pressure control at 1 atm, and a Nose-Hoover thermostat (Nosé 1983, Hoover 1985) with a temperature of 303.15 K. In addition, non-bonded interactions were cut off at 10 Å, long-range electrostatic interactions were calculated using the Gaussian split Ewald method (Shan et al. 2005), and hydrogens were constrained with the SHAKE algorithm (Ryckaert et al. 1977). Meanwhile, GROMACS 2018 runs used either a 2- or 2.5-fs time step, a Parrinello-Rahman barostat (Parrinello & Rahman 1981, Nosé & Klein 1983) with semi-isotropic pressure control at 1 atm, and a Nose-Hoover thermostat set to 310 K. Non-bonded interactions were cut off at 12 Å with force-switching between 10 and 12 Å, long-range electrostatics were calculated with particle mesh Ewald (Darden et al. 1993), and hydrogens were constrained with the LINCS algorithm (Hess et al. 1997). For low [$K^+$] simulations, solution ions were excluded from the selectivity filter using a flat bottom restraint on Anton2 or harmonic positional restraints in GROMACS 2018.

*Simulation data analysis*

Ions were tracked within a 22-Å-long cylindrical volume centered on the selectivity filter, and a permeation event was recorded when an ion originating below (above) the midplane of the filter (defined by the plane separating S2 to S3 sites) exited the top (bottom) of the cylinder. The time of the permeation event was recorded as the last time the ion crossed the midplane before exit from the cylinder. PCA was carried out on the backbone dihedral angles of selectivity filter residues (142 to 146 in SF1 and 251 to 255 in SF2) as described in Altis et al. 2007, and each strand was treated independently. Formation of hydrogen bonds to carboxylate or carbonyl oxygens was determined on the basis of the H to O distance (>2.5 Å for OH donors,

>2.75 Å for NH donors) and C═O H angle >110°. For all analyses, conformations were sampled from the trajectories every 480 to 500 ps. All analysis code was built on top of the MDAnalysis Python package (Michaud-Agrawal et al. 2011).

*Two-electrode voltage-clamp electrophysiology*

Two-electrode voltage-clamp recordings were performed on defolliculated stage V to VI Xenopus laevis oocytes 18 to 48 hours after microinjection with 1 to 40 ng of mRNA. Oocytes were impaled with borosilicate recording microelectrodes (0.3- to 3.0-MΩ resistance) backfilled with 3 M KCl. Except where otherwise indicated, recording solution was 96 mM NaCl, 2 mM KCl, 1.8 mM $CaCl_2$, and 1.0 mM $MgCl_2$, buffered with 5 mM Hepes at pH 7.4 and was perfused by gravity. For $pH_o$ experiment solutions, the standard buffer was replaced with 10 mM tris (pH 9.0 and 8.1), 5 mM Hepes (pH 7.8 and 7.1), or 5 mM MES (pH 6.5 and 5.9).

Currents were evoked from a −80-mV holding potential followed by a 300-ms ramp from −150 to +50 mV. Data were acquired using a GeneClamp 500B amplifier (MDS Analytical Technologies) controlled by pCLAMP software (Molecular Devices) and digitized at 1 kHz using Digidata 1332A digitizer (MDS Analytical Technologies).

For temperature experiments, recording solutions were heated by an SC-20 in-line heater/cooler combined with an LCS-1 liquid cooling system operated by the CL-100 bipolar temperature controller (Warner Instruments). Temperature was monitored using a CL-100–controlled thermistor placed in the bath solution 1 mm upstream of the oocyte. For temperature experiments, perfusate was warmed from 15° to 35°C in 5°C increments, with recordings performed once temperature readings stabilized at the desired values. Temperature response data were fit with the equation:

$$A = A_{min} + (A_{max} - A_{min})/(1 + e^{T_{1/2} - T)/S})$$

where $A_{min}$ and $A_{max}$ are the minimum and maximum activation, respectively, $T_{1/2}$ is the temperature of half maximal activation, and $S$ is the slope factor (adapted from Bagriantsev et al. 2012). For $pH_o$ experiments, solutions were exchanged consecutively from 9.0 to 5.9 while maintaining the temperature at 22.5°C. pH response data were fit with the equation:

$$A = A_{min} + (A_{max} - A_{min})/(1 + ([H^+]_o/K_{1/2})^H)$$

where $A_{min}$ and $A_{max}$ are the minimum and maximum activation, respectively, $K_{1/2}$ is the half maximal inhibitory concentration of extracellular protons, and $H$ is the Hill slope.

Dose-response experiments were conducted at room temperature (22°C) and used standard recording solution at pH 7.4 supplemented with 0.2% dimethyl sulfoxide and the indicated concentration of ML335 (Lolicato et al. 2017). Dose-response data were fit with the equation:

$$A = A_{min} + (A_{max} - A_{min})/(1 + (EC_{50}/[ML335])^H)$$

where $A_{min}$ and $A_{max}$ are the minimum and maximum activation, respectively, $EC_{50}$ is the half maximal effective concentration, and $H$ is the Hill slope. Data analysis and curve fitting were performed using Clampfit and Python according to procedures adapted from Bagriantsev et al.

2012 & Lolicato et al 2017. X. laevis oocytes were harvested from female X. laevis according to UCSF Institutional Animal Care and Use Commitee (IACUC) Protocol AN178461.

**Table 1.1: $K_{2P}$ channel selectivity filters structure comparison.**

| Structure (M4 status) | PDBID | Ion concentration | RMSD Cα (Å) |
|---|---|---|---|
| TREK-1 (up) | 6CQ6 | 200 mM KCl | NA - reference |
| TREK-1:ML335 (up) | 6CQ8 | 200 mM KCl | 0.25 |
| TREK-1:ML402 (up) | 6CQ9 | 200 mM KCl | 0.33 |
| TREK-2 (up) | 4BW5 | 200 mM KCl | 0.30/0.31 |
| TREK-2 (down) | 4XDJ | 200 mM KCl | 0.33/0.33 |
| TREK-2:norfluoxetine (down) | 4XDK | 200 mM KCl | 0.32/0.27 |
| TRAAK (down) | 3UM7 | 150 mM KCl | 0.55 |
| TRAAK:Fab (down) | 4I9W | 150 mM KCl | 0.38 |
| TRAAK:Fab (up) | 4WFE | 150 mM KCl | 0.38 |
| TRAAK:Fab (down) | 4WFF | 150 mM KCl | 0.37 |
| TRAAK:Fab (up) | 4WFG | 150 mM $TlNO_3$ | 0.37 |
| TRAAK:Fab (up) | 4WFH | 150 mM $TlNO_3$ | 0.39 |
| TRAAK G124I (down) | 4RUE | 150 mM KCl | 0.36 |
| TRAAK W262S (down) | 4RUF | 150 mM KCl | 0.38 |
| TWIK-1 (down) | 3UKM | 150 mM KCl | 0.41/0.42 |
| TASK-1 (X-gate, down) | 6RV2 | 200 mM KCl | 0.33/0.34 |
| TASK-1:BAY1000493 (X-gate, down) | 6RV3 | 200 mM KCl | 0.33/0.34 |
| TASK-1:BAY2341237 (X-gate, down) | 6RV4 | 200 mM KCl | 0.34/0.35 |

**Table 1.2: List of molecular dynamics simulations.**

| Sim # | N atoms | MD engine | Temp (K) | PDBID | Bilayer | N $K^+$ ions | Initial SF $K^+$ configuration | Length (us) | N $K^+$ permeations | Potential (mV) |
|---|---|---|---|---|---|---|---|---|---|---|
| 1 | 205,060 | Anton2 | 303.15 | 6W8C | POPC + $PIP_2$ | 149 | S1/S2/S4 | 2.88 | 26 | +40 |
| 2 | 205,060 | Anton2 | 303.15 | 6W8C | POPC + $PIP_2$ | 149 | S1/S2/S4 | 2.88 | 23 | +40 |
| 3 | 205,060 | Anton2 | 303.15 | 6W8C | POPC + $PIP_2$ | 149 | S1/S2/S4 | 2.88 | 9 | +40 |
| 4 | 205,060 | Anton2 | 303.15 | 6W8C | POPC + $PIP_2$ | 149 | S1/S2/S4 | 3.84 | 30 | +40 |
| 5 | 205,060 | Anton2 | 303.15 | 6W8C | POPC + $PIP_2$ | 149 | S1/S2/S4 | 2.88 | 35 | +40 |
| 6 | 205,228 | Anton2 | 303.15 | 6W8C | POPC + $PIP_2$ | 149 | S1/S2/S4 | 3.84 | 26 | +40 |
| 7 | 205,228 | Anton2 | 303.15 | 6W8C | POPC + $PIP_2$ | 149 | S1/S2/S4 | 3.84 | 20 | +40 |
| 8 | 205,228 | Anton2 | 303.15 | 6W8C | POPC + $PIP_2$ | 149 | S1/S2/S4 | 2.88 | 2 | +40 |
| 9 | 205,228 | Anton2 | 303.15 | 6W8C | POPC + $PIP_2$ | 149 | S1/S2/S4 | 2.88 | 29 | +40 |
| 10 | 205,228 | Anton2 | 303.15 | 6W8C | POPC + $PIP_2$ | 149 | S1/S2/S4 | 2.88 | 53 | +40 |
| 11 | 205,159 | Anton2 | 303.15 | 5VK5 | POPC + $PIP_2$ | 149 | S1/S2/S4 | 4.80 | 3 | +40 |
| 12 | 205,159 | Anton2 | 303.15 | 5VK5 | POPC + $PIP_2$ | 149 | S1/S2/S4 | 4.80 | 36 | +40 |
| 13 | 205,175 | Anton2 | 303.15 | 6CQ6 | POPC + $PIP_2$ | 149 | S1/S2/S4 | 1.92 | 3 | +40 |
| 14 | 205,175 | Anton2 | 303.15 | 6CQ6 | POPC + $PIP_2$ | 149 | S1/S2/S4 | 1.92 | 2 | +40 |
| 15 | 205,175 | Anton2 | 303.15 | 6CQ6 | POPC + $PIP_2$ | 149 | S1/S2/S4 | 1.92 | 2 | +40 |
| 16 | 205,175 | Anton2 | 303.15 | 6CQ6 | POPC + $PIP_2$ | 149 | S1/S2/S4 | 1.92 | -1 | +40 |
| 17 | 205,175 | Anton2 | 303.15 | 6CQ6 | POPC + $PIP_2$ | 149 | S1/S2/S4 | 2.88 | 19 | +40 |
| 18 | 205,325 | Anton2 | 303.15 | 6CQ6 | POPC + $PIP_2$ | 149 | S1/S2/S4 | 3.84 | 20 | +40 |
| 19 | 205,325 | Anton2 | 303.15 | 6CQ6 | POPC + $PIP_2$ | 149 | S1/S2/S4 | 2.88 | 18 | +40 |
| 20 | 205,325 | Anton2 | 303.15 | 6CQ6 | POPC + $PIP_2$ | 149 | S1/S2/S4 | 3.84 | 6 | +40 |
| 21 | 205,325 | Anton2 | 303.15 | 6CQ6 | POPC + $PIP_2$ | 149 | S1/S2/S4 | 2.88 | 2 | +40 |
| 22 | 205,325 | Anton2 | 303.15 | 6CQ6 | POPC + $PIP_2$ | 149 | S1/S2/S4 | 3.84 | 34 | +40 |
| 23 | 204,174 | Anton2 | 303.15 | 6CQ6 | POPC | 4 | S3 | 3.60 | - | 0 |
| 24 | 204,441 | Anton2 | 303.15 | 6CQ6 | POPC | 4 | S4 | 3.60 | - | 0 |
| 25 | 204,006 | Anton2 | 303.15 | 6CQ6 | POPC | 4 | S2 | 3.60 | - | 0 |
| 26 | 204,174 | Gromacs | 310 | 6CQ6 | POPC | 4 | S3 | 1.40 | - | 0 |
| 27 | 204,168 | Gromacs | 310 | 6CQ6 | POPC | 4 | S4 | 2.40 | - | 0 |
| 28 | 204,168 | Gromacs | 310 | 6CQ6 | POPC | 4 | S4 | 2.00 | - | 0 |
| 29 | 204,006 | Gromacs | 310 | 6CQ6 | POPC | 4 | S2 | 2.00 | - | 0 |
| 30 | 204,006 | Gromacs | 310 | 6CQ6 | POPC | 4 | S4 | 2.00 | - | 0 |

# CHAPTER 2: $PIP_2$ regulates TREK-1 via multiple binding sites and long-range electrostatics

## INTRODUCTION

It has long been recognized that the functions of ion channels and other membrane proteins are influenced by the composition and properties of their host membranes (Hilgemann et al. 2001, Suh et al. 2005, Suh et al. 2008). With the availability of increasing numbers of membrane protein structures in recent years it has become clear that lipids often bind to specific sites on protein surfaces where they directly impact structure and function (Thompson et al. 2020, Duncan et al. 2020). Of particular interest are phosphoinositide (PI) lipids which are known to be key regulators of a variety of ion channels and other membrane proteins despite their relatively low abundance in membranes. Targets for PI regulation include types of $K_{ir}$, $K_v$, BK, and TRP channels as well as members of the TMEM16 family (Logothetis et al. 2007, Taylor and Sanders 2017, Qin 2007, Prescott and Julius 2003, Vaithianathan et al. 2008; Ye et al. 2018). Binding sites for highly charged PIs, like phosphoinositol-4,5-bisphosphate ($PI(4,5)P_2$ or $PIP_2$), have been characterized on a number of channels, where they seem to exert their action by coordinating basic amino acid residues with lipid phosphate groups to bias the conformational state of the protein (Hansen et al. 2011, Niu et al. 2020, Sun & MacKinnon 2020).

The first published structures of the $K_{2P}$ channel TREK-1 ($K_{2P}2.1$) revealed the presence of a potential inner-leaflet lipid binding site in a groove formed by the M1, M4, and M2' helices (Lolicato et al. 2017). Subsequent crystal structures revealed a copurified $PIP_2$ lipid at this site, termed the modulatory lipid site, positioned such that its headgroup was in contact with the

transmembrane M4 helix as it extends parallel to the membrane away from the core of the channel (this region has also been termed the proximal C-terminus or 'pCt') (**figure 2.1A**) (Lolicato et al. 2020, Natale et al. 2021). The lipid's fatty acid tails make extensive, mostly hydrophobic contacts with M1 and M2, while basic residues on the M4/pCt, particularly Arg297, Lys301, and Lys304, are well positioned to coordinate lipid phosphate groups (**figure 2.1B**). Notably, this $PIP_2$ binding site is largely conserved among the TREK subfamily of mechanosensitive $K_{2P}$s – consisting of TREK-1, TREK-2 ($K_{2P}$10.1), and TRAAK ($K_{2P}$4.1) – especially regarding the positions of charged residues (**figure 2.1C** – binding site residues are underlined). Sensitivity to $PIP_2$ has been reported throughout the $K_{2P}$ family, including in all members of the TREK subfamily, which can be activated by $PIP_2$, as well as in some members of the TALK, TASK, and THIK subfamilies (Chemin et al. 2005, Lopes et al. 2005, Niemeyer et al. 2017, Riel et al. 2022). It was initially reported that TREK-1 is strongly activated by $PIP_2$ and several other anionic and neutral phospholipids, including phosphatidylinositol (PI), phosphatidylethanolamine (PE), phosphatidylserine (PS), and finally phosphatidic acid (PA), which had the strongest activating effect of all lipids tested (Chemin et al. 2005). Activation was shown to depend on this same M4/pCt region as was later seen contacting lipid in the crystal structures. The pCt carries a set of 5 basic residues (Arg297, Lys301, Lys302, Lys304, Arg311), a Glu residue responsible for sensing intracellular pH (Glu306) (Honoré et al. 2002), and a protein kinase C phosphorylation site (Ser300) (Murbartián et al. 2005). However, subsequent work on TREK-1 and TREK-2 has reported evidence of inhibition by $PIP_2$, or a mixed response, with activation at low [$PIP_2$] and inhibition at higher [$PIP_2$] (Chemin et al. 2007, Woo et al. 2016, Cabanos et al. 2017). Several studies have also suggested the presence of an additional $PIP_2$

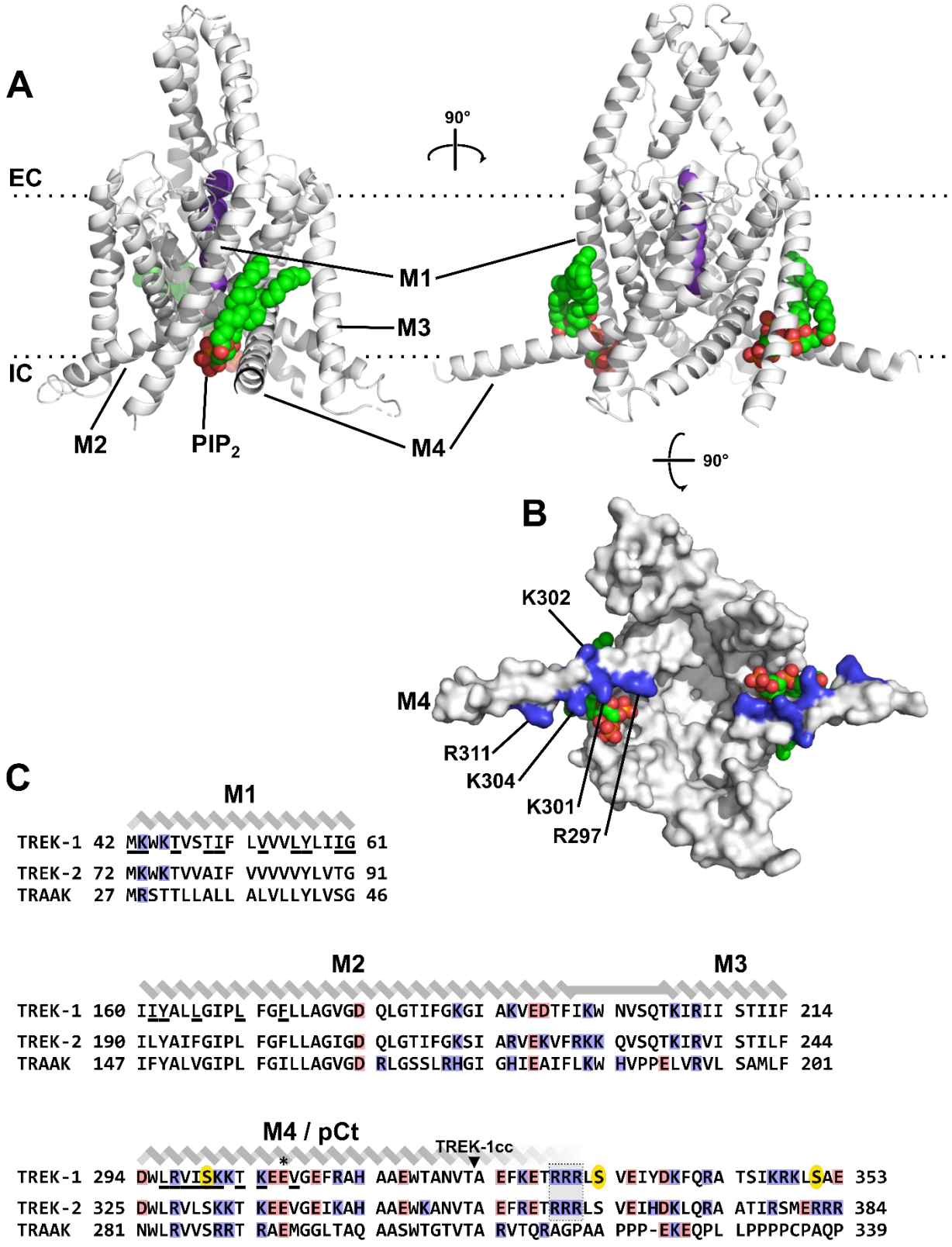


**Figure 2.1: Structural basis for $PIP_2$ binding to TREK-1**

**Figure 2.1 Legend. (A)** Two views from inside the membrane plane, showing $PIP_2$ (green, red, and orange spheres) bound into a groove in the TREK-1 (white ribbons) surface formed by the M1 and M4 helices. **(B)** The same structure rotated 90 degrees to show the intracellular face of TREK-1 (surface representation). Protein residues Arg297, Lys301, Lys302, Lys304, and Arg311 are colored blue. The structure shown in **(A) & (B)** is PDBID 6W8C (Lolicato et al. 2020). **(C)** Alignment of selected portions of the human TREK-1, TREK-2, and TRAAK sequences, covering those parts of M1, M2, M3, and M4 in contact with the inner leaflet of the plasma membrane. Residue positions in direct Van der Waals contact with the $PIP_2$ lipid in TREK-1 crystal structure 6W8C are underlined. Basic residues are highlighted in blue; acidic residues in red. Experimentally validated TREK-1 phosphorylation sites at Ser300, Ser333, and Ser351 are indicated by yellow ovals (Koh et al. 2001, Murbartián et al. 2005). An "*" indicates the TREK-1 intracellular pH sensor E306 (Honoré et al. 2002). The site of the C-terminal truncation after Thr322 used in the TREK-1 crystal construct is indicated by a "▼". The GenBank IDs for sequences used in the alignment are TREK-1($K_{2P}$2.1): AAD47569.1, TREK-2($K_{2P}$10.1): AAL95705.1, and TRAAK($K_{2P}$4.1): AAF64062.1.

sensitive site on a more distal polybasic region of the TREK-1 C-terminus at Arg329 / Arg330 / Arg331 or the TREK-2 equivalent (Woo et al. 2019, Soussia et al. 2018) (**figure 2.1C** – boxed region). It is interesting to note that in the initial report on TREK-1 $PIP_2$ activation (Chemin et al. 2005) a triple mutant of the phosphate coordinating residues R297A / K301A / K304A (denoted '3+A' in that study) retained $PIP_2$ activation comparable to "wild-type" (WT) TREK-1, while a 5x Ala mutant R297A / K301A / K302A / K304A / R311A (denoted '5+A' in that study and 'M4-5A' here) essentially eliminated $PIP_2$ dependent activation, showing that $PIP_2$ regulation is not exclusively mediated by residues contacting $PIP_2$ in the crystal structure. In addition, the ability of mutations in the pCt to eliminate $PIP_2$ sensitivity also suggests that the more distal site is subordinate to the pCt site if it is at all involved in $PIP_2$ dependent regulation.

Several studies have now directly assessed the binding affinity of lipids to TREK channels. A solubilized channel binding competition assay was used to measure $PIP_2$ $K_d$s of 0.9 µM and 1.4 µM for TREK-1 and TRAAK, respectively (Cabanos et al. 2017). Native mass

spectrometry experiments on TRAAK gave a similar result for $PIP_2$ and PA with $K_d$s ~1 μM, and notably also showed that a TRAAK construct truncated just after the pCt domain can bind up to 4x $PIP_2$ per dimer, or 4-6 copies of many other anionic lipid types (Schrecke et al. 2021). This finding demonstrates that there must be more than 1 $PIP_2$ binding site per subunit in TRAAK, and because of the overall structural similarity among TREK subfamily channels this may also be the case for TREK-1 and TREK-2.

In the present work, I aim to test this idea using long timescale coarse-grained (CG) molecular dynamics (MD) simulations. I identify 3 potential binding sites for $PIP_2$ and other anionic lipids on the surface of TREK-1 where it contacts the membrane, one of which corresponds to the crystallographic site, and calculate the relative binding free energy of these sites. In addition, using microsecond timescale all-atom computational electrophysiology MD simulations, I show that bound $PIP_2$ lipids or the M4-5A mutation can increase the $K^+$ flow rate through the selectivity filter. These conditions also modify the $K^+$ occupancy of the TREK-1 selectivity filter and on longer timescales would be expected to impact function by stabilizing the filter's active conformation and increasing channel open probability.

## RESULTS

*TREK-1 contains multiple anionic lipid binding sites per subunit*

To explore the idea that there might be additional, as-yet uncharacterized lipid binding sites on TREK-1, I turned to molecular dynamics (MD) simulations using the coarse-grained (CG) Martini force-field (Marrink et al. 2007), to access the long timescales required to observe lipid association and dissociation on the surface of the channel. The Martini coarse graining scheme

treats groups of up to 4 heavy atoms as single coarse-grained particles with average properties derived from the parent atoms – such as polar or nonpolar, or H-bond donor or acceptor. This approach allows for CG simulations to run 50-100x faster than equivalently sized all-atom simulations. While this model is necessarily lower resolution than an all-atom model it has been shown to accurately describe the interactions of many types of biomolecules and is frequently used to semi-quantitatively examine protein-lipid interactions (Corey et al. 2019). In Martini force field simulations, lipid binding and unbinding timescales range from hundreds of nanoseconds to tens of microseconds (Duncan et al. 2020), so all individual trajectories here were run for at least 100 microseconds to try to observe many binding events at any potential sites (see **Table 2.1** for a list of CG simulations).

I ran an initial set of simulations containing TREK-1 in a simple bilayer composed of a pure phosphatidylcholine (PC) outer leaflet, and a 9:1 PC:$PIP_2$ inner leaflet (**figure 2.2A**). From these trajectories 'lipid contact maps' were generated for each of the two lipid species by calculating the time-averaged number of lipids contacting each protein residue within a 6.5 Å cutoff (**figure 2.2 B-E**). To reduce noise most of the hydrophobic lipid tail particles were excluded from the calculation (keeping only the first apolar particle of each tail, typically named 'C1A' and 'C1B' in Martini) so that maps primarily represent contacts made by headgroups and glycerol backbone particles. These maps reveal several apparent hotspots for $PIP_2$ interaction on the inner leaflet contacting surface of TREK-1, including residues in and around the crystallographic site, but also numerous contacts on M2 and M3 far from that site, with Lys198 and Lys205 standing out (**figure 2.2D**). In many of these regions $PIP_2$ is substantially enriched

relative to its abundance in the inner leaflet (10%) (**figure 2.2F**) indicating that TREK-1 has a higher affinity for $PIP_2$ than for neutral PC.

To examine how $PIP_2$–TREK-1 interactions might change when in competition with other anionic and neutral lipids I ran additional simulations with a more complex bilayer containing other major plasma membrane components sphingomyelin (SM), phosphatidylethanolamine (PE), phosphatidylserine (PS), and cholesterol (chol). Here I used an upper leaflet containing a 7:7:6 mixture of PC:SM:chol and a lower leaflet containing a 5:5:3:1:6 mixture of PC:PE:PS:$PIP_2$:chol, for an overall lower leaflet $PIP_2$ concentration of 5% (**figure 2.3A**). Lipid contact maps showed that $PIP_2$ contacts clearly dominate over all other lipid types at the same hotspots identified in the 2-component bilayer system despite the more complex milieu and the presence of anionic PS (**figure 2.2D and figure 2.3B**). I also wondered how phosphatidic acid (PA) would bind to TREK-1 and whether there was any overlap in $PIP_2$ and PA binding sites. PA is a short-lived signaling lipid with a much smaller headgroup than $PIP_2$ and has been shown to bind directly to both TREK-1 and TRAAK (Comoglio et al. 2014, Cabanos et al. 2017, Schrecke et al. 2021) and is a potent activator of TREK-1 (Chemin et al. 2005). Therefore, I ran a third set of simulations, similar to the second set except that $PIP_2$ in the inner leaflet was replaced by PA (**figure 2.3C**). The PA contact pattern on TREK-1 was roughly similar to that of $PIP_2$ with hotspots in the crystallographic site and on the M2 and M3 helices (**figure 2.3D**). However, most protein residues made fewer contacts on average with PA than with $PIP_2$, likely due the much smaller size of the PA headgroup and its reduced charge. In addition, PS was able to make slightly more contact with these same sites in the PA simulations relative to those with

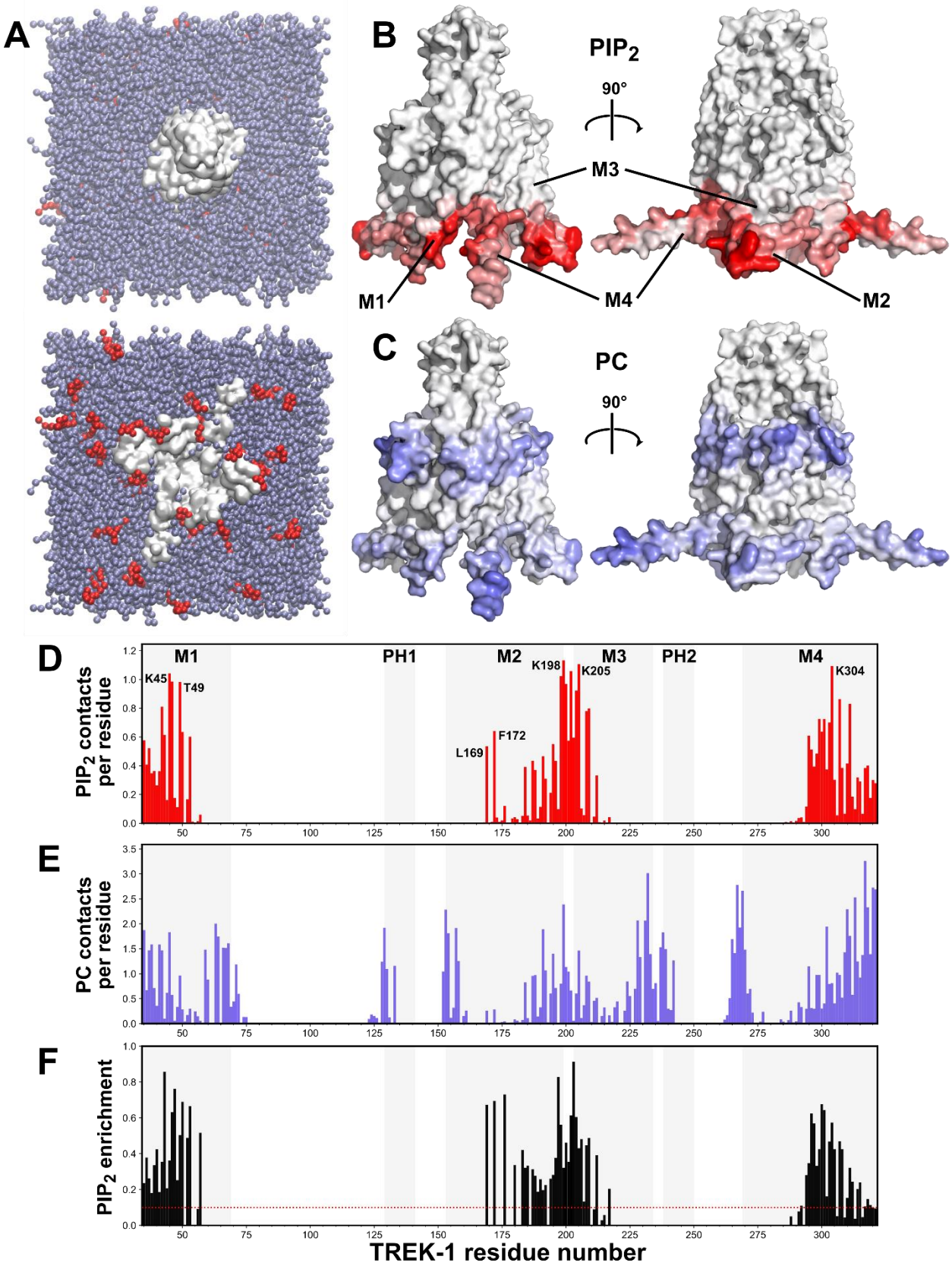


**Figure 2.2: CG simulations show $PIP_2$ enrichment on the TREK-1 surface**

**Figure 2.2 Legend. (A)** Extracellular (top) and intracellular (bottom) view of a simulation system of TREK-1 (white surface) in a simple bilayer containing only PC (light blue) and 10% inner leaflet $PIP_2$ (red). **(B)** Contact map for $PIP_2$ mapped onto the surface of TREK-1. **(C)** Contact map for PC. In **(B) & (C)** higher color intensity indicates a higher average number of contacts with the lipid in question. **(D) & (E)** Alternate representation of the contact maps shown in **(B) & (C)**. The height of a bar is the expected number of lipids of a species contacting that protein residue calculated as an average over all simulation time. **(F)** Enrichment of $PIP_2$ at each protein residue, calculated as the $PIP_2$ contact value divided by the sum of all ($PIP_2$ + PC) contacts. Positions where the sum of all contacts was less than 0.1 (representing areas that are only occasionally contacted by *any* lipid) were excluded from this calculation. The red dotted line indicates an enrichment value of 0.1, which is the expected value for a lipid at a concentration of 10% with no binding advantage over PC.

$PIP_2$, while contacts with neutral lipids remained constant, suggesting that all 3 types of anionic lipids are competing for the same set of sites (**figure 2.3 B&D**).

While it was clear from the lipid contact maps that $PIP_2$ and PA are enriched at the surface of TREK-1, this initial analysis did not uniquely identify all the potential binding sites, a description of which would be useful for interpreting lipidomics and functional experiments. To this end, I developed a method to assign protein residues to binding site clusters using the framework of a Markov state model (MSM) (see Methods section for details). This approach defines clusters as groups of protein residues which can collectively maintain long-lasting contacts with individual lipids, with the assumption that the most relevant binding sites are those groups which sustain the longest-lived interactions. I applied this analysis to the simple membrane (PC/$PIP_2$) dataset, which allowed me to identify 3 distinct $PIP_2$ binding sites per TREK-1 subunit (6 sites per dimer) with average bound state lifetimes of greater than 1 microsecond (**figure 2.4 A&B**). For the purposes of analyzing lifetimes, the equivalent sites on each subunit were considered together. The site with the longest lipid dwell times of up to ~80 microseconds ("site 1") corresponds to the crystallographic site, with a bound $PIP_2$ making

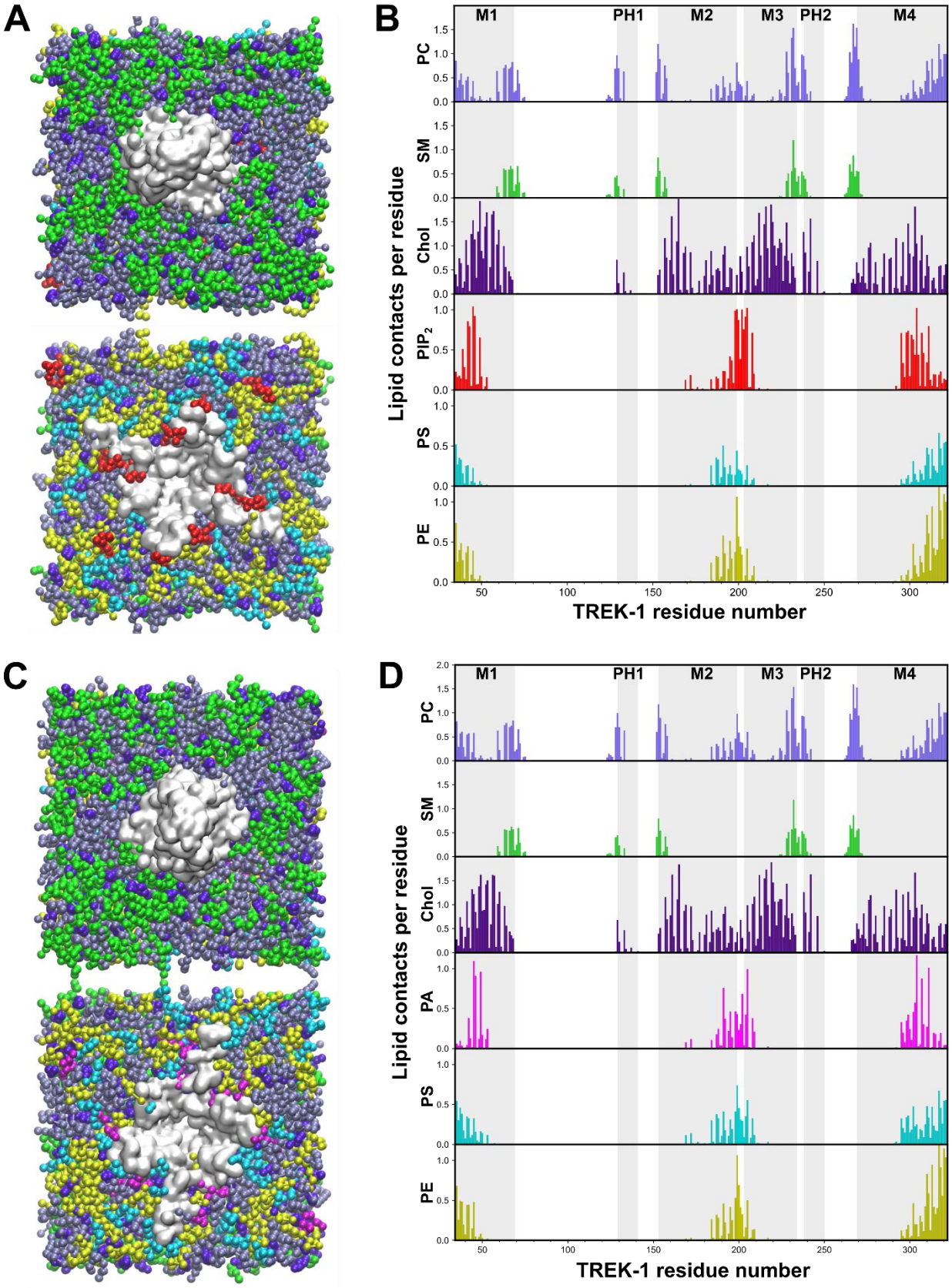


**Figure 2.3: $PIP_2$ and PA dominate TREK-1 contacts in complex lipid mixtures**

**Figure 2.3 Legend**. **(A)** Extracellular (top) and intracellular (bottom) view of a TREK-1 simulation with an upper leaflet composed of 7:7:6 PC:SM:cholesterol and a lower leaflet composed of 5:5:3:1:6 PC:PE:PS:$PIP_2$:cholesterol. **(B)** Contact maps for each lipid species for the set of simulations illustrated by **(A)**, as in **figure 2.2**. **(C)** Extracellular (top) and intracellular (bottom) view of a TREK-1 simulation with an upper leaflet composed of 7:7:6 PC:SM:cholesterol and a lower leaflet composed of 5:5:3:1:6 PC:PE:PS:PA:cholesterol. **(D)** Lipid contact maps for the set of simulations illustrated by **(C)**. In all panels PC (phosphatidylcholine) is light blue, SM (sphingomyelin) is green, cholesterol is purple, $PIP_2$ is red, PA (phosphatidic acid) is magenta, PS (phosphatidylserine) is cyan, and PE (phosphatidylethanolamine) is yellow.

extensive contacts with the M4 helix – including Lys301 and Lys304 in the functionally important 'proximal C-terminus' (pCt) region – as well as the M1 helix and the M2 helix of the opposite subunit. The next site ("site 2") hosts binding events lasting up to ~20 microseconds and is located on the opposite side of M4 from site 1, in a groove between M4 and M3. A lipid at this site can also contact the 'proximal C-terminus' region of M4, including residue Lys302, which is inaccessible from site 1. It also makes extensive contacts with the N-terminal end of M3, centered on Lys205. Finally, a third site ("site 3") was identified composed of residues at the C-terminal end of the M2 helix centered on Lys198 and Trp199, with bound $PIP_2$ lifetimes up to ~10 microseconds. This site is different than the first two in that it is not found at a groove in the protein surface but is instead mostly exposed to the bulk membrane and contains only a single basic residue (Lys198). All three sites on each subunit were occupied by $PIP_2$ greater than 95% of the time in both the simple bilayer (**figure 2.2A**) and the more complex mixture (**figure 2.3A**).

To make a semi-quantitative determination of the relative affinities of each of these sites for $PIP_2$, I next performed umbrella sampling simulations to calculate the potential of mean force (PMF) for $PIP_2$ binding to each of the sites using the weighted histogram analysis method (WHAM) (Kumar et al. 1992). These simulations were conducted in the context of an

otherwise pure PC membrane where each site is occupied by PC when $PIP_2$ is absent, so that the calculated binding free energies represent the ΔΔG of replacing PC with $PIP_2$. Sites 1, 2, and 3 have free energy minima of -8.1, -5.6, and -5.6 kcal/mol at distances of 21.3, 22.1, and 37.5 Å from the central axis of the channel, respectively (**figure 2.4 C**). The trend in binding energy roughly matches that of bound lipid lifetimes in the unbiased simulations, with site 1 having the most negative free energy and the longest bound state lifetimes. Sites 2 and 3 have the same binding energy, while the bound state lifetimes at site 2 are modestly longer than at site 3. The energy differences between site 1 and sites 2 site 3 of ~2.5 kcal/mol implies a roughly 60-fold difference in their affinities for $PIP_2$, suggesting that sites 2 & 3 are likely to be unoccupied at $PIP_2$ concentrations that would saturate site 1 (**figure 2.4 D&E**).

*$PIP_2$ binding increases conduction rates and influences $K^+$ distribution in the selectivity filter*

The presence of multiple $PIP_2$ binding sites is intriguing because it presents a possible explanation for the observation that $PIP_2$ can act as both an activator and inhibitor of TREK-1. One hypothesis is that $PIP_2$ binding at a high affinity site promotes channel opening, while binding at a lower affinity site reduces or blocks it. This would give rise to a biphasic activation response, with activation at low [$PIP_2$] and inhibition as [$PIP_2$] increases, as has been observed in both TREK-1 and TREK-2 (Chemin et al. 2007, Woo et al. 2016). Having determined the locations of several distinct $PIP_2$ binding sites on TREK-1, I next set out to explore how $PIP_2$ at these sites influences the structure and function of the channel. For this I turned to atomistic MD simulations of TREK-1 in complex with $PIP_2$ at locations identified via the CG-MD simulations, which were prepared using “wild-type” (WT) TREK-1 with either no $PIP_2$, $PIP_2$ in site 1 on both subunits (2 $PIP_2$ molecules), in site 2 on both subunits (2 $PIP_2$ molecules), or in site 1

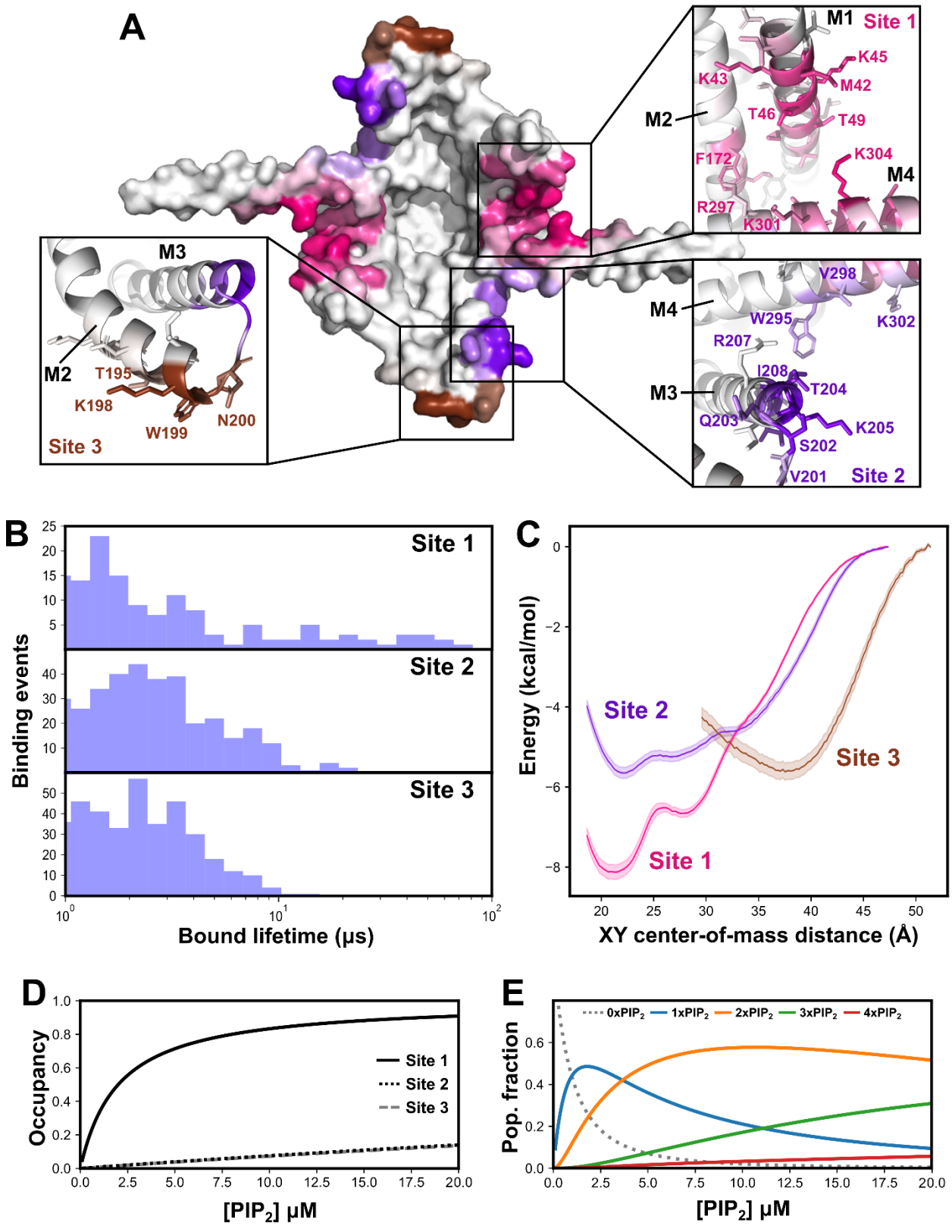


**Figure 2.4: TREK-1 contains 3 long-dwell-time $PIP_2$ binding sites**

**Figure 2.4 Legend. (A)** View of the intracellular face of TREK-1 highlighting the 3 identified binding sites; site 1 in pink, site 2 in purple, and site 3 in brown. The color intensity of each protein residue is proportional to its likelihood of being contact by a lipid bound at the site. Inset panels show details of key residues for each site. **(B)** Distributions of bound state lifetimes for $PIP_2$ binding events at each site calculated from simulations of TREK-1 in a PC + 10% inner leaflet $PIP_2$ bilayer. **(C)** PMFs for binding of $PIP_2$ into each of the 3 sites along 1-D linear reaction coordinates, colors as in **(A)**. **(D)** Occupancy of each site as a function of $PIP_2$ concentration for a simple binding model assuming no cooperativity between sites. Site 1 was assumed to have $K_{d1}$ = 2 µM based on native mass spectrometry measurements of the related channel TRAAK (Schrecke et al. 2020), and $K_d$s for sites 2 and 3 were estimated using the difference in binding free energy relative to site 1 calculated from the profiles shown in **(C)** (giving $K_{d2}$ = 120 µM and $K_{d3}$ = 130 µM). **(E)** Relative population fractions of different TREK-1:$PIP_2$ complexes from the binding model in **(D)**.

and 2 on both subunits (4 $PIP_2$ molecules) (**figure 2.5A**). In addition, I simulated the mutant R297A/K301A/K302A/K304A/R311A ("M4-5A") which neutralizes key basic residues in the M4/pCt domain that contacts sites 1 and 2 and has been shown to render TREK-1 insensitive to direct $PIP_2$ addition in functional experiments (Chemin et al. 2005). These M4-5A simulations were run without $PIP_2$. All simulations had 150 mM $K^+$ and were subject to a +200 mV membrane potential to drive ion currents through the channel. In simulations with $PIP_2$ the lipids were not restrained in their starting sites. Despite this, only 2 unbinding events were observed in over 85 microseconds of sampling, and only from site 2 while site 1 was already occupied by $PIP_2$, reinforcing the findings from the CG-MD simulations that sites 1 possesses the highest $PIP_2$ binding affinity of all identified sites. Lipid-protein contacts in site 1 were very similar to those observed in the CG simulations (**figure 2.5 B&D**), while $PIP_2$ at site 2 maintained the same overall contact pattern as in CG simulations but was able to burrow deeper into the groove between M3 and M4, enhancing its contacts with basic residues Arg207 and Arg297 as well as the M4/pCt (**figure 2.5 C&E**, compare to **figure 2.4A**).

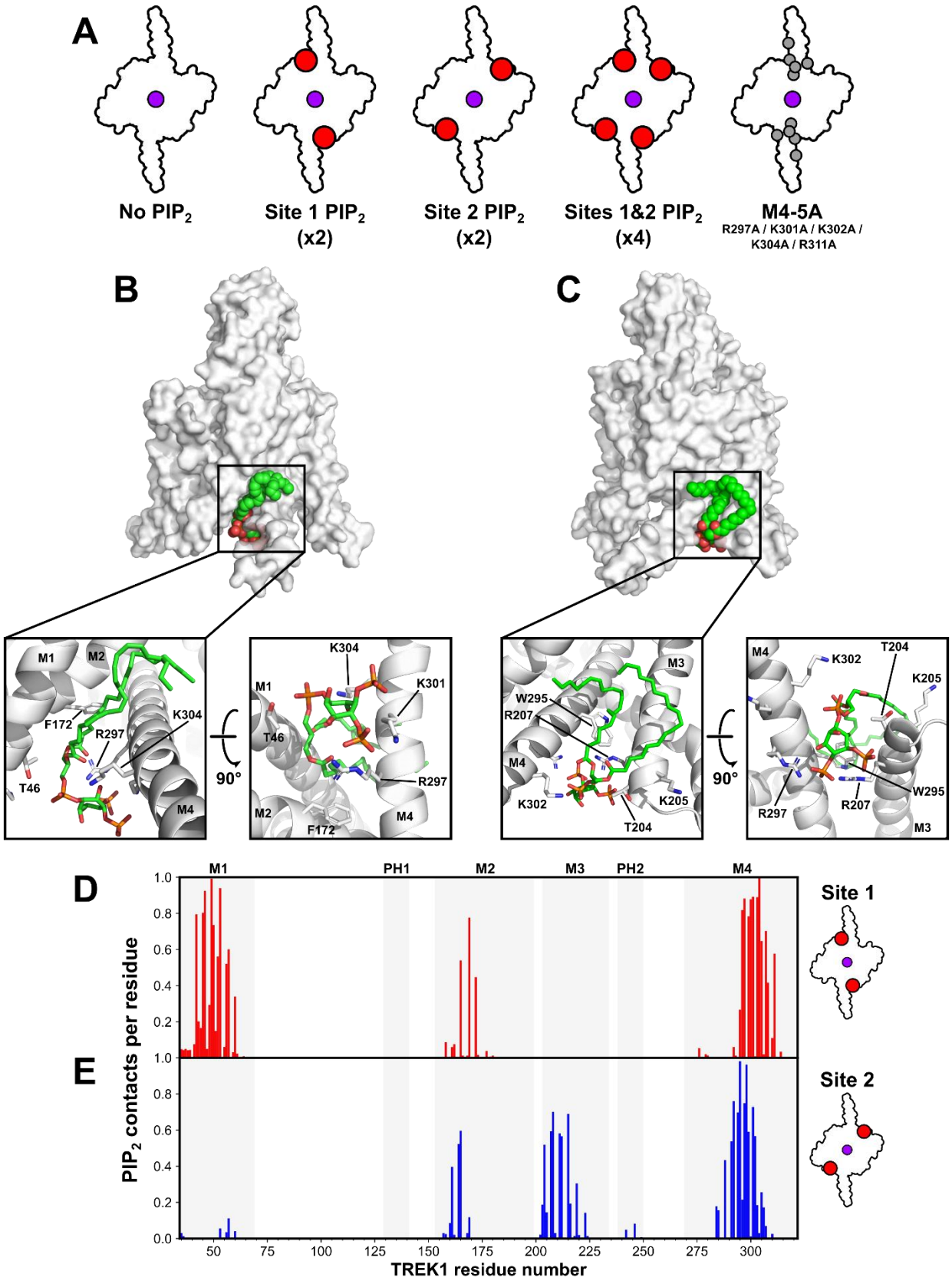


**Figure 2.5: Atomistic simulations confirm $PIP_2$ binding sites**

**Figure 2.5 Legend. (A)** Schematic illustration of the 5 different sets of atomistic simulations. The black outline is the silhouette of the cytoplasmic face of TREK-1; red circles represent approximate initial placement of $PIP_2$ molecules backmapped from CG simulations; grey circles represent locations of mutated residues; the purple circle is the location of the selectivity filter. **(B)** $PIP_2$ (green, red, & orange spheres/sticks) at site 1 at the end of a 4 μs trajectory; lower panels show closeup views and key protein residues. **(C)** $PIP_2$ in site 2 at the end of a 5 μs trajectory; same representations as in **(B)**. **(D)** Lipid contact maps for all atom simulations with $PIP_2$ in site 1 (upper panel) or site 2 (lower panel). Contact maps were calculated as for the CG simulations (**figures 2.2 and 2.3**) except using a 5.0 Å search radius and considering only protein and lipid heavy atoms.

Upon inspection of the trajectories, the rate of $K^+$ ion permeation through TREK-1 was noticeably different among the various simulation conditions (**figure 2.6 A-C**). I also observed that permeation rates were quite variable within a single trajectory, with bursts of many rapid permeation events interspersed with slower periods or even long pauses of up to 1 microsecond (**figure 2.6 A&B**). In addition, most simulations eventually saw TREK-1 enter an inactivated state via conformational changes in the selectivity filter, similar to what I had observed in a previous simulation study on TREK-1 (Lolicato et al. 2020). Despite this, I was able to observe more than 2000 total $K^+$ permeation events, with some individual trajectories maintaining the active state of the selectivity filter for up to 8-10 microseconds in the absence of any restraining potentials (see **table 2.3** for a full list of atomistic simulations).

In order to focus on the effects that $PIP_2$ or charge mutations have on the conductive state of the filter I restricted the analysis to the active portion of each trajectory, excluding any sampling after clear conformational changes in the selectivity filter. I then divided this data into 500 ns segments and calculated the current in each segment to obtain a distribution of current values for each simulation condition (**figure 2.6C**). The lowest overall permeation rate was observed for WT TREK-1 with no $PIP_2$, with a mean current (calculated on all conductive

trajectory segments) of 1.7 pA and a maximum current (in a single segment) of 4.5 pA. In contrast, simulations with $PIP_2$ in site 1 or the M4-5A mutant both had mean currents of 4.8 pA and maximum currents of 9.0 and 10.3 pA, respectively. The remaining two conditions with $PIP_2$ in site 2 or $PIP_2$ in both sites 1 and 2 had intermediate mean currents, which were still double that of the no-$PIP_2$ condition (3.4 pA mean current in both cases; 6.7 pA and 7.0 maximum, respectively).

The $PIP_2$ models used here in both atomistic and CG simulations carry a charge of −4, so the binding of 2 or 4 $PIP_2$ molecules to a TREK-1 dimer represents a net change of −8 or −16 elementary charges at the intracellular mouth of the channel. Similarly, the M4-5A mutation represents a net change of −10 elementary charges relative to WT TREK-1. I hypothesized that these charge shifts could alter the local electrostatic environment enough to increase the local $K^+$ concentration, leading to the observed increased permeation. Indeed, profiles of the $K^+$ ion density from the mouth of the pore (z = −20 Å) through the top of the selectivity filter (z = +14 Å) revealed marked differences between the 5 conditions (**figure 2.6D**). As before the analysis was restricted to only active, conducting segments of trajectories. Differences were especially pronounced in the mouth of the aqueous cavity 15-20 Å below the S4 filter site (z = 0) and were correlated with the magnitude of the charge difference relative to the no-$PIP_2$ condition. The two conditions with 2x $PIP_2$ (−8e) showed a roughly 2-fold increase in the probability of finding $K^+$ in this region, with M4-5A (−10e) it was increased by ~3-fold, and with 4x $PIP_2$ (−16e) it was increased by ~4-fold. Differences in ion occupancy were also seen just below the selectivity filter where there is an energy barrier to enter the filter as ions must shed their hydration shells (**figure 2.6D** – inset panels). Similarly correlated changes could be observed in the distribution

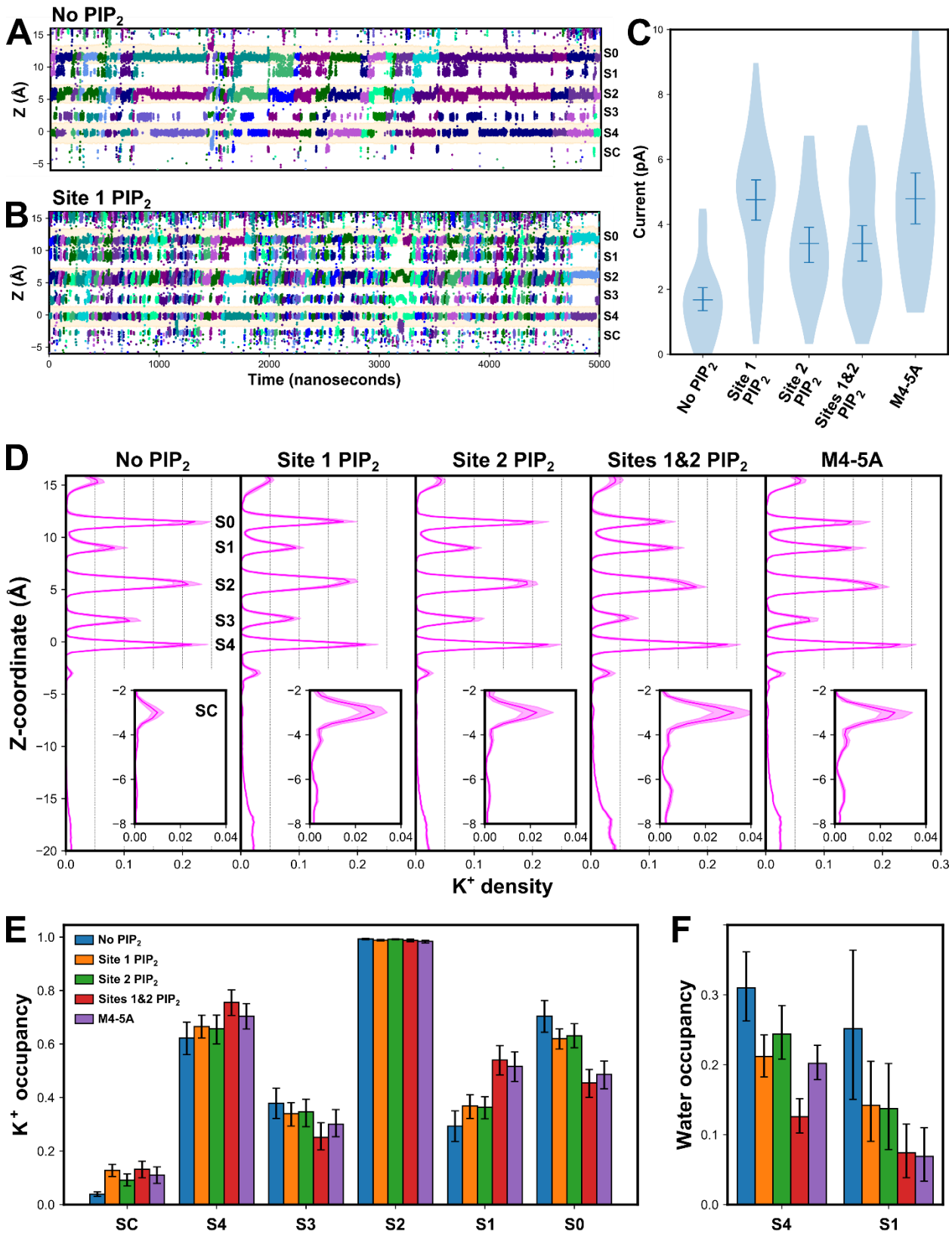


**Figure 2.6: $PIP_2$ and the M4-5A mutation alter the permeation rate and spatial distribution of $K^+$ ions around the SF**

**Figure 2.6 Legend**. **(A)** $K^+$ ion Z coordinates in the selectivity over the course of 5 μs of a "No $PIP_2$" trajectory. Individual ions are each marked with a different color (colors are recycled for different ions over time). Light yellow bands indicate the boundaries of the ion binding sites. **(B)** $K^+$ ion Z coordinates in the selectivity over the course of 5 μs of a "Site 1 $PIP_2$" trajectory, as in **(A)**. **(C)** Distribution of current values for all simulation conditions. **(D)** Profiles of the mean $K^+$ density in the SF and into the aqueous cavity for all simulation conditions. Peaks corresponding to ion binding sites are labeled in the leftmost panel. Inset panels show details of the region just below the SF, including the SC site. **(E)** Mean $K^+$ occupancy in each SF ion binding site for all simulation conditions. **(F)** Mean water occupancy in sites S4 and S1 for all simulation conditions. Error bars in **(C)-(F)** and error bands in **(D)** represent 95% bootstrap confidence intervals on the mean after the respective calculations were performed independently on each 500 ns trajectory segment, using only parts of trajectories prior to inactivation related conformational changes in the SF. The number of such segments for each simulation condition is "No $PIP_2$": 38, "Site 1 $PIP_2$": 42, "Site 2 $PIP_2$": 31, "Sites 1&2 $PIP_2$": 39, "M4-5A": 31.

of $K^+$ ions among the canonical ion binding sites of the selectivity filter (**figure 2.6E**). The 4x $PIP_2$ and M4-5A conditions resulted in a substantial increase in the $K^+$ occupancy of the S4 and S1 sites, with a corresponding decrease at S3 and S0, while the 2x $PIP_2$ conditions had an intermediate effect. Some of these differences can be attributed to decreased occupancy of sites S4 and S1 by water molecules, relative to the no-$PIP_2$ condition (**figure 2.6F**). Note that during the active, conductive trajectory segments included in the analysis in **figure 2.6** water molecules were never observed entering the central filter sites S2 and S3, although they frequently entered the filter after it had undergone conformational changes and ceased conducting.

I next sought to determine if the various simulation conditions had any effects on the overall structure of TREK-1. This was motivated by our observation that though the charge of the complex was well correlated with changes in the distribution of ions in and around the SF (**figure 2.6 D&E**), it was less well correlated with the rate of $K^+$ conduction (**figure 2.6C**). Specifically, while the condition with 4x bound $PIP_2$ (−16 e) had a higher conduction rate than

the no $PIP_2$ condition, it had a lower conduction rate than the site 1 $PIP_2$ condition (−8 e) or the M4-5A condition (−10 e). I was particularly interested in assessing any motions of the M4 helix, which has been observed in two different conformations in TREK-2 and TRAAK crystal structures (but not in TREK-1 as yet) (Brohawn et al. 2014, Dong et al. 2015). These 2 states, "M4-up" and "M4-down", have been suggested to play a role in allosteric modulation of the selectivity filter in the TREK family of channels, and simulation studies of TREK-2 have shown that it is possible to induce a conformational change from the down to up state via the application of membrane tension (Aryal et al. 2017, Clausen et al. 2017), albeit using a shorter construct that lacks part of the M4/pCt domain. I therefore measured conformational changes as in an earlier study (Aryal et al. 2017) by monitoring the distances between two key pairs of residues, Pro168-Gly293 and Arg207-Trp295. The first distance reports on the opening of a fenestration between M2 and M4 into a more M4-down state while the seconds tracks a "zippered" conformation of M3 and M4 that is also found in the M4-down state (**figure 2.7A**). The no-$PIP_2$ condition shows evidence for motions along both coordinates, with a small fraction of time spent in a more "zippered" state of M3-M4 association and in a more open M2-M4 fenestration state (**figure 2.7B**). No other condition showed evidence of M2-M4 fenestration openings. The only other condition where substantial M3-M4 "zippering" is present is with $PIP_2$ in site 2 only, which spends a significant fraction of time in this state (**figure 2.7D**), apparently as a result of the headgroup of $PIP_2$ bridging basic residues Lys205 and Arg207 on M3 and Lys302 and Arg297 on M4 to promote a closer association of these helices (**figure 2.5C**). The "zippered" conformation was entirely absent from simulations with $PIP_2$ in site 1, regardless of

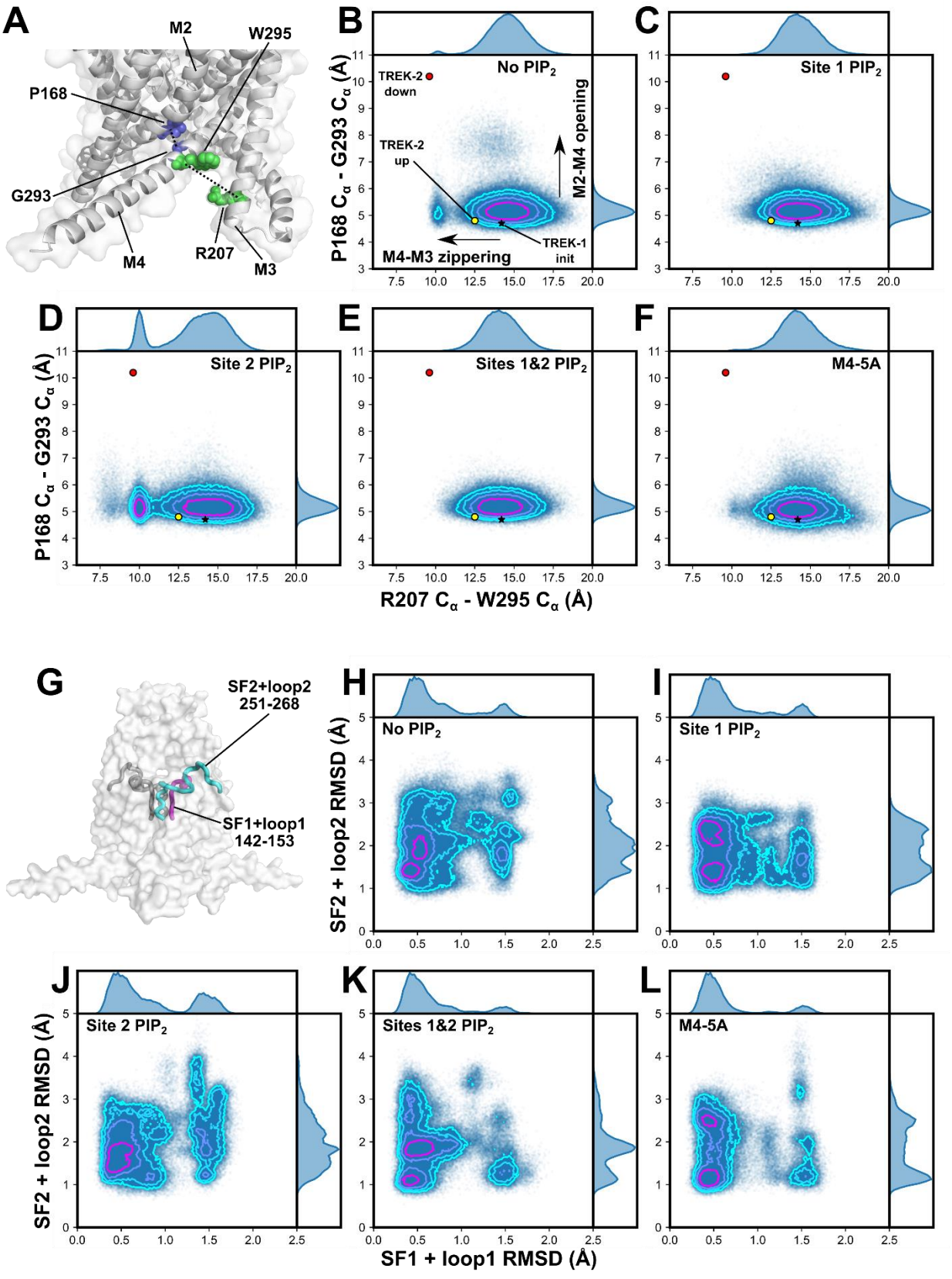


**Figure 2.7: Effects of $PIP_2$ binding on key TREK-1 structural elements**

**Figure 2.7 Legend. (A)** Structural illustration indicating the distances referenced in panels **(B)-(F)**. Arg207 and Trp295 (M3-M4 "zipper") are shown as green spheres; Pro168 and Gly293 (M2-M4 "fenestration") are shown as blue spheres. **(B)-(F)** Joint and marginal distributions of Arg207-Trp295 and Pro168-Gly293 $C_\alpha$-to-$C_\alpha$ distances for each simulation dataset. Stars indicate the initial distances in the TREK-1 structure 6CQ6 (Lolicato et al. 2017), red and yellow circles indicate the distances in the TREK-2 down state structure 4XDJ and up state structure 4BW5, respectively (Dong et al. 2015). **(G)** Structural illustration indicating the positions of SF1/loop1 (magenta; residues 142-153) and SF2/loop2 (cyan; residues 251-268) in the TREK-1 structure. **(H)-(L)** Joint and marginal distributions of $C_\alpha$ RMSD values for SF1 + loop1 and SF2 + loop2 for each simulation dataset. Each point represents the RMSD values for SF1 + loop1 and SF2 + loop2 in a single channel subunit, calculated independently. Contour levels in **(B)-(F)** and **(H)-(L)** indicate values of 50%, 25%, 12.5%, and 6.25% of the maximum height of the distribution.

the status of site 2 (**figure 2.7 C&E**), and only very rarely sampled in M4-5A simulations (**figure 2.7F**).

In my previous simulation study on TREK-1 my colleagues and I established that the post-selectivity filter loops, especially the SF2-M4 loop, are key points of control for channel inactivation (Chapter 1 & Lolicato et al. 2020). I therefore examined the distribution of root-mean-square-deviation (RMSD) values for the selectivity filter strands and their associated loops (SF1 + SF1-M2 loop ["loop1"] from residue 142-153 and SF2 + SF2-M4 loop ["loop2"] from residue 251-268) (**figure 2.7 G-L**). Note that while the no $PIP_2$ and $PIP_2$ in site 2 only conditions showed the largest deviations in SF2/loop2 RMSD from the starting structure (**figure 2.7 H&J**), each condition developed its own particular pattern. My prior work (Chapter 1 & Lolicato et al. 2020) showed that the inactivated state of the TREK-1 selectivity filter is highly dynamic, and each SF strand/loop combination can adopt many different possible conformations which makes it difficult to ascribe significance to any one inactivated conformation.

## DISCUSSION

TREK-1 and its close relatives in the $K_{2P}$ family are regulated by plasma membrane lipids, especially anionic lipids like $PIP_2$ and PA (Maingret et al. 2000b, Chemin et al. 2005, Chemin et al. 2007, Riel et al. 2022), which have been shown to bind directly to TREK-1 and TRAAK (Cabanos et al. 2017, Schrecke et al. 2021). Here, I have used Martini force-field CG-MD simulations to show that a single TREK-1 dimer can bind up to six $PIP_2$ lipids simultaneously and identify three distinct binding sites per subunit on the channel surface. One of these (site 1) corresponds to the site observed in recent crystal structures of TREK-1 in a groove formed by M1, M4, and M2 of the opposite subunit (**figure 2.1 A&B and figure 2.4A**) (Lolicato et al. 2020). From this position, $PIP_2$ makes contacts with key functional positions on the "proximal C-terminus" (pCt) of TREK-1 extending from the M4 helix (Chemin et al. 2005). Site 2 is found in the groove between M3 and M4 where it can contact the pCt from the other side of M4, and site 3 is located on the C-terminal end of the M2 helix (**figure 2.4A**). I also show that phosphatidic acid (PA), a potent activator of TREK-1, binds to the same sites as $PIP_2$ (**figure 2.3 B&D**). $PIP_2$ interactions with TREK-1 are longer lived at site 1 than at the other two sites, and free energy calculations show that binding is more favorable at site 1 by ~2.5 kcal/mol compared to sites 2 and 3 (**figure 2.4C**).

Native mass spectrometry and binding experiments have shown that $PIP_2$ binds to TRAAK and TREK-1 with an affinity of ~1-2 μM (Cabanos et al. 2017, Schrecke et al. 2021). Charged and hydrophobic residues in site 1 are well conserved among TREK family channels (**figure 2.1C**). Therefore, it seems likely that high affinity anionic lipid binding is a general feature of this M1/M4/M2' groove and that these studies have detected binding at this site in

both channels. In addition, mass spectrometry experiments on TRAAK show that up to 4-5 $PIP_2$ lipids can be detected bound to a single channel dimer (Schrecke et al. 2021), which suggests that this channel hosts sites analogous to the TREK-1 sites 2 and 3 described here. Site 2 residues are conserved between TREK-1 and TREK-2, while on the M3 side TRAAK shows some differences – notably a charge swap where central site 2 residues in TREK-1 Thr204 and Lys205 are replaced by Glu291 and Leu292 at the equivalent TRAAK positions. However, this is balanced by differences in the pCt domain, where TRAAK hosts fewer negatively charged residues than the equivalent TREK-1 and TREK-2 region (TREK-1 Glu305 and Glu309 are replaced by neutral residues Ala292 and Gly296 in TRAAK). In the case of site 3, TREK-2 carries +4 charges at the C-terminal end of M2 relative to TREK-1 (starting at TREK-1 residue 194 'DTFIKW' vs TREK-2 'KVFRKK' – see **figure 2.1C**), which may indicate that this site binds anionic lipids more strongly in TREK-2. Regardless, based on sequence features and structural similarity it seems likely that all three sites identified in TREK-1 are maintained among the three TREK subfamily members.

The detailed mechanism by which lipids exert their influence has remained unresolved, and there has not even been agreement on whether $PIP_2$ acts as an activator or inhibitor of TREK-1 and TREK-2 (Chemin et al. 2005, Chemin et al. 2007, Woo et al. 2016, Cabanos et al. 2017, Riel et al. 2022). Several studies have found evidence of channel activation of at low [$PIP_2$], followed by inhibition at higher [$PIP_2$] (Chemin et al. 2007, Woo et al. 2016), which could be explained by the presence of multiple binding sites with different affinities and opposite regulatory effects on the channel's selectivity filter gate. In this scenario, the highest affinity site, site 1, should be the activating site as it will be the first to be occupied at low [$PIP_2$]. The

inhibitory action of $PIP_2$ might then result from binding at site 2, site 3, or at an additional proposed site farther along the C-terminus at Arg329/Arg330/Arg331 (Woo et al. 2019, Soussia et al. 2018).

Our fully atomistic simulations revealed that $PIP_2$ binding to either site 1, site 2, or both sites promoted increased conduction rates, however the effect was strongest when $PIP_2$ was only in site 1. In addition, the M4-5A mutation, which was previously found to desensitize TREK-1 to $PIP_2$ addition (Chemin et al. 2005), promoted a conduction rate increase comparable to $PIP_2$ in site 1, indicating that neutralizing pCt basic residues can serve as a mutational substitute for lipid binding. Changes in the local concentration of $K^+$ around the channel mouth and in the aqueous cavity below the SF were well correlated with the overall charge of the pCt domain, counting the charge of bound lipids (**figure 2.6D**). Previous work has established that protein surface charges play a key role in determining the conductance and gating properties of a wide variety of ion channels by shaping the electrostatic potential around their ion permeation pathways (Imoto et al. 1988, MacKinnon et al. 1989, Cai and Jordan 1990, Li et al. 2000, Smith et al. 2001, Consiglio et al. 2003). In particular, the presence or absence of charged residues on the inner pore lining helix (equivalent to the $K_{2P}$ M4 helix) of tetrameric $K^+$ channels like BK and KcsA have been shown to modulate single channel conductance by modifying the local $[K^+]$ in the aqueous cavity below the SF (Brelidze et al. 2003, Nimigean et al. 2003, Carvacho et al. 2008). In a similar manner, a class of anionic small molecule $K^+$ channel activators that bind in the cavity just below the SF (such as BL1249 for TREK-1) increase single channel conductance through an electrostatic $K^+$ recruitment mechanism (Schewe et al. 2019). In the case of the TREK-1, in the absence of $PIP_2$ positively charged residues of the pCt act to reduce the local $[K^+]$.

$PIP_2$ binding into site 1 or 2, or mutations like M4-5A, neutralize these charges, recruit $K^+$ ions, and thereby raise the conduction rate.

It is well established that an increase in the permeant ion concentration stabilizes the C-type (SF) gate of potassium channels against inactivation by way of ion interactions with the selectivity filter (López-Barneo et al. 1993, Pardo et al. 1992, Bagriantsev et al. 2011, Bagriantsev et al. 2012, Lolicato et al. 2020). Therefore, the expectation is that the increase in local [$K^+$] resulting from $PIP_2$ binding or the M4-5A mutant should have a detectable effect on the selectivity filter. I do indeed observe such an effect as a shift in the distribution of $K^+$ ions among the binding sites of the filter between the different simulation conditions (**figure 2.6 D&E**). Most clearly, the simulations of $PIP_2$ in both sites 1 and 2 and of M4-5A show a substantial increase in the $K^+$ occupancy of ion site S1, which jumps to greater than 50% occupied from ~30% in the no $PIP_2$ condition. Smaller increases in S1 occupancy were observed for the other two conditions with $PIP_2$ in either site 1 or site 2. My previous work showed that TREK-1 C-type inactivation is the result of a conformational change in the SF that disrupts the ion binding sites, especially S1, and is associated with reduced or eliminated $K^+$ occupancy of this upper part of the filter (Chapter 1 & Lolicato et al. 2020). It follows that increasing the ion occupancy of S1 should stabilize the active state of the C-type gate and disfavor conformational changes in the SF. Altogether, my results show that $PIP_2$ binding modulates the electrostatic potential of TREK-1, increasing local [$K^+$] around the intracellular channel mouth, increasing the conduction rate, and redistributing ions in the filter to stabilize the active C-type gate.

This electrostatic activation mechanism provides for one potential explanation for how $PIP_2$ and other anionic lipids activate TREK-1, however our results do not clearly reveal how $PIP_2$

might act as an inhibitor. I find that in all conditions when $PIP_2$ is at either site 1, site 2, or both, it promotes an increase in the conduction rate and an increase in S1 $K^+$ occupancy, suggesting activation in all cases (**figure 2.6 C-E**). However, previous data suggests that factors other than just electrostatics may determine the degree of activation. Notably, phosphatidylethanolamine (PE), a zwitterionic lipid with a net zero charge, has also been shown to act as a TREK-1 activator, and lipids like PA (−1 or −2 charge) and phosphatidylserine (PS; −1 charge) have a larger activating effect than $PIP_2$ (−3 to −5 charge), despite carrying less charge per lipid (Chemin et al. 2005). I therefore also examined our data for any signs of structural transitions around the lipid binding sites with the hypothesis that there may be an allosteric component to lipid activation (or potentially inhibition).

All our simulations were initiated in the "M4-up" state, with M4 packed against M2 of the opposite subunit, while the intracellular ends of M4 and M3 are separated by a ~14 Å gap, as measured from residues Arg207 and Trp295. This remains the predominant configuration throughout most of our simulation time, and I never observe any full transitions to the "M4-down" state, as it appears in TREK-2 crystal structures (Dong et al. 2015). However, I do observe transient "zippering" of the M3-M4 interface in some conditions, characterized by close contacts between Arg207 and Trp295 sidechains (Aryal et al. 2017) (**figure 2.5C and figure 2.7 A-F**). In the no $PIP_2$ and M4-5A conditions this was observed rarely (~2% or ~1% of simulation frames, respectively), while in the site 2 $PIP_2$ condition it occurs for ~20% of the total simulation time and apparently results from the $PIP_2$ headgroup acting as a bridge between positively charged residues on M3 and M4 (**figure 2.5C**). In the other conditions it never occurs, including when $PIP_2$ is at both sites. These data show that $PIP_2$ binding at sites 1 or 2 influence the

motions of TREK-1 TM helices in different ways, with site 1 $PIP_2$ favoring the crystallographic M4-up state while site 2 $PIP_2$ promotes a partial transition to a more "M4-down-like" state. This offers a potential explanation for $PIP_2$ inhibition, as there is substantial evidence that the M4-down state is lower activity (Brohawn et al. 2014, Dong et al. 2015, McClenaghan et al. 2016, Aryal et al. 2017). Also note that there is evidence for a bound lipid at site 2 in the TREK-2 down-state structure and simulations of that structure showed stable lipid interactions along the zippered M3-M4 interface (Dong et al. 2015). Altogether, this could indicate dual and opposing effects of $PIP_2$ at site 2, where it promotes activation via electrostatic effects on the SF but also promotes inhibition via allosteric effects on the channel TM helices. However, from our data alone it is not possible to definitively say that $PIP_2$ at site 2 favors the M4-down state, as I never observe a full up-down transition.

If it is in fact the case that $PIP_2$ binding influences the up-down equilibrium of TREK-1 and its close relatives then I would also expect that the state of the channel should affect the strength of lipid interactions. Although available TREK-2 and TRAAK structures of M4-down states lack most of the pCt domain following M4 (Dong et al. 2015, Brohawn et al. 2013, Brohawn et. al. 2014), it is clear that transitions to this state would entirely reposition all of the key basic residues that form the basis for the $PIP_2$ interactions observed in the M4-up state. All my simulations reported here use the TREK-1 M4-up state structure and should be considered with that context in mind. In order to fully understand the regulation of TREK-1 by lipids, future computational efforts should focus on understanding the energy landscape of the up-down transition with the context of the full pCt domain, how factors such as lipid binding shift this landscape, and how the state of the channel affects the affinity of lipid interactions.

## METHODS

Except where otherwise noted, simulation data processing and analysis used custom python/numpy/matplotlib code built on top of the MDAnalysis software package (Hunter 2007, Michaud-Agrawal et al. 2011, Harris et al. 2020). Simulations and analysis were run using a combination of the shared UCSF Wynton computing cluster and a local GPU cluster operated by the Grabe laboratory.

*Initial TREK-1 structural model*

The TREK-1 structural model used for all coarse-grain and atomistic MD simulations was based on a symmetrized version of PDBID 6CQ6, the mTREK-1 crystallization construct containing residues 35-321 and an intermolecular disulfide bond in the cap domain at residue Cys93 (Lolicato et al. 2017). Crystal contacts in the 6CQ6 structure cause a portion of the M2-M3 hairpin region to be partially unfolded compared to the conformation observed in structures of closely related $K_{2P}$ channels. Therefore, residues 191-208 were manually rebuilt using the structure of TRAAK (PDBID 4I9W) as a template (Brohawn et al. 2013).

*Preparation of coarse-grained simulation systems*

For coarse-grained (CG) simulations the TREK-1 model was parameterized using the Martini v2.2 polarizable force-field with an ElNeDyn elastic network model (Marrink et al. 2004, Marrink et al. 2007, Monticelli et al. 2008, Periole et al. 2009, Yesylevskyy et al. 2010, de Jong et al. 2013). The default ElNeDyn parameterization provided by the 'martinize.py' script did not result in realistic dynamics as compared to all-atom simulations in certain extended helical portions of the TREK-1 structure, namely the C-terminal portions of M4 and the M2-M3 hairpin. To stabilize these regions, additional elastic bonds were manually added between M2-M4 and

M3-M4, while increasing the force constant to 2500 kJ/mol/nm$^2$ (~6 kcal/mol/Å$^2$) for certain existing intrahelical elastic bonds in the ranges from residues 188-199, 203-209, and 283-317. In test simulations, the resulting model remained closer to the starting structure than the original and exhibited fluctuations in interhelical distances comparable to what was seen in all-atom simulations; this model was used for all subsequent CG simulations. All CG membrane systems were initially constructed using the 'insane.py' Martini script (Wassenaar et al. 2015). Current Martini v2 lipid topologies available from the Martini website ('www.cgmartini.nl') were used for most lipids (POPC, POPS, POPE, POPA, CHOL, & DBSM) (Marrink et al. 2004, Marrink et al. 2007, Baoukina et al. 2008, Ingólfsson et al. 2014, Wassenaar et al. 2015, Melo et al. 2015), with the exception of POP2 (alias for $PIP_2$) (López et al. 2013) which was modified to carry a −4 charge instead of the default −5, in line with the expected protonation state of $PIP_2$ at physiological pH (van Paridon et al. 1986) and in order to match the charge of $PIP_2$ used in all-atom simulations. Systems were solvated with Martini polarizable water (Yesylevskyy et al. 2010), and approximately 120 mM $K^+$ was added with neutralizing $Cl^-$. Simulation systems for umbrella sampling simulations were prepared similarly, except that they used TREK1-$PIP_2$ bound complexes extracted from previous unbiased simulations as input structures and used only POPC as the bulk lipid in the membrane.

*Preparation of atomistic simulation systems*

For atomistic MD simulations 10 water molecules were placed into the cavities between the selectivity filter and pore helices at high occupancy sites observed in previous TREK-1 simulations (Lolicato et al. 2020). Despite the lack of resolved water molecules in available TREK-1 crystal structures, it is well established that similar cavities in other $K^+$ channels host

slowly exchanging structural water molecules (Ostmeyer et al. 2013, Cuello et al. 2017), and this addition greatly stabilizes the selectivity filter in subsequent simulations. Protein N-termini were capped with acetyl groups and C-termini with methylamide groups. In contrast to the CG simulations (which used the mTREK-1 crystal construct sequence which has several differences from the WT mTREK-1 sequence), for most atomistic simulations all residues were reverted to their WT mTREK-1 identities using the PyMOL 'Mutagenesis Wizard' (the PyMOL Molecular Graphics System, Version 2.4/2.5 Schrödinger, LLC). The model of the TREK-1 M4-5A mutant (R297A / K301A / K302A / K304A / R311A) was then created on this WT background using the same method. All atomistic simulations were initialized with 4 $K^+$ ions in the selectivity filter at sites S1, S2, S3, and S4 as positioned in the crystal structure 6CQ6 (Lolicato et al. 2017). For atomistic simulations containing $PIP_2$ at specific binding sites, random lipid conformations out of all those with the lipid at the desired site were extracted from unbiased CG simulations and 'backmapped' to fully atomistic 1-stearoyl-2-arachidonoyl-glycero-3-phosphatidylinositol 4,5-bisphosphate. Briefly, CG protein-lipid complexes were aligned locally to secondary structural elements near the binding site on the initial all-atom TREK-1 structure to optimally align binding site residues. Then the positions of CG lipid particles were used as restraints in short implicit-solvent MD simulations using NAMD 2.13 (Phillips et al. 2020) to fit atomistic lipids into poses analogous to those of the CG lipids. This procedure was performed one lipid at a time, and then combinations of the 'backmapped' lipid structures were used to assemble complexes with multiple bound lipids. The remaining parts of these systems were prepared using the CHARMM-GUI membrane builder application (Wu et al. 2014, Lee et al. 2016). All systems contained 150 mM $K^+$ and neutralizing $Cl^-$. Aside from any $PIP_2$ lipids complexed with TREK-1, membranes were

constructed as a 7:3 mixture of POPC:cholesterol. The force field parameters used for protein, phospholipids, cholesterol, and water were CHARMM36m protein (Best et al. 2012, Huang et al. 2017), CHARMM36 lipid (Klauda et al. 2010), C36c (Lim et al. 2012), and CHARMM TIP3P (Jorgensen et al. 1983), respectively. Standard CHARMM parameters were used for ions (Beglov & Roux 1994).

*CG-MD simulation parameters*

Martini CG simulations were run using GPU accelerated builds of the GROMACS software package (versions 2018.8 and 2020.6) (Abraham et al. 2015). Systems were initially minimized with 1000 steps of steepest descent minimization, after which particle velocities were assigned according to a Maxwell-Boltzmann distribution at 303 K. This was followed by 5 ns of equilibration with positional restraints on protein backbone particles. CG simulations were propagated with a 20 fs timestep, temperature was maintained at 303 K with a stochastic velocity-rescaling thermostat (Bussi et al. 2007), and pressure was held at 1 atmosphere with a Parrinello-Rahman barostat (Parrinello & Rahman 1981, Nosé & Klein 1983 ). Short range non-bonded interactions were cut off at 11 Å, while long range electrostatics were treated with the particle mesh Ewald method (Darden et al. 1993, Essmann et al. 1995). Bond and angle constraints were enforced using the LINCS algorithm (Hess et al. 1997).

See **table 2.1** for a list of unbiased CG simulations.

*Free energy calculations*

Free energy calculations for $PIP_2$ binding to TREK-1 were preformed using a replica-exchange umbrella sampling protocol (Domański et al. 2017, Sugita et al. 2000). Reaction coordinates were defined along a vector in the XY plane from the center of mass of the protein

through the average center of mass of lipids in the target binding site cluster, as determined from unbiased simulations, and the 1D collective variable (CV) was defined as the center of mass distance between the protein and lipid in the XY plane. Initial conformations in each window were generated via steered MD, either by pushing the lipid along the reaction coordinate into the binding site from a starting point in the bulk membrane, or by pulling the lipid away from the protein from a starting point in the binding site. To restrict sampling to the linear reaction coordinate, the protein had to be restrained from rotating and translating in the plane of the membrane. This was achieved by harmonically restraining several TREK-1 backbone beads with a force constant of 200 kJ/mol/nm$^2$ (~0.5 kcal/mol/Å$^2$). Additionally, flat-bottom harmonic restraints with a force constant of 50 kJ/mol/nm$^2$ (~0.1 kcal/mol/Å$^2$) were applied to the lipid center of mass to keep it in a narrow channel along the radial reaction coordinate and prevent angular drift. This force effectively restricted the sampled area to a 25 Å wide lane parallel to the CV vector.

For each binding site two separate umbrella sampling simulations were run, one for each initialization approach (steered MD into or out of the site) and simulations were run until the free energy profiles for the two runs approximately converged (**figure 2.8**). The final PMFs were then calculated using aggregated data from the final half of both runs. For all calculations umbrella potentials of 1000 kJ/mol/nm$^2$ (2.4 kcal/mol/Å$^2$) and a spacing of 0.5 Å between umbrella centers were used. Biasing forces were applied using the GROMACS pull code parameters, and exchanges were calculated using a custom python script. Exchanges of umbrella potentials between replicas used the Boltzmann criterion, where the difference in

energies of the replicas in each window before and after a trial exchange controls the probability of the exchange:

$$\Delta = \frac{1}{k_B T}[U_1(X_2) + U_2(X_1) - U_1(X_1) - U_2(X_2)]$$

Here $U_1$ and $U_2$ are the two umbrella potentials initially associated with the two replicas attempting exchange, the replicas have molecular configurations $X_1$ and $X_2$; $k_B$ is Boltzmann's constant, and $T$ is the temperature. The exchange was then evaluated based on the Metropolis criterion, i.e. if $e^{-\Delta} \geq 1$ it was always accepted and if $e^{-\Delta} < 1$ it was accepted if a random number drawn from a uniform distribution on [0,1) was less than $e^{-\Delta}$. Exchanges were attempted every 5 ns, and for efficiency they were restricted to neighboring umbrella windows. The first half of each simulation was discarded as equilibration and then PMFs were calculated from the remaining data using the Weighted Histogram Analysis Method (WHAM) (Kumar et al. 1992), as implemented in GROMACS version 2018.8 (Hub et al. 2010). Errors were calculated using a Bayesian bootstrap after dividing the simulation data for each site into 8 bins.

See **table 2.2** for a list of umbrella sampling CG simulations.

*Atomistic MD simulation parameters*

Atomistic simulations were run using GPU accelerated builds of the GROMACS software package (version 2020.6). All systems were initially energy minimized with strong harmonic restraints on all protein heavy atoms, after which particle velocities were assigned according to a Maxwell-Boltzmann distribution at 100 K. The systems were then heated to 310 K over the course of 50 ps while maintaining protein restraints, followed by a multistep equilibration in which restraints were gradually removed over 10 to 12 ns. Finally, after 30 ns of unrestrained equilibration in the NPT ensemble, the membrane potential was equilibrated to +200 mV

stepwise at a rate of 5 mV per nanosecond. The membrane potential was created by applying a constant electric field along the Z-axis of the simulation calculated as $E_{applied} = V/L_z$; $L_z$ is the average length of the periodic simulation cell in the Z dimension during the unrestrained equilibration period (Gumbart et al. 2012). Hydrogen mass repartioning was applied by shifting 2 amu of mass from each non-water heavy atom to its bonded hydrogen atoms, which enabled the use of a 4 fs timestep (Hopkins et al. 2015, Balusek et al. 2019). Temperature was maintained at 310 K with a v-rescale thermostat (Bussi et al. 2007), and pressure was held at 1 atm with a Berendsen barostat (Berendsen et al. 1984). Non-bonded interactions were cut off at 12 Å with force-switching applied to Lennard-Jones forces between 10 and 12 Å, while long-range electrostatics were treated with the particle mesh Ewald method (Darden et al. 1993, Essmann et al. 1995). Bond and angle constraints were enforced using the LINCS algorithm (Hess et al. 1997).

See **table 2.3** for a list of all-atom simulations.

*Identification of lipid binding sites*

To identify specific, unique lipid binding sites on the surface of TREK-1 in our CG simulations I developed a novel clustering and assignment method using the framework of a Markov state model (MSM) that takes into account both spatial and temporal information about protein-lipid contacts. This method was implemented in python notebooks, using tools for dimensionality reduction, clustering, and MSM construction from the PyEMMA software package (Scherer et al. 2015). Firstly, lipid-protein contacts were encoded using the scheme illustrated in **figure 2.9A**. Each lipid was divided into several groups of particles, typically the headgroup, glycerol backbone, and lipid tails. Then for all lipid-protein pairs over all simulation

time I calculated which, if any, protein residues lay within contact distance (6.5 Å) of any particles in each of the lipid particle groups. From this information a 'contact vector' was generated for each lipid group, with length equal to the number of protein residues, and values of either 0 (no contact) or 1 (contact) at each position, with the $i^{th}$ value reporting on contact for the $i^{th}$ protein residue. A 'contact vector' for the full lipid is generated by concatenating the vectors for each of the individual particle groups, as shown in **figure 2.9A**. This procedure is then applied to every lipid of a particular species at every saved timepoint over the simulation trajectory, resulting in a collection of 'lipid contact trajectories', each describing the protein contact history of a single lipid. If multiple independent MD trajectories are used, the number of such 'lipid contact trajectories' will be *n* MD simulations x *m* lipids of interest. In the case of the data presented in **figure 2.4** of the present work, this is 6 MD simulations x 23 $PIP_2$ lipids, or 138 $PIP_2$ contact trajectories, each with length 100 μs and a sampling rate of 50 ns.

At this point dimensionality reduction is applied to the 'lipid contact trajectories' in the form of a time-lagged independent component analysis (tICA) (Molgedey & Schuster 1994, Pérez-Hernández et al. 2013). tICA calculates a linear transformation of the input data that separates the components of the data according to their autocorrelation at the specified lag time. The dimensionality reduction is achieved by discarding the fastest components and keeping the slowest ones, which preserves most of the information about slow processes like lipid binding. In the present work I used a lag time of 500 ns and retained tICA components corresponding to 80% of the cumulative kinetic variance for further analysis of $PIP_2$ binding.

After dimensionality reduction, an initial round of k-means clustering in the tICA subspace is used to discretize the contacts into ~100 clusters. These are then used as a basis to

construct an MSM. Timescale analysis showed that an MSM lag time of 1 μs was appropriate for analysis of $PIP_2$ in my simulations (**figure 2.9B**) and for the dataset shown in **figure 2.4** this model contains 16 implied timescales slower than 1 μs (**figure 2.9C**). The PCCA+ method is then used to cluster lipid contacts into metastable states (**figure 2.9D**) (Röblitz & Weber 2013). When I examined the average lipid-protein contacts as well as example lipid conformations for each of these metastable clusters, it was clear that they represented localized patches on the surface of the protein resembling binding sites, with identical sites observed at the equivalent positions on each of the two TREK-1 subunits. For sites 1 and 2 it also was apparent that I was detecting two to three temporally distinct binding modes at the same spatial binding site, which are likely related to each other by lipid or protein conformational changes. For the purposes of analyzing TREK-1 – $PIP_2$ interaction lifetimes, any such clusters that co-occurred at the same spatial site were merged together, and in addition, each of the symmetry related binding sites across the TREK-1 homodimer were treated as equivalent.

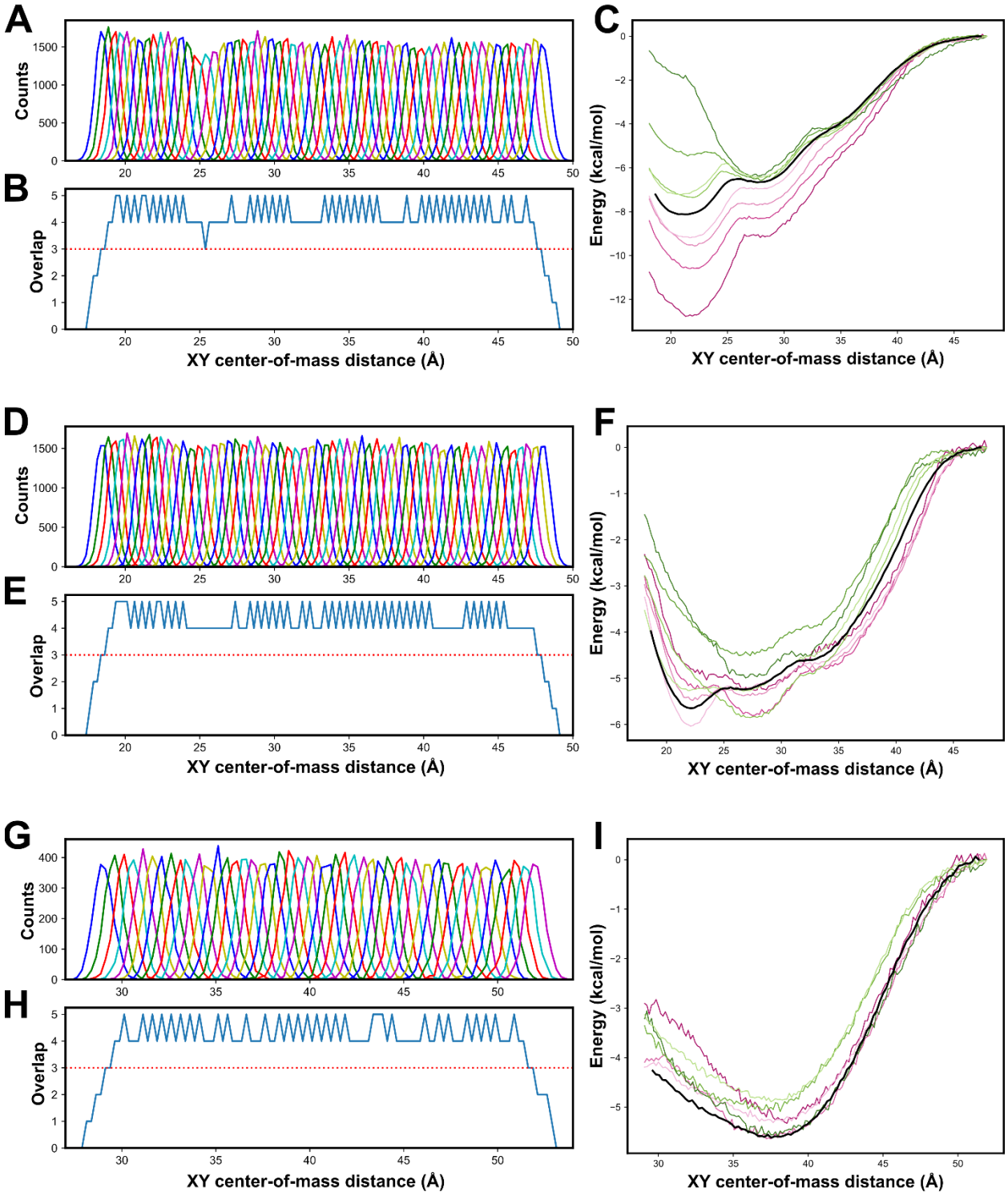


**Figure 2.8: Convergence analysis of umbrella sampling simulations**

**Figure 2.8 Legend. (A)-(C)** Convergence analysis for binding site 1 umbrella sampling simulations. **(A)** Umbrella histograms in each window for the data included in the final PMF shown in **figure 2.4 E**. **(B)** The degree of histogram overlap for the data shown in **(A)**. The value of the blue line is the number of histograms covering each point, histograms are counted wherever they are greater than 10% of their maximum value. The final PMF was calculated over the region where every point is covered by at least 3 histograms (red dotted line). **(C)** PMFs calculated from the data for simulations seeded from $PIP_2$ bound (pink) and unbound (green) conformations. PMFs were calculated from different time sections of each umbrella sampling run, from darkest to lightest color: 500-1000 ns, 1000- 2000 ns, 2000-4000 ns, 4000-8000 ns. The final PMF (black curve) used combined data from both seeds from 4000-8000 ns. **(D)-(F)** Convergence analysis for binding site 2 umbrella sampling simulations, as in **(A)-(C)**. **(G)-(I)** Convergence analysis for binding site 3 umbrella sampling simulations, as in **(A)-(C)**. The time sections shown in panel **(I)** cover from darkest to lightest: 250-500 ns, 500-1000 ns, and 1000-2000 ns. The final PMF used combined data from both seeds from 1000-2000 ns.

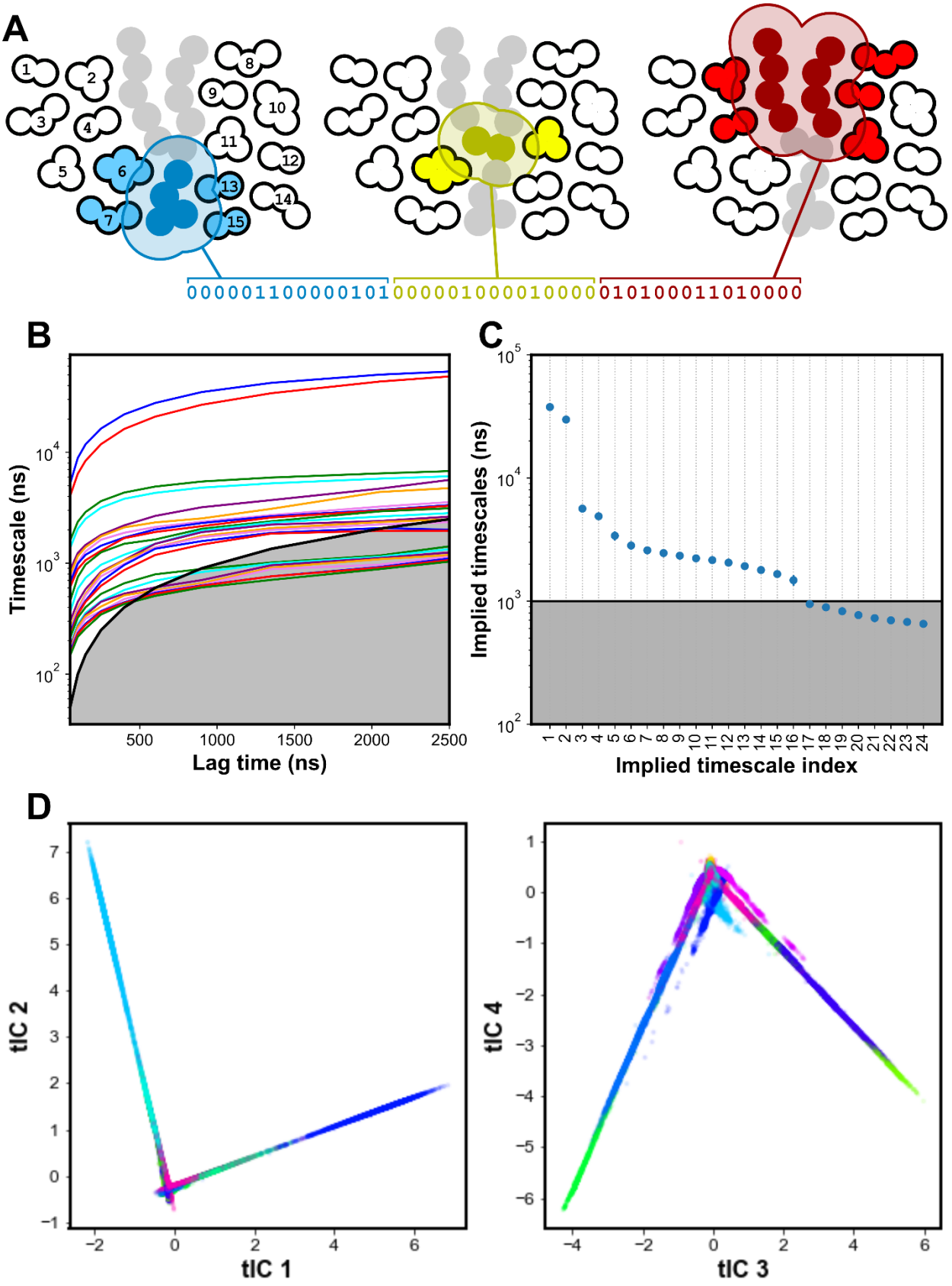


**Figure 2.9: A method for identifying lipid binding sites from MD simulations**

**Figure 2.9 Legend. (A)** Illustration of the process of converting protein-lipid conformations into lipid contact vectors. Circles represent coarse-grained beads or atoms, groups of black outlined circles represent protein residues, each with a fixed numerical identifier (left), gray and colored circles without black outlines together represent a single lipid molecule – blue indicates the headgroup, yellow the glycerol backbone, and red the fatty acid tails. A color filled interior of a protein residue indicates that the residue is inside the distance cutoff from a specific set of lipid beads/atoms. **(B)** Model lag time versus implied timescale for MSMs constructed from lipid binding contact trajectories from the simple membrane dataset presented in **figure 2.2. (C)** Ranking of implied timescales constructed from the same data as in **(B)** for a MSM constructed with a 1 μs lag time. The grey shaded area indicates timescales faster than the lag time. **(D)** Lipid contact vectors for the same data as in **(B) & (C)** projected into tICA space, along the 1$^{st}$ and 2$^{nd}$ (left) and 3$^{rd}$ and 4$^{th}$ independent components (ICs). Each dot represents a single lipid-protein conformation, and dots are colored according to cluster assignment after construction of an MSM and PCCA+ clustering.

**Table 2.1: List of unbiased CG simulations**

| ID #* | N particles | Upper leaflet | Lower leaflet | Total length (μs) |
|---|---|---|---|---|
| $1^{A}$ | 38378 | 100% PC | 9:1 PC:$PIP_2$ | 110 |
| $2^{A}$ | 38378 | | | 110 |
| $3^{A}$ | 38378 | | | 110 |
| $4^{B}$ | 38324 | | | 110 |
| $5^{B}$ | 38324 | | | 110 |
| $6^{B}$ | 38324 | | | 110 |
| $7^{C}$ | 37147 | 7:7:6 PC:SM:chol | 5:5:3:1:6 PC:PE:PS:$PIP_2$:chol | 210 |
| $8^{C}$ | 37147 | | | 210 |
| $9^{C}$ | 37147 | | | 210 |
| $10^{D}$ | 37192 | | | 210 |
| $11^{D}$ | 37192 | | | 210 |
| $12^{D}$ | 37192 | | | 210 |
| $13^{E}$ | 37279 | 7:7:6 PC:SM:chol | 5:5:3:1:6 PC:PE:PS:PA:chol | 110 |
| $14^{E}$ | 37279 | | | 110 |
| $15^{E}$ | 37279 | | | 110 |
| $16^{F}$ | 37213 | | | 110 |
| $17^{F}$ | 37213 | | | 110 |
| $18^{F}$ | 37213 | | | 110 |

*Simulations with the same superscript letter in ID were initialized from the same equilibration run.

**Table 2.2: List of umbrella sampling CG simulations**

| ID # | N particles | Binding site | Initialization strategy | N umbrella windows | Sampling per window (μs) |
|---|---|---|---|---|---|
| 1 | 30445 | site 1 | Steered MD from lipid bound in site to unbound | 61 | 8 |
| 2 | 31522 | site 1 | Steered MD from lipid unbound to binding site | 61 | 8 |
| 3 | 30571 | site 2 | Steered MD from lipid bound in site to unbound | 61 | 8 |
| 4 | 30670 | site 2 | Steered MD from lipid unbound to binding site | 61 | 8 |
| 5 | 31657 | site 3 | Steered MD from lipid bound in site to unbound | 47 | 2 |
| 6 | 30466 | site 3 | Steered MD from lipid unbound to binding site | 47 | 2 |

**Table 2.3: List of all-atom simulations**

| ID # | Protein model | N atoms | $PIP_2$ location | Total length (μs) | Conductive length (μs) | N $K^+$ permeations |
|---|---|---|---|---|---|---|
| 1 | TREK-1 WT | 205,586 | - | 5.5 | 0.75 | 4 |
| 2 | TREK-1 WT | 205,436 | - | 9.5 | 5.75 | 52 |
| 3 | TREK-1 WT | 204,743 | - | 10 | 10 | 111 |
| 4 | TREK-1 WT | 204,445 | - | 4 | 3.25 | 57 |
| 5 | TREK-1 WT | 205,530 | - | 1.5 | 0 | 0 |
| 6 | TREK-1 WT | 205,500 | - | 1.5 | 0 | 0 |
| 7 | TREK-1 WT | 204,140 | site 1 | 4 | 1.75 | 57 |
| 8 | TREK-1 WT | 204,311 | site 1 | 9 | 9 | 310 |
| 9 | TREK-1 WT | 204,104 | site 1 | 4 | 0 | 2 |
| 10 | TREK-1 WT | 204,191 | site 1 | 4 | 2.25 | 29 |
| 11 | TREK-1 WT | 204,694 | site 1 | 5 | 4.75 | 118 |
| 12 | TREK-1 WT | 204,485 | site 1 | 5 | 4.25 | 146 |
| 13 | TREK-1 WT | 203,981 | site 2 | 4 | 0.25 | 7 |
| 14 | TREK-1 WT | 204,703 | site 2 | 6 | 2.25 | 44 |
| 15 | TREK-1 WT | 205,036 | site 2 | 4 | 0 | 0 |
| 16 | TREK-1 WT | 204,335 | site 2 | 5 | 4.25 | 112 |
| 17 | TREK-1 WT | 204,703 | site 2 | 5 | 4.5 | 73 |
| 18 | TREK-1 WT | 204,379 | site 2 | 5 | 5 | 120 |
| 19 | TREK-1 WT | 203,987 | sites 1 & 2 | 8.5 | 4.75 | 96 |
| 20 | TREK-1 WT | 204,229 | sites 1 & 2 | 8.5 | 7.25 | 181 |
| 21 | TREK-1 WT | 204,721 | sites 1 & 2 | 9 | 8 | 180 |
| 22 | M4-5A | 205,448 | - | 3.5 | 3.5 | 56 |
| 23 | M4-5A | 205,298 | - | 2.5 | 1.75 | 53 |
| 24 | M4-5A | 204,605 | - | 3.5 | 3.5 | 125 |
| 25 | M4-5A | 204,307 | - | 3.5 | 3.5 | 127 |
| 26 | M4-5A | 205,392 | - | 3.5 | 2.5 | 83 |
| 27 | M4-5A | 205,362 | - | 3 | 1 | 24 |
| | | | Totals: | 137.5 | 93.75 | 2167 |

# REFERENCES


Abraham, M. J.; Murtola, T.; Schulz, R.; Páll, S.; Smith, J. C.; Hess, B.; Lindahl, E. GROMACS: High Performance Molecular Simulations through Multi-Level Parallelism from Laptops to Supercomputers. *SoftwareX* 2015, 1–2, 19–25. https://doi.org/10.1016/j.softx.2015.06.001.

Alloui, A.; Zimmermann, K.; Mamet, J.; Duprat, F.; Noël, J.; Chemin, J.; Guy, N.; Blondeau, N.; Voilley, N.; Rubat-Coudert, C.; Borsotto, M.; Romey, G.; Heurteaux, C.; Reeh, P.; Eschalier, A.; Lazdunski, M. TREK-1, a $K^+$ Channel Involved in Polymodal Pain Perception. *EMBO Journal* 2006, 25 (11), 2368–2376. https://doi.org/10.1038/sj.emboj.7601116.

Altis, A.; Nguyen, P. H.; Hegger, R.; Stock, G. Dihedral Angle Principal Component Analysis of Molecular Dynamics Simulations. *Journal of Chemical Physics* 2007, 126 (24), 244111. https://doi.org/10.1063/1.2746330.

Aryal, P.; Jarerattanachat, V.; Clausen, M. V.; Schewe, M.; McClenaghan, C.; Argent, L.; Conrad, L. J.; Dong, Y. Y.; Pike, A. C. W.; Carpenter, E. P.; Baukrowitz, T.; Sansom, M. S. P.; Tucker, S. J. Bilayer-Mediated Structural Transitions Control Mechanosensitivity of the TREK-2 $K_{2P}$ Channel. *Structure* 2017, 25 (5), 708-718. https://doi.org/10.1016/j.str.2017.03.006.

Balusek, C.; Hwang, H.; Lau, C. H.; Lundquist, K.; Hazel, A.; Pavlova, A.; Lynch, D. L.; Reggio, P. H.; Wang, Y.; Gumbart, J. C. Accelerating Membrane Simulations with Hydrogen Mass Repartitioning. *Journal of Chemical Theory and Computation* 2019, 15 (8), 4673–4686. https://doi.org/10.1021/acs.jctc.9b00160.

Bagriantsev, S. N.; Clark, K. A.; Minor, D. L. Metabolic and Thermal Stimuli Control $K_{2P}$2.1 (TREK-1) through Modular Sensory and Gating Domains. *EMBO Journal* 2012, 31 (15), 3297–3308. https://doi.org/10.1038/emboj.2012.171.

Bagriantsev, S. N.; Peyronnet, R.; Clark, K. A.; Honoré, E.; Minor, D. L. Multiple Modalities Converge on a Common Gate to Control $K_{2P}$ Channel Function. *EMBO Journal* 2011, 30 (17), 3594–3606. https://doi.org/10.1038/emboj.2011.230.

Baoukina, S.; Monticelli, L.; Risselada, H. J.; Marrink, S. J.; Tieleman, D. P. The Molecular Mechanism of Lipid Monolayer Collapse. *Proceedings of the National Academy of Sciences USA* 2008, 105 (31), 10803–10808. https://doi.org/10.1073/pnas.0711563105.

Baukrowitz, T.; Yellen, G. Modulation of $K^+$ Current by Frequency and External $[K^+]$: A Tale of Two Inactivation Mechanisms. *Neuron* 1995, 15 (4), 951–960. https://doi.org/10.1016/0896-6273(95)90185-X.

Beglov, D.; Roux, B. Finite Representation of an Infinite Bulk System: Solvent Boundary Potential for Computer Simulations. *Journal of Chemical Physics* 1994, 100 (12), 9050–9063. https://doi.org/10.1063/1.466711.

Berendsen, H. J. C.; Postma, J. P. M.; van Gunsteren, W. F.; DiNola, A.; Haak, J. R. Molecular Dynamics with Coupling to an External Bath. *Journal of Chemical Physics* 1984, 81 (8), 3684–3690. https://doi.org/10.1063/1.448118.

Berg, A. P.; Talley, E. M.; Manger, J. P.; Bayliss, D. A. Motoneurons Express Heteromeric TWIK-Related Acid-Sensitive $K^+$ (TASK) Channels Containing TASK-1 (KCNK3) and TASK-3 (KCNK9) Subunits. *Journal of Neuroscience* 2004, 24 (30), 6693–6702. https://doi.org/10.1523/JNEUROSCI.1408-04.2004.

Best, R. B.; Zhu, X.; Shim, J.; Lopes, P. E. M.; Mittal, J.; Feig, M.; MacKerell, A. D. Optimization of the Additive CHARMM All-Atom Protein Force Field Targeting Improved Sampling of the Backbone φ, ψ and Side-Chain $\chi_1$ and $\chi_2$ Dihedral Angles. *Journal of Chemical Theory and Computation* 2012, 8 (9), 3257–3273. https://doi.org/10.1021/ct300400x.

Blin, S.; Soussia, I. B.; Kim, E.; Brau, F.; Kang, D.; Lesage, F.; Bichet, D. Mixing and Matching TREK/TRAAK Subunits Generate Heterodimeric $K_{2P}$ Channels with Unique Properties. *Proceedings of the National Academy of Sciences USA* 2016, 113 (15), 4200–4205. https://doi.org/10.1073/pnas.1522748113.

Blin, S.; Chatelain, F. C.; Feliciangeli, S.; Kang, D.; Lesage, F.; Bichet, D. Tandem Pore Domain Halothane-Inhibited $K^+$ Channel Subunits THIK1 and THIK2 Assemble and Form Active Channels. *Journal of Biological Chemistry* 2014, 289 (41), 28202–28212. https://doi.org/10.1074/jbc.M114.600437.

Bockenhauer, D.; Zilberberg, N.; Goldstein, S. A. N. KCNK2: Reversible Conversion of a Hippocampal Potassium Leak into a Voltage-Dependent Channel. *Nature Neuroscience* 2001, 4 (5), 486–491. https://doi.org/10.1038/87434.

Brelidze, T. I.; Niu, X.; Magleby, K. L. A Ring of Eight Conserved Negatively Charged Amino Acids Doubles the Conductance of BK Channels and Prevents Inward Rectification. *Proceedings of the National Academy of Sciences USA* 2003, 100 (15), 9017–9022. https://doi.org/10.1073/pnas.1532257100.

Brennecke, J. T.; de Groot, B. L. Mechanism of Mechanosensitive Gating of the TREK-2 Potassium Channel. *Biophysical Journal* 2018, 114 (6), 1336–1343. https://doi.org/10.1016/j.bpj.2018.01.030.

Brohawn, S. G.; Campbell, E. B.; MacKinnon, R. Domain-Swapped Chain Connectivity and Gated Membrane Access in a Fab-Mediated Crystal of the Human TRAAK $K^+$ Channel. *Proceedings of the National Academy of Sciences USA* 2013, 110 (6), 2129–2134. https://doi.org/10.1073/pnas.1218950110.

Brohawn, S. G.; Campbell, E. B.; MacKinnon, R. Physical Mechanism for Gating and Mechanosensitivity of the Human TRAAK $K^+$ Channel. *Nature* 2014, 516 (7529), 126–130. https://doi.org/10.1038/nature14013.

Brohawn, S. G.; del Mármol, J.; MacKinnon, R. Crystal Structure of the Human $K_{2P}$ TRAAK, a Lipid- and Mechano-Sensitive $K^+$ Ion Channel. *Science* 2012, 335 (6067), 436–441. https://doi.org/10.1126/science.1213808.

Brohawn, S. G.; Wang, W.; Handler, A.; Campbell, E. B.; Schwarz, J. R.; MacKinnon, R. The mechanosensitive ion channel TRAAK is localized to the mammalian node of Ranvier. *eLife* 2019, 8:e50403. https://doi.org/10.7554/eLife.50403.

Bussi, G.; Donadio, D.; Parrinello, M. Canonical Sampling through Velocity Rescaling. *Journal of Chemical Physics* 2007, 126 (1), 014101. https://doi.org/10.1063/1.2408420.

Cabanos, C.; Wang, M.; Han, X.; Hansen, S. B. A Soluble Fluorescent Binding Assay Reveals $PIP_2$ Antagonism of TREK-1 Channels. *Cell Reports* 2017, 20 (6), 1287–1294. https://doi.org/10.1016/j.celrep.2017.07.034.

Cai, M.; Jordan, P. C. How Does Vestibule Surface Charge Affect Ion Conduction and Toxin Binding in a Sodium Channel? *Biophysical Journal* 1990, 57 (4), 883–891. https://doi.org/10.1016/S0006-3495(90)82608-4.

Carvacho, I.; Gonzalez, W.; Torres, Y. P.; Brauchi, S.; Alvarez, O.; Gonzalez-Nilo, F. D.; Latorre, R. Intrinsic Electrostatic Potential in the BK Channel Pore: Role in Determining Single Channel Conductance and Block. *Journal of General Physiology* 2008, 131 (2), 147–161. https://doi.org/10.1085/jgp.200709862.

Chemin, J.; Patel, A. J.; Duprat, F.; Lauritzen, I.; Lazdunski, M.; Honoré, E. A Phospholipid Sensor Controls Mechanogating of the $K^+$ Channel TREK-1. *EMBO Journal* 2005, 24 (1), 44–53. https://doi.org/10.1038/sj.emboj.7600494.

Chemin, J.; Patel, A. J.; Duprat, F.; Sachs, F.; Lazdunski, M.; Honore, E. Up- and down-Regulation of the Mechano-Gated $K_{2P}$ Channel TREK-1 by $PIP_2$ and Other Membrane Phospholipids. *Pflügers Archiv - European Journal of Physiology* 2007, 455 (1), 97–103. https://doi.org/10.1007/s00424-007-0250-2.

Clausen, M. V.; Jarerattanachat, V.; Carpenter, E. P.; Sansom, M. S. P.; Tucker, S. J. Asymmetric Mechanosensitivity in a Eukaryotic Ion Channel. *Proceedings of the National Academy of Sciences USA* 2017, 114 (40), E8343–E8351. https://doi.org/10.1073/pnas.1708990114.

Cohen, A.; Ben-Abu, Y.; Hen, S.; Zilberberg, N. A Novel Mechanism for Human $K_{2P}2.1$ Channel Gating. *Journal of Biological Chemistry* 2008, 283 (28), 19448–19455. https://doi.org/10.1074/jbc.M801273200.

Comoglio, Y.; Levitz, J.; Kienzler, M. A.; Lesage, F.; Isacoff, E. Y.; Sandoz, G. Phospholipase D2 Specifically Regulates TREK Potassium Channels via Direct Interaction and Local Production of Phosphatidic Acid. *Proceedings of the National Academy of Sciences USA* 2014, 111 (37), 13547–13552. https://doi.org/10.1073/pnas.1407160111.

Consiglio, J. F.; Andalib, P.; Korn, S. J. Influence of Pore Residues on Permeation Properties in the Kv2.1 Potassium Channel. Evidence for a Selective Functional Interaction of $K^+$ with the Outer Vestibule. *Journal of General Physiology* 2003, 121 (2), 111–124. https://doi.org/10.1085/jgp.20028756.

Cordero-Morales, J. F.; Cuello, L. G.; Zhao, Y.; Jogini, V.; Cortes, D. M.; Roux, B.; Perozo, E. Molecular Determinants of Gating at the Potassium-Channel Selectivity Filter. *Nature Structural & Molecular Biology* 2006, 13 (4), 311–318. https://doi.org/10.1038/nsmb1069.

Corey, R. A.; Stansfeld, P. J.; Sansom, M. S. P.; The Energetics of Protein-Lipid Interactions as Viewed by Molecular Simulations. *Biochemical Society Transactions* 2019, 48, 25-37. https://doi.org/10.1042/BST20190149.

Cuello, L. G.; Cortes, D. M.; Perozo, E. The Gating Cycle of a $K^+$ Channel at Atomic Resolution. *eLife* 2017, 6, e28032. https://doi.org/10.7554/eLife.28032.

Cuello, L. G.; Jogini, V.; Cortes, D. M.; Perozo, E. Structural Mechanism of C-Type Inactivation in $K^+$ Channels. *Nature* 2010, 466 (7303), 203–208. https://doi.org/10.1038/nature09153.

Darden, T.; York, D.; Pedersen, L. Particle Mesh Ewald: An $N \cdot \log(N)$ Method for Ewald Sums in Large Systems. *Journal of Chemical Physics* 1993, 98 (12), 10089–10092. https://doi.org/10.1063/1.464397.

Decher, N.; Ortiz-Bonnin, B.; Friedrich, C.; Schewe, M.; Kiper, A. K.; Rinné, S.; Seemann, G.; Peyronnet, R.; Zumhagen, S.; Bustos, D.; Kockskämper, J.; Kohl, P.; Just, S.; González, W.; Baukrowitz, T.; Stallmeyer, B.; Schulze-Bahr, E. Sodium Permeable and “Hypersensitive”

TREK -1 Channels Cause Ventricular Tachycardia. *EMBO Molecular Medicine* 2017, 9 (4), 403–414. https://doi.org/10.15252/emmm.201606690.

de Jong, D. H.; Singh, G.; Bennett, W. F. D.; Arnarez, C.; Wassenaar, T. A.; Schäfer, L. V.; Periole, X.; Tieleman, D. P.; Marrink, S. J. Improved Parameters for the Martini Coarse-Grained Protein Force Field. *Journal of Chemical Theory and Computation* 2013, 9 (1), 687–697. https://doi.org/10.1021/ct300646g.

Derebe, M. G.; Sauer, D. B.; Zeng, W.; Alam, A.; Shi, N.; Jiang, Y. Tuning the Ion Selectivity of Tetrameric Cation Channels by Changing the Number of Ion Binding Sites. *Proceedings of the National Academy of Sciences USA* 2011, 108 (2), 598–602. https://doi.org/10.1073/pnas.1013636108.

Devaraneni, P. K.; Komarov, A. G.; Costantino, C. A.; Devereaux, J. J.; Matulef, K.; Valiyaveetil, F. I. Semisynthetic $K^+$ Channels Show That the Constricted Conformation of the Selectivity Filter Is Not the C-Type Inactivated State. *Proceedings of the National Academy of Sciences USA* 2013, 110 (39), 15698–15703. https://doi.org/10.1073/pnas.1308699110.

Devilliers, M.; Busserolles, J.; Lolignier, S.; Deval, E.; Pereira, V.; Alloui, A.; Christin, M.; Mazet, B.; Delmas, P.; Noel, J.; Lazdunski, M.; Eschalier, A. Activation of TREK-1 by Morphine Results in Analgesia without Adverse Side Effects. *Nature Communications* 2013, 4 (1), 2941. https://doi.org/10.1038/ncomms3941.

Domański, J.; Hedger, G.; Best, R. B.; Stansfeld, P. J.; Sansom, M. S. P. Convergence and Sampling in Determining Free Energy Landscapes for Membrane Protein Association. *Journal of Physical Chemistry B* 2017, 121 (15), 3364–3375. https://doi.org/10.1021/acs.jpcb.6b08445.

Dong, Y. Y.; Pike, A. C. W.; Mackenzie, A.; McClenaghan, C.; Aryal, P.; Dong, L.; Quigley, A.; Grieben, M.; Goubin, S.; Mukhopadhyay, S.; Ruda, G. F.; Clausen, M. V.; Cao, L.; Brennan, P. E.; Burgess-Brown, N. A.; Sansom, M. S. P.; Tucker, S. J.; Carpenter, E. P. $K_{2P}$ Channel Gating Mechanisms Revealed by Structures of TREK-2 and a Complex with Prozac. *Science* 2015, 347 (6227), 1256–1259. https://doi.org/10.1126/science.1261512.

Duncan, A. L.; Song, W.; Sansom, M. S. P. Lipid-Dependent Regulation of Ion Channels and G Protein–Coupled Receptors: Insights from Structures and Simulations. *Annual Review of Pharmacology and Toxicology* 2020, 60 (1), 31–50. https://doi.org/10.1146/annurev-pharmtox-010919-023411.

Duprat, F.; Lesage, F.; Fink, M.; Reyes, R.; Heurteaux, C.; Lazdunski, M. TASK, a human background $K^+$ channel to sense external pH variations near physiological pH. *EMBO Journal* 1997, 16 (17), 5464–5471. https://doi.org/10.1093/emboj/16.17.5464.

Enyedi, P.; Czirják, G. Molecular Background of Leak $K^+$ Currents: Two-Pore Domain Potassium Channels. *Physiological Reviews* 2010, 90 (2), 559–605. https://doi.org/10.1152/physrev.00029.2009.

Essmann, U.; Perera, L.; Berkowitz, M. L.; Darden, T.; Lee, H.; Pedersen, L. G. A Smooth Particle Mesh Ewald Method. *Journal of Chemical Physics* 1995, 103 (19), 8577–8593. https://doi.org/10.1063/1.470117.

Feliciangeli, S.; Chatelain, F. C.; Bichet, D.; Lesage, F. The Family of $K_{2P}$ Channels: Salient Structural and Functional Properties. *Journal of Physiology* 2015, 593 (12), 2587–2603. https://doi.org/10.1113/jphysiol.2014.287268.

Fink, M.; Duprat, F.; Lesage, F.; Reyes, R.; Romey, G.; Heurteaux, C.; Lazdunski, M. Cloning, functional expression and brain localization of a novel unconventional outward rectifier K+ channel. *EMBO Journal* 1996, 15 (24), 6854-6862. https://doi.org/10.1002/j.1460-2075.1996.tb01077.x.

Fink, M.; Lesage, F.; Duprat, F.; Heurteaux, C.; Reyes, R.; Fosset, M.; Lazdunski, M. A neuronal two P domain $K^+$ channel stimulated by arachidonic acid and polyunsaturated fatty acids. *EMBO Journal* 1998, 17 (12), 3297–3308. https://doi.org/10.1093/emboj/17.12.3297.

Gumbart, J.; Khalili-Araghi, F.; Sotomayor, M.; Roux, B. Constant Electric Field Simulations of the Membrane Potential Illustrated with Simple Systems. *Biochimica et Biophysica Acta (BBA) - Biomembranes* 2012, 1818 (2), 294–302. https://doi.org/10.1016/j.bbamem.2011.09.030.

Guizouarn, H.; Gabillat, N.; Motais, R.; Borgese, F. Multiple Transport Functions of a Red Blood Cell Anion Exchanger, TAE1: Its Role in Cell Volume Regulation. *Journal of Physiology* 2001, 535 (2), 497–506. https://doi.org/10.1111/j.1469-7793.2001.t01-1-00497.x.

Hansen, S. B.; Tao, X.; MacKinnon, R. Structural Basis of $PIP_2$ Activation of the Classical Inward Rectifier $K^+$ Channel $K_{ir}2.2$. *Nature* 2011, 477 (7365), 495–498. https://doi.org/10.1038/nature10370.

Harrigan, M. P.; McKiernan, K. A.; Shanmugasundaram, V.; Denny, R. A.; Pande, V. S. Markov Modeling Reveals Novel Intracellular Modulation of the Human TREK-2 Selectivity Filter. *Scientific Reports* 2017, 7 (1), 632. https://doi.org/10.1038/s41598-017-00256-y.

Harris, C. R.; Millman, K. J.; van der Walt, S. J.; Gommers, R.; Virtanen, P.; Cournapeau, D.; Wieser, E.; Taylor, J.; Berg, S.; Smith, N. J.; Kern, R.; Picus, M.; Hoyer, S.; van Kerkwijk, M. H.; Brett, M.; Haldane, A.; del Río, J. F.; Wiebe, M.; Peterson, P.; Gérard-Marchant, P.; Sheppard, K.; Reddy, T.; Weckesser, W.; Abbasi, H.; Gohlke, C.; Oliphant, T. E. Array Programming with NumPy. *Nature* 2020, 585 (7825), 357–362. https://doi.org/10.1038/s41586-020-2649-2.

Hess, B.; Bekker, H.; Berendsen, H. J. C.; Fraaije, J. G. E. M. LINCS: A Linear Constraint Solver for Molecular Simulations. *Journal of Computational Chemistry* 1997, 18 (12), 1463–1472.

Heurteaux, C.; Guy, N.; Laigle, C.; Blondeau, N.; Duprat, F.; Mazzuca, M.; Lang-Lazdunski, L.; Widmann, C.; Zanzouri, M.; Romey, G.; Lazdunski, M. TREK-1, a $K^+$ Channel Involved in Neuroprotection and General Anesthesia. *EMBO Journal* 2004, 23 (13), 2684–2695. https://doi.org/10.1038/sj.emboj.7600234.

Heurteaux, C.; Lucas, G.; Guy, N.; El Yacoubi, M.; Thümmler, S.; Peng, X.; Noble, F.; Blondeau, N.; Widmann, C.; Borsotto, M.; Gobbi, G.; Vaugeois, J.; Debonnel, G.; Lazdunski, M. Deletion of the background potassium channel TREK-1 results in a depression-resistant phenotype. *Nature Neuroscience* 2006, 9 (9), 1134-1141. https://doi.org/10.1038/nn1749.

Hilgemann, D. W.; Feng, S.; Nasuhoglu, C. The Complex and Intriguing Lives of $PIP_2$ with Ion Channels and Transporters. *Science's STKE* 2001, 111. https://doi.org/10.1126/stke.2001.111.re19.

Hille, B. *Ionic Channels of Excitable Membranes*, 3rd ed; Sinauer Associates, 2001.

Hodgkin, A. L.; Huxley, A. F. Potassium Leakage from an Active Nerve Fibre. *Journal of Physiology* 1947, 106, 341-367. https://doi.org/10.1113/jphysiol.1947.sp004216.

Hodgkin, A. L.; Huxley, A. F. A Quantitative Description of Membrane Current and its Application to Conduction and Excitation in Nerve. *Journal of Physiology* 1952, 117, 500-544. https://doi.org/10.1113/jphysiol.1952.sp004764.

Hodgkin, A. L.; Katz, B. The Effect of Sodium Ions on the Electrical Activity of the Giant Axon of the Squid. *Journal of Physiology* 1949, 108, 37-77. https://doi.org/10.1113/jphysiol.1949.sp004310.

Honoré, E.; Maingret, F.; Lazdunski, M.; Patel, A. J. An Intracellular Proton Sensor Commands Lipid- and Mechano-Gating of the $K^+$ Channel TREK-1. *EMBO Journal* 2002, 21 (12), 2968–2976. https://doi.org/10.1093/emboj/cdf288.

Hoover, W. G. Canonical dynamics: Equilibrium phase-space distributions. Physical Review A 1985, 31, 1695–1697. https://doi.org/10.1103/PhysRevA.31.1695.

Hopkins, C. W.; Le Grand, S.; Walker, R. C.; Roitberg, A. E. Long-Time-Step Molecular Dynamics through Hydrogen Mass Repartitioning. *Journal of Chemical Theory and Computation* 2015, 11 (4), 1864–1874. https://doi.org/10.1021/ct5010406.

Hoshi, T.; Armstrong, C. M. C-Type Inactivation of Voltage-Gated $K^+$ Channels: Pore Constriction or Dilation? *Journal of General Physiology* 2013, 141 (2), 151–160. https://doi.org/10.1085/jgp.201210888.

Huang, J.; Rauscher, S.; Nawrocki, G.; Ran, T.; Feig, M.; de Groot, B. L.; Grubmüller, H.; MacKerell, A. D. CHARMM36m: An Improved Force Field for Folded and Intrinsically

Disordered Proteins. *Nature Methods* 2017, 14 (1), 71–73. https://doi.org/10.1038/nmeth.4067.

Huang, P.; Ban, Y. A.; Richter, F.; Andre, I.; Vernon, R.; Schief, W. R.; Baker, D. RosettaRemodel: A Generalized Framework for Flexible Backbone Protein Design. *PLoS ONE* 2011, 6 (8), e24109. https://doi.org/10.1371/journal.pone.0024109.

Hub, J. S.; de Groot, B. L.; van der Spoel, D. G_wham—A Free Weighted Histogram Analysis Implementation Including Robust Error and Autocorrelation Estimates. *Journal of Chemical Theory and Computation* 2010, 6 (12), 3713–3720. https://doi.org/10.1021/ct100494z.

Hunter, J. D. Matplotlib: A 2D Graphics Environment. *Computing in Science & Engineering* 2007, 9 (3), 90–95. https://doi.org/10.1109/MCSE.2007.55.

Imoto, K.; Busch, C.; Sakmann, B.; Mishina, M.; Konno, T.; Nakai, J.; Bujo, H.; Mori, Y.; Fukuda, K.; Numa, S. Rings of Negatively Charged Amino Acids Determine the Acetylcholine Receptor Channel Conductance. *Nature* 1988, 335 (6191), 645–648. https://doi.org/10.1038/335645a0.

Ingólfsson, H. I.; Melo, M. N.; van Eerden, F. J.; Arnarez, C.; Lopez, C. A.; Wassenaar, T. A.; Periole, X.; de Vries, A. H.; Tieleman, D. P.; Marrink, S. J. Lipid Organization of the Plasma Membrane. *Journal of the American Chemical Society* 2014, 136 (41), 14554–14559. https://doi.org/10.1021/ja507832e.

Jekhmane, S.; Medeiros-Silva, J.; Li, J.; Kümmerer, F.; Müller-Hermes, C.; Baldus, M.; Roux, B.; Weingarth, M. Shifts in the Selectivity Filter Dynamics Cause Modal Gating in $K^+$

Channels. *Nature Communications* 2019, 10 (1), 123. https://doi.org/10.1038/s41467-018-07973-6.

Jo, S.; Kim, T.; Im, W. Automated Builder and Database of Protein/Membrane Complexes for Molecular Dynamics Simulations. *PLoS ONE* 2007, 2 (9), e880. https://doi.org/10.1371/journal.pone.0000880.

Jorgensen, W. L.; Chandrasekhar, J.; Madura, J. D.; Impey, R. W.; Klein, M. L. Comparison of Simple Potential Functions for Simulating Liquid Water. *Journal of Chemical Physics* 1983, 79 (2), 926–935. https://doi.org/10.1063/1.445869.

Kanda, H.; Ling, J.; Tonomura, S.; Noguchi, K.; Matalon, S; Gu, J. G. TREK-1 and TRAAK Are Principal $K^+$ Channels at the Nodes of Ranvier for Rapid Action Potential Conduction on Mammalian Myelinated Afferent Nerves. *Neuron* 2019, 104, 960-971. https://doi.org/10.1016/j.neuron.2019.08.042.

Kim, Y.; Bang, H.; Gnatenco, C.; Kim, D. Synergistic Interaction and the Role of C-Terminus in the Activation of TRAAK $K^+$ Channels by Pressure, Free Fatty Acids and Alkali. *Pflügers Archiv - European Journal of Physiology* 2001, 442 (1), 64–72. https://doi.org/10.1007/s004240000496.

Klauda, J. B.; Venable, R. M.; Freites, J. A.; O'Connor, J. W.; Tobias, D. J.; Mondragon-Ramirez, C.; Vorobyov, I.; MacKerell, A. D.; Pastor, R. W. Update of the CHARMM All-Atom Additive Force Field for Lipids: Validation on Six Lipid Types. *Journal of Physical Chemistry B* 2010, 114 (23), 7830–7843. https://doi.org/10.1021/jp101759q.

Koh, S. D.; Monaghan, K.; Sergeant, G. P.; Ro, S.; Walker, R. L.; Sanders, K. M.; Horowitz, B. TREK-1 Regulation by Nitric Oxide and CGMP-Dependent Protein Kinase. *Journal of*

*Biological Chemistry* 2001, 276 (47), 44338–44346. https://doi.org/10.1074/jbc.M108125200.

Kumar, S.; Rosenberg, J. M.; Bouzida, D.; Swendsen, R. H.; Kollman, P. A. THE Weighted Histogram Analysis Method for Free-Energy Calculations on Biomolecules. I. The Method. *Journal of Computational Chemistry* 1992, 13 (8), 1011–1021. https://doi.org/10.1002/jcc.540130812.

Laigle, C.; Confort-Gouny, S.; Le Fur, Y.; Cozzone, P. J.; Viola, A. Deletion of TRAAK Potassium Channel Affects Brain Metabolism and Protects against Ischemia. *PLoS ONE* 2012, 7 (12), e53266. https://doi.org/10.1371/journal.pone.0053266.

Lambert, M.; Boet, A.; Rucker-Martin, C.; Mendes-Ferreira, P.; Capuano, V.; Hatem, S.; Adão, R.; Brás-Silva, C.; Hautefort, A.; Michel, J-.B.; Dorfmuller, P.; Fadel, E.; Kotsimbos, T.; Price, L.; Jourdon, P.; Montani, D.; Humbert, M.; Perros, F.; Antigny, F. Loss of KCNK3 is a hallmark of RV hypertrophy/dysfunction associated with pulmonary hypertension. *Cardiovascular Research* 2018, 114, 880-893. https://doi.org/10.1093/cvr/cvy016.

Larsson, H. P.; Elinder, F. A Conserved Glutamate Is Important for Slow Inactivation in $K^+$ Channels. *Neuron* 2000, 27 (3), 573–583. https://doi.org/10.1016/S0896-6273(00)00067-2.

Lazarenko, R. M.; Fortuna, M. G.; Shi, Y.; Mulkey, D. K.; Takakura, A. C.; Moreira, T. S.; Guyenet, P. G.; Bayliss, D. A. Anesthetic Activation of Central Respiratory Chemoreceptor Neurons Involves Inhibition of a THIK-1-Like Background $K^+$ Current. *Journal of Neuroscience* 2010, 30 (27), 9324–9334. https://doi.org/10.1523/JNEUROSCI.1956-10.2010.

Lee, J.; Cheng, X.; Swails, J. M.; Yeom, M. S.; Eastman, P. K.; Lemkul, J. A.; Wei, S.; Buckner, J.; Jeong, J. C.; Qi, Y.; Jo, S.; Pande, V. S.; Case, D. A.; Brooks, C. L.; MacKerell, A. D.; Klauda, J. B.; Im, W. CHARMM-GUI Input Generator for NAMD, GROMACS, AMBER, OpenMM, and CHARMM/OpenMM Simulations Using the CHARMM36 Additive Force Field. *Journal of Chemical Theory and Computation* 2016, 12 (1), 405–413. https://doi.org/10.1021/acs.jctc.5b00935.

Lees-Miller, J. P.; Duan, Y.; Teng, G. Q.; Thorstad, K.; Duff, H. J. Novel Gain-of-Function Mechanism in $K^+$ Channel–Related Long-QT Syndrome: Altered Gating and Selectivity in the HERG1 N629D Mutant. *Circulation Research* 2000, 86 (5), 507–513. https://doi.org/10.1161/01.RES.86.5.507.

Lengyel, M.; Czirják, G.; Enyedi, P. Formation of Functional Heterodimers by TREK-1 and TREK-2 Two-Pore Domain Potassium Channel Subunits. *Journal of Biological Chemistry* 2016, 291 (26), 13649–13661. https://doi.org/10.1074/jbc.M116.719039.

Lesage, F.; Guillemare, E.; Fink, M.; Duprat, F.; Lazdunski, M.; Romey, G.; Barhanin, J. TWIK-1, a ubiquitous human weakly inward rectifying $K^+$ channel with a novel structure. *EMBO Journal* 1996, 15 (5), 1004-1011. https://doi.org/10.1002/j.1460-2075.1996.tb00437.x.

Levitz, J.; Royal, P.; Comoglio, Y.; Wdziekonski, B.; Schaub, S.; Clemens, D. M.; Isacoff, E. Y.; Sandoz, G. Heterodimerization within the TREK Channel Subfamily Produces a Diverse Family of Highly Regulated Potassium Channels. *Proceedings of the National Academy of Sciences USA* 2016, 113 (15), 4194–4199. https://doi.org/10.1073/pnas.1522459113.

Li, J.; Ostmeyer, J.; Boulanger, E.; Rui, H.; Perozo, E.; Roux, B. Chemical Substitutions in the Selectivity Filter of Potassium Channels Do Not Rule out Constricted-like Conformations

for C-Type Inactivation. *Proceedings of the National Academy of Sciences USA* 2017, 114 (42), 11145–11150. https://doi.org/10.1073/pnas.1706983114.

Li, J.; Ostmeyer, J.; Cuello, L. G.; Perozo, E.; Roux, B. Rapid Constriction of the Selectivity Filter Underlies C-Type Inactivation in the KcsA Potassium Channel. *Journal of General Physiology* 2018, 150 (10), 1408–1420. https://doi.org/10.1085/jgp.201812082.

Li, R. A.; Vélez, P.; Chiamvimonvat, N.; Tomaselli, G. F.; Marbán, E. Charged Residues between the Selectivity Filter and S6 Segments Contribute to the Permeation Phenotype of the Sodium Channel. *Journal of General Physiology* 2000, 115 (1), 81–92. https://doi.org/10.1085/jgp.115.1.81.

Lim, J. B.; Rogaski, B.; Klauda, J. B. Update of the Cholesterol Force Field Parameters in CHARMM. *Journal of Physical Chemistry B* 2012, 116 (1), 203–210. https://doi.org/10.1021/jp207925m.

Liu, S.; Focke, P. J.; Matulef, K.; Bian, X.; Moënne-Loccoz, P.; Valiyaveetil, F. I.; Lockless, S. W. Ion-Binding Properties of a $K^+$ Channel Selectivity Filter in Different Conformations. *Proceedings of the National Academy of Sciences USA* 2015, 112 (49), 15096–15100. https://doi.org/10.1073/pnas.1510526112.

Logothetis, D. E.; Jin, T.; Lupyan, D.; Rosenhouse-Dantsker, A. Phosphoinositide-Mediated Gating of Inwardly Rectifying $K^+$ Channels. *Pflügers Archiv - European Journal of Physiology* 2007, 455 (1), 83–95. https://doi.org/10.1007/s00424-007-0276-5.

Lolicato, M.; Arrigoni, C.; Mori, T.; Sekioka, Y.; Bryant, C.; Clark, K. A.; Minor, D. L. $K_{2P}2.1$ (TREK-1)–Activator Complexes Reveal a Cryptic Selectivity Filter Binding Site. *Nature* 2017, 547 (7663), 364–368. https://doi.org/10.1038/nature22988.

Lolicato, M.; Natale, A. M.; Abderemane-Ali, F.; Crottès, D.; Capponi, S.; Duman, R.; Wagner, A.; Rosenberg, J. M.; Grabe, M.; Minor, D. L. $K_{2P}$ Channel C-Type Gating Involves Asymmetric Selectivity Filter Order-Disorder Transitions. *Science Advances* 2020, 6 (44), eabc9174. https://doi.org/10.1126/sciadv.abc9174.

Lolicato, M.; Riegelhaupt, P. M.; Arrigoni, C.; Clark, K. A.; Minor, D. L. Transmembrane Helix Straightening and Buckling Underlies Activation of Mechanosensitive and Thermosensitive $K_{2P}$ Channels. *Neuron* 2014, 84 (6), 1198–1212. https://doi.org/10.1016/j.neuron.2014.11.017.

Long, S. B.; Tao, X.; Campbell, E. B.; MacKinnon, R. Atomic Structure of a Voltage-Dependent $K^+$ Channel in a Lipid Membrane-like Environment. *Nature* 2007, 450 (7168), 376–382. https://doi.org/10.1038/nature06265.

Lopes, C. M. B.; Rohács, T.; Czirják, G.; Balla, T.; Enyedi, P.; Logothetis, D. E. $PIP_2$ Hydrolysis Underlies Agonist-Induced Inhibition and Regulates Voltage Gating of Two-Pore Domain $K^+$ Channels. *Journal of Physiology* 2005, 564 (1), 117–129. https://doi.org/10.1113/jphysiol.2004.081935.

López, C. A.; Sovova, Z.; van Eerden, F. J.; de Vries, A. H.; Marrink, S. J. Martini Force Field Parameters for Glycolipids. *Journal of Chemical Theory and Computation* 2013, 9 (3), 1694–1708. https://doi.org/10.1021/ct3009655.

López-Barneo, J.; Hoshi, T.; Heinemann, S. H.; Aldrich, R.W. Effects of external cations and mutations in the pore region on C-type inactivation of Shaker potassium channels. *Receptors and Channels*. 1993, 1 (1), 61-71. PMID: 8081712.

Ma, L.; Roman-Campos, D.; Austin, E. D.; Eyries, M.; Sampson, K. S.; Soubrier, F.; Germain, M.; Trégouët, D.-A.; Borczuk, A.; Rosenzweig, E. B.; Girerd, B.; Montani, D.; Humbert, M.; Loyd, J. E.; Kass, R. S.; Chung, W. K. A Novel Channelopathy in Pulmonary Arterial Hypertension. *New England Journal of Medicine* 2013, 369 (4), 351–361. https://doi.org/10.1056/NEJMoa1211097.

MacKinnon, R.; Latorre, R.; Miller, C. Role of Surface Electrostatics in the Operation of a High-Conductance Calcium-Activated Potassium Channel. *Biochemistry* 1989, 28 (20), 8092–8099. https://doi.org/10.1021/bi00446a020.

Madry, C.; Kyrargyri, V.; Arancibia-Cárcamo, I. L.; Jolivet, R.; Kohsaka, S.; Bryan, R. M., Attwell D. Microglial Ramification, Surveillance, and Interleukin-1β Release Are Regulated by the Two-Pore Domain $K^+$ Channel THIK-1. *Neuron* 2018, 97, 299–312. https://doi.org/10.1016/j.neuron.2017.12.002.

Maingret, F.; Lauritzen, I.; Patel, A. J.; Heurteaux, C.; Reyes, R.; Lesage, F.; Lazdunski, M.; Honoré, E. TREK-1 Is a Heat-Activated Background $K^+$ Channel. *EMBO Journal* 2000, 19 (11), 2483–2491. https://doi.org/10.1093/emboj/19.11.2483.

Maingret, F.; Patel, A. J.; Lesage, F.; Lazdunski, M.; Honoré, E. Mechano- or Acid Stimulation, Two Interactive Modes of Activation of the TREK-1 Potassium Channel. *Journal of Biological Chemistry*, 1999, 274 (38), 26691-26696. https://doi.org/10.1074/jbc.274.38.26691.

Maingret, F.; Patel, A. J.; Lesage, F.; Lazdunski, M.; Honoré, E. Lysophospholipids Open the Two-Pore Domain Mechano-Gated $K^+$ Channels TREK-1 and TRAAK. *Journal of Biological Chemistry* 2000, 275 (14), 10128–10133. https://doi.org/10.1074/jbc.275.14.10128.

Marrink, S. J.; de Vries, A. H.; Mark, A. E. Coarse Grained Model for Semiquantitative Lipid Simulations. *Journal of Physical Chemistry B* 2004, 108 (2), 750–760. https://doi.org/10.1021/jp036508g.

Marrink, S. J.; Risselada, H. J.; Yefimov, S.; Tieleman, D. P.; de Vries, A. H. The MARTINI Force Field: Coarse Grained Model for Biomolecular Simulations. *Journal of Physical Chemistry B* 2007, 111 (27), 7812–7824. https://doi.org/10.1021/jp071097f.

Martyna, G. J.; Tobias, D. J.; Klein, M. L.; Constant pressure molecular dynamics algorithms. *Journal of Chemical Physics* 1994, 101, 4177-4189. https://doi.org/10.1063/1.467468.

Mathie, A.; Veale, E. L.; Cunningham, K. P.; Holden, R. G.; Wright, P. D. Two-Pore Domain Potassium Channels as Drug Targets: Anesthesia and Beyond. *Annual Review of Pharmacology and Toxicology* 2021, 61 (1), 401–420. https://doi.org/10.1146/annurev-pharmtox-030920-111536.

Matthies, D.; Bae, C.; Toombes, G. E.; Fox, T.; Bartesaghi, A.; Subramaniam, S.; Swartz, K. J. Single-Particle Cryo-EM Structure of a Voltage-Activated Potassium Channel in Lipid Nanodiscs. *eLife* 2018, 7, e37558. https://doi.org/10.7554/eLife.37558.

McClenaghan, C.; Schewe, M.; Aryal, P.; Carpenter, E. P.; Baukrowitz, T.; Tucker, S. J. Polymodal Activation of the TREK-2 $K_{2P}$ Channel Produces Structurally Distinct Open States. *Journal of General Physiology* 2016, 147 (6), 497–505. https://doi.org/10.1085/jgp.201611601.

Melo, M. N.; Ingólfsson, H. I.; Marrink, S. J. Parameters for Martini Sterols and Hopanoids Based on a Virtual-Site Description. *Journal of Chemical Physics* 2015, 143 (24), 243152. https://doi.org/10.1063/1.4937783.

Michaud-Agrawal, N.; Denning, E. J.; Woolf, T. B.; Beckstein, O. MDAnalysis: A Toolkit for the Analysis of Molecular Dynamics Simulations. *Journal of Computational Chemistry* 2011, 32 (10), 2319–2327. https://doi.org/10.1002/jcc.21787.

Miller, A. N.; Long, S. B. Crystal Structure of the Human Two–Pore Domain Potassium Channel K2P1. *Science* 2012, 335 (6067), 432–436. https://doi.org/10.1126/science.1213274.

Miranda, W. E.; DeMarco, K. R.; Guo, J.; Duff, H. J.; Vorobyov, I.; Clancy, C. E.; Noskov, S. Yu. Selectivity Filter Modalities and Rapid Inactivation of the HERG1 Channel. *Proceedings of the National Academy of Sciences USA* 2020, 117 (6), 2795–2804. https://doi.org/10.1073/pnas.1909196117.

Molgedey, L.; Schuster, H. G. Separation of a Mixture of Independent Signals Using Time Delayed Correlations. *Physical Review Letters* 1994, 72 (23), 3634–3637. https://doi.org/10.1103/PhysRevLett.72.3634.

Monticelli, L.; Kandasamy, S. K.; Periole, X.; Larson, R. G.; Tieleman, D. P.; Marrink, S.-J. The MARTINI Coarse-Grained Force Field: Extension to Proteins. *Journal of Chemical Theory and Computation* 2008, 4 (5), 819–834. https://doi.org/10.1021/ct700324x.

Murbartián, J.; Lei, Q.; Sando, J. J.; Bayliss, D. A. Sequential Phosphorylation Mediates Receptor- and Kinase-Induced Inhibition of TREK-1 Background Potassium Channels. *Journal of Biological Chemistry* 2005, 280 (34), 30175–30184. https://doi.org/10.1074/jbc.M503862200.

Natale, A. M.; Deal, P. E.; Minor, D. L. Structural Insights into the Mechanisms and Pharmacology of $K_{2P}$ Potassium Channels. *Journal of Molecular Biology* 2021, 433 (17), 166995. https://doi.org/10.1016/j.jmb.2021.166995.

Niemeyer, M. I.; Cid, L. P.; Paulais, M.; Teulon, J.; Sepúlveda, F. V. Phosphatidylinositol (4,5)-Bisphosphate Dynamically Regulates the $K_{2P}$ Background $K^+$ Channel TASK-2. *Scientific Reports* 2017, 7 (1), 45407. https://doi.org/10.1038/srep45407.

Nimigean, C. M.; Chappie, J. S.; Miller, C. Electrostatic Tuning of Ion Conductance in Potassium Channels. *Biochemistry* 2003, 42 (31), 9263–9268. https://doi.org/10.1021/bi0348720.

Niu, Y.; Tao, X.; Touhara, K. K.; MacKinnon, R. Cryo-EM Analysis of $PIP_2$ Regulation in Mammalian GIRK Channels. *eLife* 2020, 9, e60552. https://doi.org/10.7554/eLife.60552.

Nosé, S. A molecular dynamics method for simulations in the canonical ensemble. Molecular Physics 1984, 52 (2), 255-268. https://doi.org/10.1080/00268978400101201.

Nosé, S.; Klein, M. L. Constant Pressure Molecular Dynamics for Molecular Systems. *Molecular Physics* 1983, 50 (5), 1055–1076. https://doi.org/10.1080/00268978300102851.

Ortega-Sáenz, P.; Pardal, R.; Castellano, A.; López-Barneo, J. Collapse of Conductance Is Prevented by a Glutamate Residue Conserved in Voltage-Dependent $K^+$ Channels. *Journal of General Physiology* 2000, 116 (2), 181–190. https://doi.org/10.1085/jgp.116.2.181.

Ostmeyer, J.; Chakrapani, S.; Pan, A. C.; Perozo, E.; Roux, B. Recovery from Slow Inactivation in $K^+$ Channels Is Controlled by Water Molecules. *Nature* 2013, 501 (7465), 121–124. https://doi.org/10.1038/nature12395.

Pardo, L. A.; Heinemann, S. H.; Terlau, H.; Ludewig, U.; Lorra, C.; Pongs, O.; Stuhmer, W. Extracellular $K^+$ Specifically Modulates a Rat Brain $K^+$ Channel. *Proceedings of the National Academy of Sciences USA* 1992, 89 (6), 2466–2470. https://doi.org/10.1073/pnas.89.6.2466.

Parrinello, M.; Rahman, A. Polymorphic Transitions in Single Crystals: A New Molecular Dynamics Method. *Journal of Applied Physics* 1981, 52 (12), 7182–7190. https://doi.org/10.1063/1.328693.

Patel, A. J.; Honoré, E., Maingret, F.; Lesage, F.; Fink, M.; Duprat, F.; Lazdunski, M. A Mammalian Two Pore Domain Mechano-Gated S-like $K^+$ Channel. *EMBO Journal* 1998, 17 (15), 4283–4290. https://doi.org/10.1093/emboj/17.15.4283.

Pau, V.; Zhou, Y.; Ramu, Y.; Xu, Y.; Lu, Z. Crystal Structure of an Inactivated Mutant Mammalian Voltage-Gated $K^+$ Channel. *Nature Structural and Molecular Biology* 2017, 24 (10), 857–865. https://doi.org/10.1038/nsmb.3457.

Pérez-Hernández, G.; Paul, F.; Giorgino, T.; De Fabritiis, G.; Noé, F. Identification of Slow Molecular Order Parameters for Markov Model Construction. *Journal of Chemical Physics* 2013, 139 (1), 015102. https://doi.org/10.1063/1.4811489.

Periole, X.; Cavalli, M.; Marrink, S.-J.; Ceruso, M. A. Combining an Elastic Network with a Coarse-Grained Molecular Force Field: Structure, Dynamics, and Intermolecular Recognition. *Journal of Chemical Theory and Computation* 2009, 5 (9), 2531–2543. https://doi.org/10.1021/ct9002114.

Piechotta, P. L.; Rapedius, M.; Stansfeld, P. J.; Bollepalli, M. K.; Erhlich, G.; Andres-Enguix, I.; Fritzenschaft, H.; Decher, N.; Sansom, M. S. P.; Tucker, S. J.; Baukrowitz, T. The Pore Structure and Gating Mechanism of $K_{2P}$ Channels. *EMBO Journal* 2011, 30 (17), 3607–3619. https://doi.org/10.1038/emboj.2011.268.

Phillips, J. C.; Braun, R.; Wang, W.; Gumbart, J.; Tajkhorshid, E.; Villa, E.; Chipot, C.; Skeel, R. D.; Kalé, L.; Schulten, K. Scalable Molecular Dynamics with NAMD. *Journal of Computational Chemistry* 2005, 26 (16), 1781–1802. https://doi.org/10.1002/jcc.20289.

Phillips, J. C.; Hardy, D. J.; Maia, J. D. C.; Stone, J. E.; Ribeiro, J. V.; Bernardi, R. C.; Buch, R.; Fiorin, G.; Hénin, J.; Jiang, W.; McGreevy, R.; Melo, M. C. R.; Radak, B. K.; Skeel, R. D.; Singharoy, A.; Wang, Y.; Roux, B.; Aksimentiev, A.; Luthey-Schulten, Z.; Kalé, L. V.; Schulten, K.; Chipot, C.; Tajkhorshid, E. Scalable Molecular Dynamics on CPU and GPU Architectures with NAMD. *Journal of Chemical Physics* 2020, 153 (4), 044130. https://doi.org/10.1063/5.0014475.

Pless, S. A.; Galpin, J. D.; Niciforovic, A. P.; Kurata, H. T.; Ahern, C. A. Hydrogen Bonds as Molecular Timers for Slow Inactivation in Voltage-Gated Potassium Channels. *eLife* 2013, 2, e01289. https://doi.org/10.7554/eLife.01289.

Pope, L.; Arrigoni, C.; Lou, H.; Bryant, C.; Gallardo-Godoy, A.; Renslo, A. R.; Minor, D. L. Protein and Chemical Determinants of BL-1249 Action and Selectivity for $K_{2P}$ Channels. *ACS Chemical Neuroscience* 2018, 9 (12), 3153–3165. https://doi.org/10.1021/acschemneuro.8b00337.

Pope, L.; Lolicato, M., Minor, D. L. Polynuclear Ruthenium Amines Inhibit K2P Channels via a ‘‘Finger in the Dam’’ Mechanism. *Cell Chemical Biology* 2020, 27, 511-524. https://doi.org/10.1016/j.chembiol.2020.01.011.

Prescott, E. D.; Julius, D. A Modular $PIP_2$ Binding Site as a Determinant of Capsaicin Receptor Sensitivity. *Science* 2003, 300 (5623), 1284–1288. https://doi.org/10.1126/science.1083646.

Qin, F. Regulation of TRP Ion Channels by Phosphatidylinositol-4,5-Bisphosphate. In Transient Receptor Potential (TRP) Channels; Flockerzi, V., Nilius, B., Eds.; *Handbook of Experimental Pharmacology*; Springer Berlin Heidelberg 2007, 179, 509–525. https://doi.org/10.1007/978-3-540-34891-7_30.

Rapedius, M.; Schmidt, M. R.; Sharma, C.; Stansfeld, P. J.; Sansom, M. S. P.; Baukrowitz, T.; Tucker. S. J. State-independent intracellular access of quaternary ammonium blockers to the pore of TREK-1. Channels 2012, 6 (6), 473-478. https://doi.org/10.4161/chan.22153.

Renigunta, V.; Schlichthörl, G.; Daut, J. Much more than a leak: structure and function of $K_{2P}$-channels. *Pflügers Archiv - European Journal of Physiology* 2015, 467, 867-894. https://doi.org/10.1007/s00424-015-1703-7.

Renigunta, V.; Zou, X.; Kling, S.; Schlichthörl, G.; Daut, J. Breaking the Silence: Functional Expression of the Two-Pore-Domain Potassium Channel THIK-2. *Pflügers Archiv - European Journal of Physiology* 2014, 466 (9), 1735–1745. https://doi.org/10.1007/s00424-013-1404-z.

Riel, E. B.; Jürs, B. C.; Cordeiro, S.; Musinszki, M.; Schewe, M.; Baukrowitz, T. The Versatile Regulation of $K_{2P}$ Channels by Polyanionic Lipids of the Phosphoinositide and Fatty Acid Metabolism. *Journal of General Physiology* 2022, 154 (2), e202112989. https://doi.org/10.1085/jgp.202112989.

Röblitz, S.; Weber, M. Fuzzy Spectral Clustering by PCCA+: Application to Markov State Models and Data Classification. *Advances in Data Analysis and Classification* 2013, 7 (2), 147–179. https://doi.org/10.1007/s11634-013-0134-6.

Rödström, K. E. J.; Kiper, A. K.; Zhang, W.; Rinné, S.; Pike, A. C. W.; Goldstein, M.; Conrad, L. J.; Delbeck, M.; Hahn, M. G.; Meier, H.; Platzk, M.; Quigley, A.; Speedman, D.; Shrestha, L.; Mukhopadhyay, S. M. M.; Burgess-Brown, N. A.; Tucker, S. J.; Müller, T.; Decher, N.; Carpenter, E. P. A Lower X-Gate in TASK Channels Traps Inhibitors within the Vestibule. *Nature* 2020, 582 (7812), 443–447. https://doi.org/10.1038/s41586-020-2250-8.

Royal, P.; Andres-Bilbe, A.; Ávalos Prado, P.; Verkest, C.; Wdziekonski, B.; Schaub, S.; Baron, A.; Lesage, F.; Gasull, X.; Levitz, J.; Sandoz, G. Migraine-Associated TRESK Mutations Increase Neuronal Excitability through Alternative Translation Initiation and Inhibition of TREK. *Neuron* 2019, 101 (2), 232-245.e6. https://doi.org/10.1016/j.neuron.2018.11.039.

Ryckaert J.-P.; Ciccotti, G.; Berendsen, H. J. C. Numerical integration of the cartesian equations of motion of a system with constraints: Molecular dynamics of n-alkanes. Journal of Computational Physics 1977, 23, 327–341. https://doi.org/10.1016/0021-9991(77)90098-5.

Sandoz, G.; Douguet, D.; Chatelain, F.; Lazdunski, M.; Lesage, F. Extracellular Acidification Exerts Opposite Actions on TREK1 and TREK2 Potassium Channels via a Single Conserved Histidine Residue. *Proceedings of the National Academy of Sciences USA* 2009, 106 (34), 14628–14633. https://doi.org/10.1073/pnas.0906267106.

Scherer, M. K.; Trendelkamp-Schroer, B.; Paul, F.; Pérez-Hernández, G.; Hoffmann, M.; Plattner, N.; Wehmeyer, C.; Prinz, J.-H.; Noé, F. PyEMMA 2: A Software Package for Estimation, Validation, and Analysis of Markov Models. *Journal of Chemical Theory and Computation* 2015, 11 (11), 5525–5542. https://doi.org/10.1021/acs.jctc.5b00743.

Schewe, M.; Nematian-Ardestani, E.; Sun, H.; Musinszki, M.; Cordeiro, S.; Bucci, G.; de Groot, B. L.; Tucker, S. J.; Rapedius, M.; Baukrowitz, T. A Non-Canonical Voltage-Sensing Mechanism Controls Gating in $K_{2P}$ $K^+$ Channels. *Cell* 2016, 164 (5), 937–949. https://doi.org/10.1016/j.cell.2016.02.002.

Schewe, M.; Sun, H.; Mert, Ü.; Mackenzie, A.; Pike, A. C. W.; Schulz, F.; Constantin, C.; Vowinkel, K. S.; Conrad, L. J.; Kiper, A. K.; Gonzalez, W.; Musinszki, M.; Tegtmeier, M.; Pryde, D. C.; Belabed, H.; Nazare, M.; de Groot, B. L.; Decher, N.; Fakler, B.; Carpenter, E. P.; Tucker, S. J.; Baukrowitz, T. A Pharmacological Master Key Mechanism That Unlocks the Selectivity Filter Gate in $K^+$ Channels. Science 2019, 363 (6429), 875–880. https://doi.org/10.1126/science.aav0569.

Schrecke, S.; Zhu, Y.; McCabe, J. W.; Bartz, M.; Packianathan, C.; Zhao, M.; Zhou, M.; Russell, D.; Laganowsky, A. Selective Regulation of Human TRAAK Channels by Biologically Active Phospholipids. *Nature Chemical Biology* 2021, 17 (1), 89–95. https://doi.org/10.1038/s41589-020-00659-5.

Shan, Y.; Klepeis, J. L.; Eastwood, M. P.; Dror, R. O.; Shaw, D. E. Gaussian split Ewald: A fast Ewald mesh method for molecular simulation. *Journal of Chemical Physics* 2005, 122, 054101. https://doi.org/10.1063/1.1839571.

Shaw, D. E.; Grossman, J. P.; Bank, J. A.; Batson, B.; Butts, J. A.; Chao, J. C.; Deneroff, M. M.; Dror, R. O.; Even, A.; Fenton, C. H.; Forte, A.; Gagliardo, J.; Gill, G.; Greskamp, B.; Ho, C. R.; Ierardi, D. J.; Iserovich, L.; Kuskin, J. S.; Larson, R. H.; Layman, T.; Lee, L.-S.; Lerer, A. K.; Li, C.; Killebrew, D.; Mackenzie, K. M.; Mok, S. Y.-H.; Moraes, M. A.; Mueller, R.; Nociolo, L. J.; Peticolas, J. L.; Quan, T.; Ramot, D.; Salmon, J. K.; Scarpazza, D. P.; Schafer,

U. B.; Siddique, N.; Snyder, C. W.; Spengler, J.; Tang, P. T. P.; Theobald, M.; Toma, H.; Towles, B.; Vitale, B.; Wang, S. C.; Young, C. Anton 2: Raising the Bar for Performance and Programmability in a Special-Purpose Molecular Dynamics Supercomputer. In *SC14: International Conference for High Performance Computing, Networking, Storage and Analysis*; IEEE: New Orleans, LA, USA, 2014, 41–53. https://doi.org/10.1109/SC.2014.9.

Shi, N.; Ye, S.; Alam, A.; Chen, L.; Jiang, Y. Atomic Structure of a $Na^+$- and $K^+$-Conducting Channel. *Nature* 2006, 440 (7083), 570–574. https://doi.org/10.1038/nature04508.

Smith, S. S.; Liu, X.; Zhang, Z.-R.; Sun, F.; Kriewall, T. E.; McCarty, N. A.; Dawson, D. C. Cftr: Covalent and Noncovalent Modification Suggests a Role for Fixed Charges in Anion Conduction. *Journal of General Physiology* 2001, 118 (4), 407–432. https://doi.org/10.1085/jgp.118.4.407.

Soussia, I. B.; Choveau, F. S.; Blin, S.; Kim, E.-J.; Feliciangeli, S.; Chatelain, F. C.; Kang, D.; Bichet, D.; Lesage, F. Antagonistic Effect of a Cytoplasmic Domain on the Basal Activity of Polymodal Potassium Channels. *Frontiers in Molecular Neuroscience* 2018, 11, 301. https://doi.org/10.3389/fnmol.2018.00301.

Sugita, Y.; Kitao, A.; Okamoto, Y. Multidimensional Replica-Exchange Method for Free-Energy Calculations. *Journal of Chemical Physics* 2000, 113 (15), 6042–6051. https://doi.org/10.1063/1.1308516.

Suh, B.; Hille, B. Regulation of Ion Channels by Phosphatidylinositol 4,5-Bisphosphate. *Current Opinion in Neurobiology* 2005, 15 (3), 370–378. https://doi.org/10.1016/j.conb.2005.05.005.

Suh, B.; Hille, B. $PIP_2$ Is a Necessary Cofactor for Ion Channel Function: How and Why? *Annual Review of Biophysics* 2008, 37 (1), 175–195. https://doi.org/10.1146/annurev.biophys.37.032807.125859.

Sun, J.; MacKinnon, R. Structural Basis of Human KCNQ1 Modulation and Gating. *Cell* 2020, 180 (2), 340-347.e9. https://doi.org/10.1016/j.cell.2019.12.003.

Taylor, K. C.; Sanders, C. R. Regulation of KCNQ/Kv7 Family Voltage-Gated $K^+$ Channels by Lipids. *Biochimica et Biophysica Acta (BBA) - Biomembranes* 2017, 1859 (4), 586–597. https://doi.org/10.1016/j.bbamem.2016.10.023.

Thompson, M. J.; Baenziger, J. E. Ion Channels as Lipid Sensors: From Structures to Mechanisms. *Nature Chemical Biology* 2020, 16 (12), 1331–1342. https://doi.org/10.1038/s41589-020-00693-3.

Vaithianathan, T.; Bukiya, A.; Liu, J.; Liu, P.; Asuncion-Chin, M.; Fan, Z.; Dopico, A. Direct Regulation of BK Channels by Phosphatidylinositol 4,5-Bisphosphate as a Novel Signaling Pathway. *Journal of General Physiology* 2008, 132 (1), 13–28. https://doi.org/10.1085/jgp.200709913.

van der Cruijsen, E. A. W.; Nand, D.; Weingarth, M.; Prokofyev, A.; Hornig, S.; Cukkemane, A. A.; Bonvin, A. M. J. J.; Becker, S.; Hulse, R. E.; Perozo, E.; Pongs, O.; Baldus, M. Importance of Lipid-Pore Loop Interface for Potassium Channel Structure and Function. *Proceedings of the National Academy of Sciences USA* 2013, 110 (32), 13008–13013. https://doi.org/10.1073/pnas.1305563110.

Vanommeslaeghe, K.; Hatcher, E.; Acharya, C.; Kundu, S.; Zhong, S.; Shim, J.; Darian, E.; Guvench, O.; Lopes, P.; Vorobyov, I.; Mackerell, A. D. CHARMM General Force Field: A

Force Field for Drug-like Molecules Compatible with the CHARMM All-Atom Additive Biological Force Fields. *Journal of Computational Chemistry* 2010, 31 (4), 671-690. https://doi.org/10.1002/jcc.21367.

Vanommeslaeghe, K.; MacKerell, A. D. Automation of the CHARMM General Force Field (CGenFF) I: Bond Perception and Atom Typing. *Journal of Chemical Information and Modeling* 2012, 52 (12), 3144–3154. https://doi.org/10.1021/ci300363c.

Vanommeslaeghe, K.; Raman, E. P.; MacKerell, A. D. Automation of the CHARMM General Force Field (CGenFF) II: Assignment of Bonded Parameters and Partial Atomic Charges. *Journal of Chemical Information and Modeling* 2012, 52 (12), 3155–3168. https://doi.org/10.1021/ci3003649.

van Paridon, P. A.; de Kruijff, B.; Ouwerkerk, R.; Wirtz, K. W. A. Polyphosphoinositides Undergo Charge Neutralization in the Physiological PH Range: A 31P-NMR Study. *Biochimica et Biophysica Acta (BBA) - Lipids and Lipid Metabolism* 1986, 877 (1), 216–219. https://doi.org/10.1016/0005-2760(86)90137-2.

Vivier, D.; Soussia, I. B.; Rodrigues, N.; Lolignier, S.; Devilliers, M.; Chatelain, F. C.; Prival, L.; Chapuy, E.; Bourdier, G.; Bennis, K.; Lesage, F.; Eschalier, A.; Busserolles, J.; Ducki, S. Development of the First Two-Pore Domain Potassium Channel TWIK-Related $K^+$ Channel 1-Selective Agonist Possessing in Vivo Antinociceptive Activity. *Journal of Medicinal Chemistry* 2017, 60 (3), 1076–1088. https://doi.org/10.1021/acs.jmedchem.6b01285.

Wang, W.; MacKinnon, R. Cryo-EM Structure of the Open Human Ether-à-Go-Go -Related $K^+$ Channel HERG. *Cell* 2017, 169 (3), 422-430.e10. https://doi.org/10.1016/j.cell.2017.03.048.

Wassenaar, T. A.; Ingólfsson, H. I.; Böckmann, R. A.; Tieleman, D. P.; Marrink, S. J. Computational Lipidomics with Insane: A Versatile Tool for Generating Custom Membranes for Molecular Simulations. *Journal of Chemical Theory and Computation* 2015, 11 (5), 2144–2155. https://doi.org/10.1021/acs.jctc.5b00209.

Woo, J.; Jeon, Y. K.; Zhang, Y.-H.; Nam, J. H.; Shin, D. H.; Kim, S. J. Triple Arginine Residues in the Proximal C-Terminus of TREK $K^+$ Channels Are Critical for Biphasic Regulation by Phosphatidylinositol 4,5-Bisphosphate. *American Journal of Physiology -Cell Physiology* 2019, 316 (3), C312–C324. https://doi.org/10.1152/ajpcell.00417.2018.

Woo, J.; Shin, D. H.; Kim, H. J.; Yoo, H. Y.; Zhang, Y.-H.; Nam, J. H.; Kim, W. K.; Kim, S. J. Inhibition of TREK-2 $K^+$ Channels by PI(4,5)P2: An Intrinsic Mode of Regulation by Intracellular ATP via Phosphatidylinositol Kinase. *Pflügers Archiv - European Journal of Physiology* 2016, 468 (8), 1389–1402. https://doi.org/10.1007/s00424-016-1847-0.

Wu, E. L.; Cheng, X.; Jo, S.; Rui, H.; Song, K. C.; Dávila-Contreras, E. M.; Qi, Y.; Lee, J.; Monje-Galvan, V.; Venable, R. M.; Klauda, J. B.; Im, W. CHARMM-GUI Membrane Builder toward Realistic Biological Membrane Simulations. *Journal of Computational Chemistry* 2014, 35 (27), 1997–2004. https://doi.org/10.1002/jcc.23702.

Wu, X.; Liu, Y.; Chen, X.; Sun, Q.; Tang, R.; Wang, W.; Yu, Z.; Xie, M. Involvement of TREK-1 Activity in Astrocyte Function and Neuroprotection Under Simulated Ischemia

Conditions. *Journal of Molecular Neuroscience* 2013, 49 (3), 499–506. https://doi.org/10.1007/s12031-012-9875-5.

Yarishkin, O.; Phuong, T. T. T.; Bretz, C. A.; Olsen, K. W.; Baumann, J. M.; Lakk, M.; Crandall, A.; Heurteaux, C.; Hartnett, M. E.; Križaj, D. TREK-1 channels regulate pressure sensitivity and calcium signaling in trabecular meshwork cells. *Journal of General Physiology* 2018, 150 (12), 1660–1675. https://doi.org/10.1085/jgp.201812179.

Ye, W.; Han, T. W.; Nassar, L. M.; Zubia, M.; Jan, Y. N.; Jan, L. Y. Phosphatidylinositol-(4, 5)-Bisphosphate Regulates Calcium Gating of Small-Conductance Cation Channel TMEM16F. *Proceedings of the National Academy of Sciences USA* 2018, 115 (7), E1667–E1674. https://doi.org/10.1073/pnas.1718728115.

Yesylevskyy, S. O.; Schäfer, L. V.; Sengupta, D.; Marrink, S. J. Polarizable Water Model for the Coarse-Grained MARTINI Force Field. *PLoS Computational Biology* 2010, 6 (6), e1000810. https://doi.org/10.1371/journal.pcbi.1000810.

Yoshida, K.; Shi, S.; Ukai-Tadenuma, M.; Fujishima, H.; Ohno, R.; Ueda, H. R. Leak potassium channels regulate sleep duration. *Proceedings of the National Academy of Sciences, USA* 2018, 115 (40), E9459–E9468. https://doi.org/10.1073/pnas.1806486115.

Yu, F. H.; Yarov-Yarovoy, V.; Gutman, G. A.; Catterall, W. A. Overview of Molecular Relationships in the Voltage-Gated Ion Channel Superfamily. *Pharmacological Reviews* 2005, 57, 387-395. https://doi.org/10.1124/pr.57.4.13.

Yuill, K. H.; Stansfeld, P. J.; Ashmole, I.; Sutcliffe, M. J.; Stanfield, P. R. The Selectivity, Voltage-Dependence and Acid Sensitivity of the Tandem Pore Potassium Channel TASK-1:

Contributions of the Pore Domains. *Pflügers Archiv - European Journal of Physiology* 2007, 455 (2), 333–348. https://doi.org/10.1007/s00424-007-0282-7.

Zhou, Y.; MacKinnon, R. The Occupancy of Ions in the $K^+$ Selectivity Filter: Charge Balance and Coupling of Ion Binding to a Protein Conformational Change Underlie High Conduction Rates. *Journal of Molecular Biology* 2003, 333 (5), 965–975. https://doi.org/10.1016/j.jmb.2003.09.022.

Zhou, Y.; Morais-Cabral, J. H.; Kaufman, A.; MacKinnon, R. Chemistry of Ion Coordination and Hydration Revealed by a $K^+$ Channel–Fab Complex at 2.0 Å Resolution. *Nature* 2001, 414 (6859), 43–48. https://doi.org/10.1038/35102009.

Zilberberg, N.; Ilan, N.; Goldstein, S. A. N. KCNKØ: Opening and Closing the 2-P-Domain Potassium Leak Channel Entails "C-Type" Gating of the Outer Pore. *Neuron* 2001, 32 (4), 635–648. https://doi.org/10.1016/S0896-6273(01)00503-7.

Zyrianova, T.; Lopez, B.; Riccardo Olcese, R.; Belperio, J.; Waters, C. M.; Wong, L.; Nguyen, V.; Talapaneni, S.; Schwingshackl, A. $K_{2P}$2.1 (TREK-1) potassium channel activation protects against hyperoxia-induced lung injury. *Scientific Reports* 2020, 10, 22011. https://doi.org/10.1038/s41598-020-78886-y.

**Publishing Agreement**

It is the policy of the University to encourage open access and broad distribution of all theses, dissertations, and manuscripts. The Graduate Division will facilitate the distribution of UCSF theses, dissertations, and manuscripts to the UCSF Library for open access and distribution. UCSF will make such theses, dissertations, and manuscripts accessible to the public and will take reasonable steps to preserve these works in perpetuity.

I hereby grant the non-exclusive, perpetual right to The Regents of the University of California to reproduce, publicly display, distribute, preserve, and publish copies of my thesis, dissertation, or manuscript in any form or media, now existing or later derived, including access online for teaching, research, and public service purposes.

DocuSigned by:
Andrew M. Natale
2F0643E9A065454...
Author Signature

3/10/2022
Date